Production of electrons from heavy flavor decays in proton-lead collisions measured with ALICE at the LHC

A Dissertation Presented for the

Doctor of Philosophy

Degree

The University of Tennessee, Knoxville

Rebecca Michelle Scott

May 2017

© by Rebecca Michelle Scott, 2017
All Rights Reserved.

Acknowledgements

I would like to first thank my advisors, Soren Sorensen, Ken Read, and Christine Nattrass for their time, patience and encouragement. I am so thankful that I had the opportunity to learn from three wonderful advisors that each helped me in a unique way.

Having Dr. Nattrass as a role model and mentor was invaluable. She helped me figure out the tiny details that no one else seemed to have the patience for.

Dr. Read helped me see the super modules for the towers. I could always rely on him to give me honest feedback and help me figure out the best action to take next.

Dr. Sorensen was simply the best advisor I could ever ask for. I will always have a profound debt of gratitude for his scientific guidance and selfless support and encouragement.

I am so grateful that I had the wonderful opportunity to go to CERN and work among the brilliant physicists that make up the ALICE collaboration. I could not have done this without the hard work from my collaborators, and all the engineers and technicians who contributed to the construction, performance and support of the LHC, the ALICE experiment and the Grid.

In particular I would like to thank Cristiane Jahnke, Shingo Sakai, and Deepa Thomas who taught and helped me so much.

From the UT and ORNL group, I would like to thank Abhisek Sen, David Silvermyr, Matt Wysocki, Natasha Sharma, and Andrew Castro who helped me at different stages of my analysis.

Thanks to Dr. Marianne Breinig and Chrisanne Romeo who were always willing to help and give advice.

I also would like to thank Kyle Schmoll. When I wanted to quit he gave me the encouragement that I needed to continue on.

I would like to thank my parents, Dora and Antonino Carnevali, who invested in my education and helped me learn to think like a scientist. I would also like to thank my oldest sibling and best friend Alana, and my favorite and only brother Corey.

Lastly, I would like to thank Neutrino, Cappy and Barlow who gave me unconditional love and companionship throughout my time in graduate school.

"The story so far:

In the beginning the Universe was created. This has made a lot of people very angry and been widely regarded as a bad move."

– Douglas Adams, The Restaurant at the End of the Universe

Abstract

This dissertation presents a measurement of the yield and cross section of electrons from heavy flavor decays at central rapidity in proton-lead collisions measured by the ALICE (A Large Ion Collider Experiment) detector at the Large Hadron Collider. This analysis extends the transverse momentum reach of an earlier measurement in ALICE and the comparison is shown. The cross section of single electrons in proton-lead collisions is compared to the value expected in the absence of nuclear modification from proton-proton collisions. The cross section is well described by the perturbative Quantum Chromodynamics and no statistically significant alteration due to hot nuclear matter effects is observed. The results are also compared to other measurements of heavy flavor and collision systems.

Table of Contents

1 Introduction **1**

1.1 The Standard Model 2

1.2 Quantum Chromodynamics (QCD) 3

1.3 Heavy Flavor 5

1.3.1 Heavy Flavor Quark Production 5

1.3.2 Electrons from Semileptonic Decays of Charm and Bottom Hadrons 7

1.4 Relativistic Proton-Nucleus Collisions 9

1.4.1 Kinematic Variables 9

1.4.2 Collision Geometry 11

1.4.3 Transverse Energy and Charged Particle Multiplicity 14

1.4.4 Lund Model 16

1.5 Nuclear Modification Factor 18

1.6 Cold Nuclear Matter Effects 19

1.6.1 Cronin Effect 19

1.6.2 Shadowing and Anti-Shadowing 21

2 Theoretical and Experimental Status **23**

2.1 QCD prediction of heavy flavor production 23

2.1.1 FONLL 25

2.2 Early Single Lepton Measurements 26

2.3 Single lepton measurements at RHIC 30
2.4 Single lepton measurements at the LHC 32
2.4.1 Electrons from heavy flavor in pp collisions 32
2.4.2 Electrons from heavy flavor in pPb collisions 34
2.4.3 D Mesons at the LHC 35
2.4.4 B Mesons at the LHC 37

3 Experimental Overview 40
3.1 Large Hadron Collider 40
3.2 ALICE Experiment 41
3.2.1 ALICE coordinate system 42
3.3 VZERO 43
3.3.1 Design of the VZERO 43
3.3.2 VZERO Event trigger 45
3.3.3 VZERO Centrality and Multiplicity measurement 46
3.4 Inner Tracking System 46
3.5 Time Projection Chamber 50
3.5.1 Charged particles interactions with the TPC 51
3.5.2 TPC dE/dx 52
3.6 Electromagnetic Calorimeter: EMCal 53
3.6.1 Electron and Photon interactions with the EMCal 54
3.6.2 Other particle interactions with the EMCal 56
3.6.3 Design of the EMCal 59
3.6.4 EMCal Electronics 61
3.6.5 EMCal Calibration 63
3.6.6 Cluster Algorithms 64
3.6.7 EMCal Trigger 67
3.7 Data Objects 69

4 Analysis **71**

4.1 pPb Collisions in ALICE . . . 71

4.2 Run selection . . . 72

4.3 Event and Track Selection . . . 73

4.4 EMCal Cluster and Track Matching . . . 76

4.5 Trigger Scaling . . . 78

4.6 Particle Identification cuts . . . 82

4.6.1 TPC electron identification: n_{σ}^{TPC} . . . 82

4.6.2 EMCal electron identification: E/p . . . 83

4.6.3 EMCal electron identification: M20 and M02 . . . 87

4.7 Hadron Background Subtraction . . . 93

4.8 Photonic Electron Background . . . 96

4.9 Acceptance and Efficiency . . . 104

4.10 Error Analysis . . . 106

4.10.1 Particle identification systematics: n_{σ}^{TPC} . . . 107

4.10.2 Particle identification systematics: Shower Shape . . . 109

4.10.3 Particle identification systematics: E/p . . . 110

4.10.4 Background Determination Systematics . . . 111

4.10.5 Total Systematics . . . 114

5 Results and Discussion **115**

5.1 Invariant Yield of HFE . . . 115

5.2 Cross Section of HFE . . . 117

5.3 Nuclear Modification Factor R_{pA} . . . 118

5.4 Comparison to previous measurement . . . 120

5.5 Comparison to similar analysis . . . 123

5.6 Comparison to other results . . . 124

6 Summary and Conclusions **127**

Bibliography **130**

Vita **140**

Chapter 1

Introduction

The main goal of the ALICE (A Large Ion Collider Experiment) detector at the Large Hadron Collider is to study nuclear matter under high temperature and energy density by creating a Quark Gluon Plasma (QGP) in ultra relativistic nucleus-nucleus collisions. Complementary studies of proton-proton collisions and proton-nucleus collisions are not expected to produce a Quark-Gluon Plasma and are essential to provide a baseline for the measurements carried out in heavy-ion collisions. Proton-nucleus collisions are also interesting in their own right, providing a view into cold nuclear matter effects and the modifications to parton distributions in the proton and the nucleus.

Heavy flavor quarks, charm and bottom, are produced from hard parton scattering early in the collision and traverse the medium throughout its evolution, making them a good probe. The production of heavy-flavor is sensitive to the parton distributions and the medium produced in the collisions. Due to the large mass of the charm and bottom quark, their production cross sections can be calculated by perturbative Quantum Chromodynamics. Single electrons from the semileptonic decays of charm and bottom mesons provide one way of measuring heavy flavor production.

This dissertation describes the measurement of the production of single electrons that come from the decay of heavy flavor D and B mesons. Chapter 1 provides the

context for this measurement and defines the basic words and concepts. Chapter 2 describes the experimental status of the field. Chapter 3 describes the ALICE experiment in detail. Chapter 4 describes the steps taken in this analysis. Chapter 5 reports the final results and provides a discussion of the results compared to other relevant measurements. Chapter 6 summarizes the final conclusions.

1.1 The Standard Model

The Standard Model of particle physics, formulated in the 1970s, describes all of the known elementary particle interactions except for gravity [1]. The current view is that all matter is comprised of three fundamental pieces: quarks, leptons, and force mediators. The names of these fundamental constituents along with their mass, charge, and spin are shown in figure 1.1 [2]. The spin is given in units of $\hbar$. The charges are written in units of e, where the charge of an electron is $-e$. The quarks and leptons also have antiparticles which were omitted from 1.1. The antiparticles (antiquarks: $\bar{u}, \bar{d}, \bar{c}, \bar{s}, \bar{t}, \bar{b}$, antileptons: e^+ (positron), $\mu^+, \tau^+, \bar{\nu_\mathrm{e}}, \bar{\nu_\mu}, \bar{\nu_\tau}$) have the same mass and spin as their particle counterparts but have opposite charge.

The electron, muon and tau are leptons, all with $-e$ charge. The electron is thought to be stable. However, the muon and tau will spontaneously decay. The muon has a mean lifetime of $2.1969811 \pm 0.0000022 \times 10^{-6}$ s [3] and its primary decay is into an electron, electron antineutrino and muon neutrino: $\mu^- \rightarrow \mathrm{e}^- \, \bar{\nu_\mathrm{e}} \, \nu_\mu$. The tau has a much shorter lifetime of $2.906 \pm 0.010 \times 10^{-13}$ s and can decay into hadrons and other particles. The muon is about 200 times more massive than the electron. The tau is about 3,500 times more massive than the electron and about twice the mass of a proton.

The leptons also include three flavors of neutrinos. Neutrinos have no electric charge and a very light mass.

There are six flavors of quarks: up, down, charm, strange, top (also referred to as "truth"), and bottom (also referred to as "beauty"). Up, charm and top quarks carry

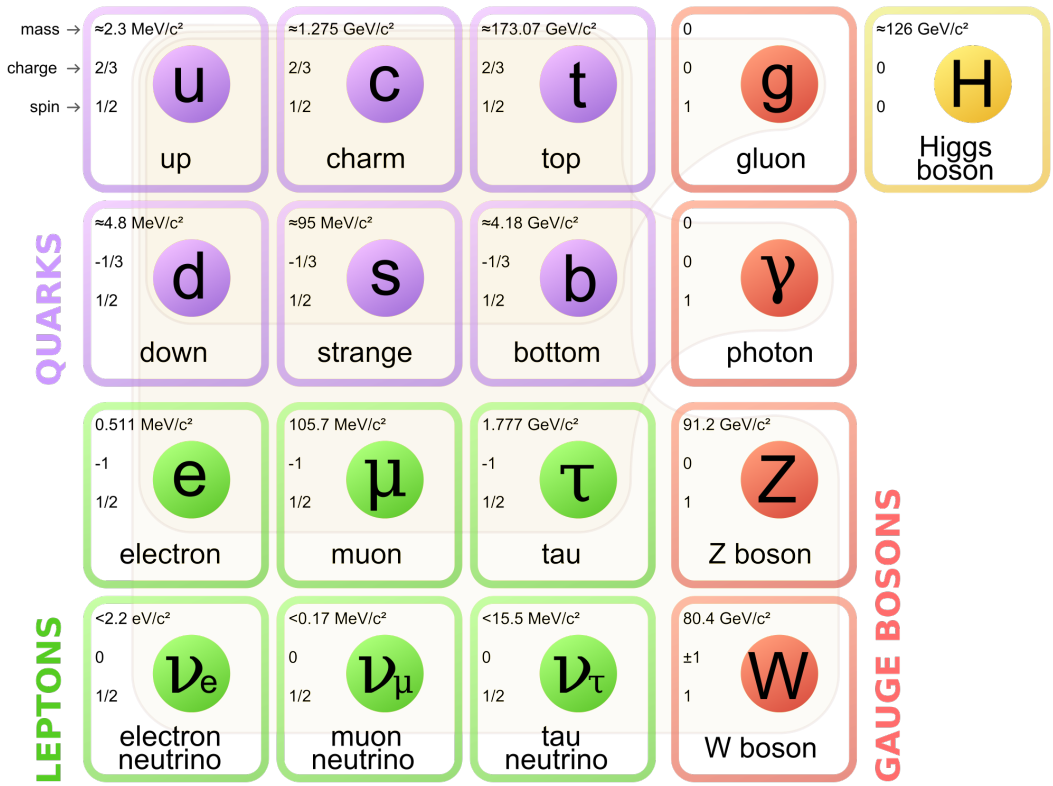


Figure 1.1: The standard model of particle physics [2].

charges of $+\frac{2}{3}e$ while down, strange and bottom carry a charge of $-\frac{1}{3}e$. Individual quarks can not be directly observed, a phenomenon called quark confinement.

The interactions between fermions (quarks, leptons, and baryons) can be described as an exchange of bosons. The strong interaction is mediated by the gluon, which is responsible for binding quarks in baryons and binding the protons and neutrons in a nucleus. Interactions between electrically charged particles are governed by the electromagnetic force and mediated by photons. Weak interactions have three intermediate bosons, W^+, W^- and Z^0. Weak interactions are responsible for β-decay.

1.2 Quantum Chromodynamics (QCD)

Quantum chromodynamics describes the interactions between quarks. Quarks have a degree of freedom, called color. Quarks can have three possible values of a color

Table 1.1: Fundamental forces [1] [4]

Interaction	Mediator	Theory	Range
Strong	gluon, g	Chromodynamics	1F $\simeq \frac{1}{m_\pi}$
Electromagnetic	photon, γ	Electrodynamics	∞
Weak	$W^{\pm}$, Z^0	Flavordynamics	$\frac{1}{M_W}$

charge and anti-quarks have anti-color making six total types of color charge. The color values are red (r), blue (b), and green (g).

The force between the quark-quark interaction is mediated by the exchange of a vector boson called the gluon. A gluon is a massless particle with spin 1 and has one unit of color and anticolor. There are eight possible gluon color states. One way of presenting the color octet is shown in the list 1.1 [1] [4].

$$\begin{array}{ll} \frac{1}{\sqrt{2}}(r\bar{b}+b\bar{r}) & \frac{-i}{\sqrt{2}}(r\bar{b}-b\bar{r}) \\ \frac{1}{\sqrt{2}}(r\bar{g}+g\bar{r}) & \frac{-i}{\sqrt{2}}(r\bar{g}-g\bar{r}) \\ \frac{1}{\sqrt{2}}(b\bar{g}+g\bar{b}) & \frac{-i}{\sqrt{2}}(b\bar{g}-g\bar{b}) \\ \frac{1}{\sqrt{2}}(r\bar{r}-b\bar{b}) & \frac{1}{\sqrt{6}}(r\bar{r}+b\bar{b}-2g\bar{g}) \end{array} \tag{1.1}$$

Leptons can be found as free particles but quarks are confined into colorless composite particles called hadrons. Quarks are only seen in baryons (three quarks, QQQ) and mesons (quark and antiquark, $Q\bar{Q}$). The proton is a baryon and composed of two up quarks and one down quark. An example of a meson is the D^+ which is composed of a charm and antidown.

The strength of the strong force is given by the running coupling constant, α_s. α_s decreases with smaller distances and increasing energy. At large distances, such as the size of atoms, α_s is large and quarks are confined. However, for small distances and high energies, α_s approaches zero and quark-quark interactions are minor and

quarks can be treated as free particles. This is known as asymptotic freedom. (See figure 2.1 [5].)

1.3 Heavy Flavor

Because the QGP is very short lived ($\tau \sim 10 fm/c$), the medium must be studied with the particles created during the collision. Heavy-flavor quarks, charm and bottom, are produced early in the collision from hard partonic scatterings. For $c\bar{c}$ production, the time scale is $\sim \hbar/(2m_Q c^2) \simeq 0.2/2.4 \simeq 0.08 fm/c$[6]. Production or annihilation of heavy-flavor quarks at later times in the evolution of the collision is not expected, therefore the total number of heavy flavor quarks is constant after the initial stages of the collision. The heavy quarks can interact with the partons in the medium while traversing the medium. In this way, the heavy flavor quarks can carry information about the medium. This makes charm and bottom quarks a good probe for the QGP.

Since the charm and bottom quark are heavier than the light up and down quarks, they were expected to not react as strongly to the medium. However measurements have shown that charm and bottom undergo a suppression similar to light quarks. This makes the measurement of heavy flavor particularly interesting.

1.3.1 Heavy Flavor Quark Production

The factorization theorem can be used to calculate the cross section for the production of the heavy quarks. Heavy quarks are made in the hard collision of light partons a and b of each hadron A and B and produce heavy quarks C and D. The cross section can be expressed as the factorized form in equation 1.2 [7]. In this equation, C and D refers to heavy flavored quarks with mass M. Y is the rapidity in the center of mass frame of partons a and b, $Y = \frac{1}{2}\ln(x_A/x_B)$.

$$\frac{d\sigma}{dy_c dy_D} = \sum_{a,b} \int dx_A f_{a/A}(x_A) \int dx_B f_{b/B}(x_B) H_{ab}(y_C - Y, y_D - Y, x_A x_B s, M) \quad (1.2)$$

This cross section can be described by the multiplication of three components. The first ingredient is $f_{a/A}(x_A)$, the parton distribution function. This describes the probability of finding a parton of type a with some momentum fraction x_A in a hadron. The second factor is the probability of finding another parton of type b with some momentum x_B in another hadron. The third component is H_{ab}, the hard scattering function for the production of a heavy quark pair from partons a and b. This describes the probability that these two partons will produce a heavy flavor quark pair.

Figure 1.2 shows the lowest-order QCD diagrams for flavor creation process [8]. The diagrams show the production of charm/anti-charm or bottom/anti-bottom pairs. Time is shown going left to right in the figures 1.2. The thin lines represent light quarks. Heavy quarks are represented by a thick line. Gluons are represented by corkscrew lines. These are the most common processes for creating heavy flavor. The left most diagram shows light quark and anti-quark annihilating and producing a heavy quark and anti-quark pair. The next three diagrams show two gluons interacting and producing a heavy quark and anti-quark pair.

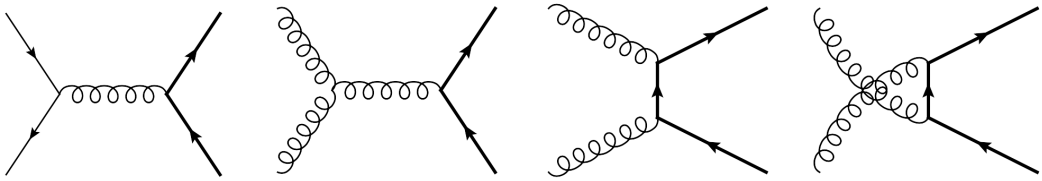


Figure 1.2: Leading Order Feynman diagrams for heavy quark production [8].

Heavy quarkonium, a $c\bar{c}$ or $b\bar{b}$ pair, can be created by gluon fusion in either the color singlet or color octet state[9] [10]. In the color singlet model, the quarkonium is formed with the same quantum numbers in a color singlet state. The bound state is a colorless meson, J/Ψ for $c\bar{c}$ and Υ for $b\bar{b}$. If quarkonium is produced in the

Table 1.2: Table of Heavy Flavor Mesons and their decays [3]

Meson Name	Quark content	Decay length, $c\tau$	Relevant $e^{\pm}$ decay	fraction
D^+ , D^-	$c\bar{d}$, $\bar{c}d$	311.8 μm	$D^+ \to e^+ +$ anything	$16.0 \pm 0.4\%$
D^0 , $\bar{D}^0$	$c\bar{u}$, $\bar{c}u$	122.9 μm	$D^0 \to e^+ +$ anything	$6.53 \pm 0.17\%$
B^+ , B^-	$u\bar{b}$, $\bar{u}b$	492.0 μm	$B^+ \to e^+\nu_e X_C$	$10.99 \pm 0.28\%$
B^0 , $\bar{B}^0$	$d\bar{b}$, $\bar{d}b$	455.4 μm	$B^0 \to e^+\nu_e X_C$	$10.1 \pm 0.4\%$
			$B \to D \to e$	9.6%

color octet state, the quark-antiquark pair will have "extra, unwanted" color. The quarkonium can neutralize its color by radiating off soft gluons, or combine with a light quark-antiquark pair and create charm or bottom mesons.

The color singlet state is formed at shorter distances than the color octet state. The color octet cross section is substantially larger than the color singlet cross section. The color singlet state is more tightly bound and is more likely to produce J/Ψ and Υ. The octet state is fragile and is more likely to produce open heavy flavor.

1.3.2 Electrons from Semileptonic Decays of Charm and Bottom Hadrons

This analysis measured the production of open heavy flavor, that is hadrons containing a single charm or bottom quark. The J/Ψ (comprised of charm-anticharm) and Υ (comprised of bottom-antibottom) are considered background.

Heavy flavor hadrons measured in this analysis are made up of one charm or bottom quark and a light quark: $D^+, D^-, D^0, \bar{D}^0, B^+, B^-, B^0, \bar{B}^0$. Table 1.2 shows a list of the open heavy flavor hadrons, the quark constituents, decay length and decay fraction relevant to this analysis [3]. B mesons can also have decay daughters D^+, D^-, D^0, and $\bar{D}^0$, making it difficult to separate the contribution from bottom and charm.

The decay length of the D and B mesons are on the order of a few hundred micrometers while the innermost detectors in ALICE have a radius of a few centimeters. For this reason, a meson containing a heavy quark does not survive long enough to travel through the detector to be studied directly. Instead they must be studied by their decay products. A meson containing a charm or bottom quark can decay hadronically or semileptonically as shown in the diagram in figure 1.3 [11].

In the center of the drawing on figure 1.3, a charm and anti-charm pair is created. The c quark goes into a D^0 meson and the $\bar{c}$ quark goes into a $\bar{D}^0$ meson. Shown on the left half of the figure, the D^0 undergoes a hadronic decay into a K^- and a π^+. On the right hand side of the figure, the $\bar{D}^0$ has a semileptonic decay into a K^+ meson and a lepton (which could be an electron, muon or tau) and the corresponding neutrino. The kaon, pion, and lepton can be measured in the detector. In this way, charm and bottom mesons can be studied by their hadronic or their semileptonic decay products.

The focus of this dissertation is the type of decay drawn on the right half of figure 1.3, where the decay product contains a *single electron*. Electrons produced

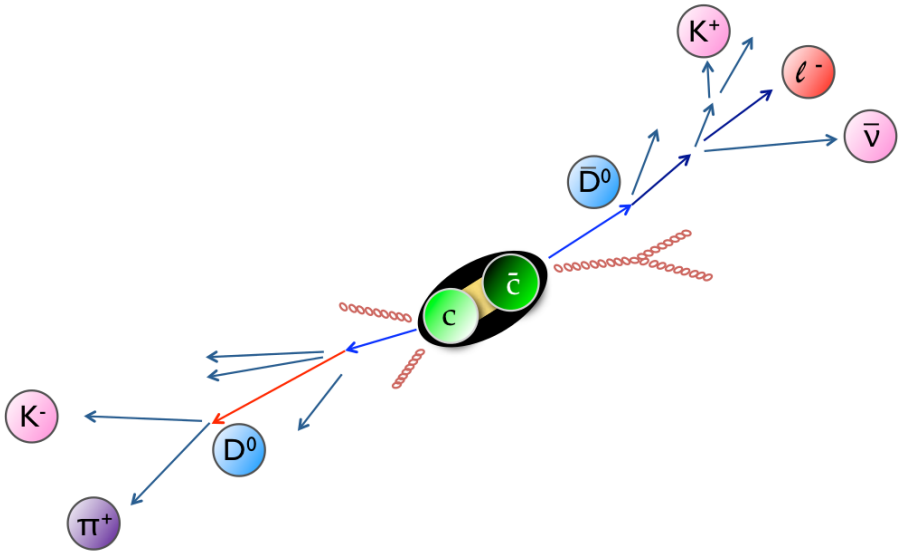


Figure 1.3: Schematic of a hadronic and semileptonic decay of D mesons [11].

in pairs, $e^+ + e^-$, are the main source of background to this measurement. These background electrons are often referred to as *photonic electrons*, as a main source is photon conversion. The spectrum of single electrons is dominated by electrons from the semileptonic decays of D and B mesons. The measurement of electrons from semileptonic decays of charm and bottom mesons is also labeled as the measurement of *non-photonic electrons* and *single electrons*.

1.4 Relativistic Proton-Nucleus Collisions

In this section basic terms and concepts of relativistic collisions will be discussed. The kinematic variables are general for proton-proton, proton-nucleus, and nucleus-nucleus collisions. The initial geometry of proton-nucleus collisions differs from proton-proton and nucleus-nucleus collisions.

1.4.1 Kinematic Variables

In relativistic collisions, it is convenient to use kinematic variables in relation to the beam axis and the laboratory frame. The coordinate system used for the ALICE experiment places the beam direction along the z direction, with positive y pointing towards the sky. The z = 0 position is the approximate region where the beams cross and collisions occur. Figure 3.2 has z and y labeled in a drawing of the ALICE detector.

Transverse momentum, $\mathbf{p_T}$ is a kinetic variable that is used frequently in heavy-ion physics. Cross sections and yields are often shown with respect to p_T. A particle's p_T is the magnitude of the particle's momentum component perpendicular to the beam axis.

$$p_T = \sqrt{p_x^2 + p_y^2} = p \sin\theta = p_z \tan\theta \tag{1.3}$$

Rapidity, y, is a useful quantity for relativistic velocities because the rapidities can be added and subtracted like the velocity in the non-relativistic case if the two

frames of reference are moving at a constant velocity relative to each other. A great reference with an example and a more detailed description of rapidity is [12]. The rapidity can be calculated using the energy and the longitudinal momentum component of a particle.

$$y = \frac{1}{2} \ln \left(\frac{E + p_z}{E - p_z} \right) \tag{1.4}$$

The **pseudorapidity**, η, variable is often more convenient because it can be measured solely based on the angle of a particle's trajectory. Rapidity is dependent on knowing the momentum and identity of a particle which is not always known in an experiment. The pseudorapidity is given by equation 1.5.

$$\eta \equiv -\ln \left[\tan \frac{\theta}{2} \right] \qquad \text{and} \qquad \eta = \frac{1}{2} \ln \left[\frac{|\mathbf{p}| + p_z}{|\mathbf{p}| - p_z} \right] \tag{1.5}$$

The pseudorapidity can be positive or negative, depending on the particle's direction, and can range from $-\infty$ to ∞. Figure 1.4 shows the values of pseudorapidity that correspond to various angles with respect to the beam axis. The detectors used to identify electrons in this analysis are the tracking detectors, with a range $|\eta| < 0.9$, and the Electromagnetic Calorimeter, inside of $|\eta| < 0.7$.

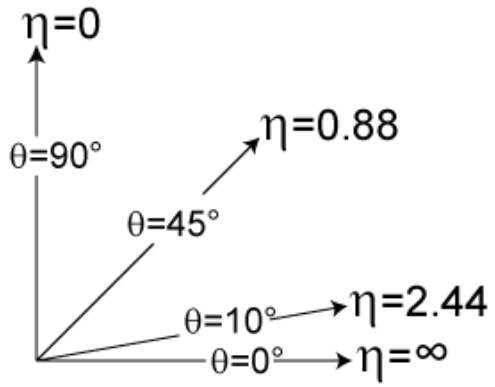


Figure 1.4: Various pseudorapidity values that correspond to the angle relative to the beam axis [13].

The rapidity and pseudorapidity are approximately equal for particles with momenta about equal to their energy, $|\mathbf{p}| \approx E$, which can be seen by comparing equation 1.4 and 1.5. Electrons have a small mass of 0.0005 GeV/c^2. Typical values measured in this analysis for electrons are 1 GeV/c $< p_T <$ 30 GeV/c. Consequently for this electron analysis, $|\mathbf{p}| \approx E$ and $y \approx \eta$.

1.4.2 Collision Geometry

The collision geometry is defined by the impact parameter, b. In a nucleus-nucleus collision the impact parameter is easy to visualize as shown in figure 1.5. The value of b can be in the range $0 < b < R_1 + R_2$, where the radii of the colliding nuclei are R_1 and R_2. Figure 1.6 shows drawings of longitudinal and transverse views of an Au-Au collision with impact parameter $b = 6$ fm. The nucleons in the overlapping regions are the participants, and drawn as darker red and blue circles.

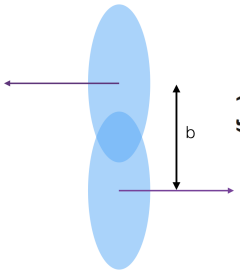


Figure 1.5: Impact parameter, b.

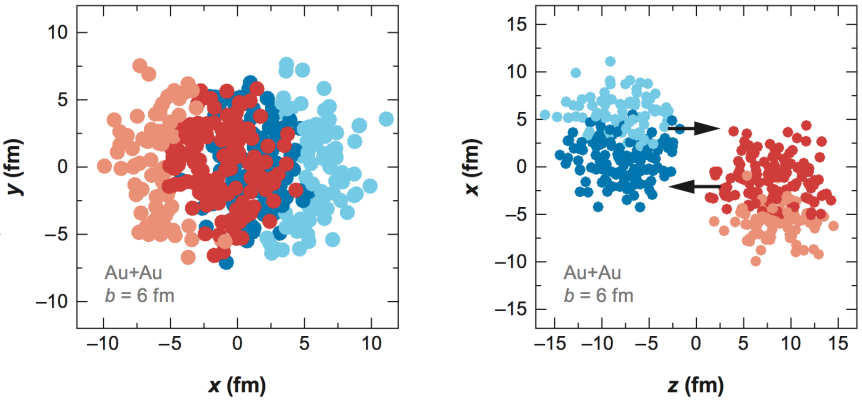


Figure 1.6: An illustration showing two views of a A-A collision [14].

In nucleus-nucleus collisions, the initial system's geometry can be primarily characterized by b and the general size and shape of the overlapping region. However, in p-Pb collisions the initial geometry and number of participants are sensitive to the finer details of the spatial distribution of the proton and nucleus. Figure 1.7 shows an

illustration of a proton-nucleus collision. The number of participants depends on the effective path length, L(b), that the proton takes when colliding with the nucleons.

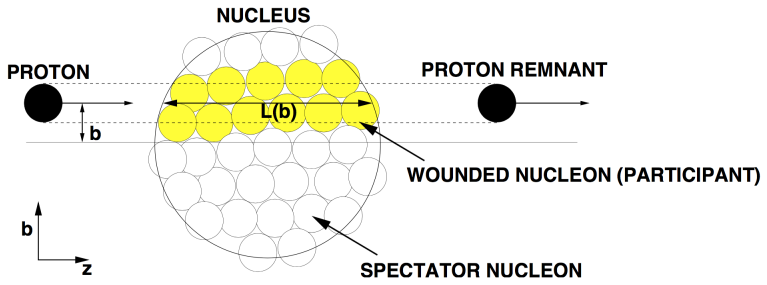


Figure 1.7: Schematic illustration of the impact parameter, b, in a proton-nucleus collision [15].

An impact parameter of $b = 0$ is a perfectly central collision. Central nucleus-nucleus collisions have the most overlap. Central collisions are expected to have the largest number of nucleons participating in the collision (N_{part}) and the largest number of nucleon-nucleon binary collisions, (N_{coll}). The most central events, in general, are classified in the 0-5 percentile centrality class. For 0-5% centrality pPb collisions, $\langle b \rangle = 3.12 \pm 1.39$ fm and $\langle N_{part} \rangle = 15.7 \pm 3.84$ and $\langle N_{coll} \rangle = 14.7 \pm 3.84$ [16].

An impact parameter of $b = R_1 + R_2$ is a peripheral collision. The most peripheral events are in the 80-100 percentile centrality class. For 80-100% centrality pPb collisions, $\langle b \rangle = 7.51 \pm 1.11$fm and $\langle N_{part} \rangle = 2.94 \pm 1.42$ and $\langle N_{coll} \rangle = 1.94 \pm 1.42$ [16].

The geometrical values of the collision such as b, N_{part}, or N_{coll} can not be measured directly. Instead, the centrality has to be estimated using some observable from the collision. For nucleus-nucleus collisions, the energy expelled in the collision and the particle multiplicity are approximately proportional to N_{part}. The centrality can be determined by measuring the particle multiplicity or transverse energy distribution.

As compared to nucleus-nucleus collisions, pPb collisions have a much smaller range of the number of participants. Within the small range of N_{part} there are large fluctuations of particle multiplicity. For p-Pb collisions, the impact parameter is weakly correlated with N_{coll}. Estimating the impact parameter based on the particle

multiplicity or transverse energy in pPb collisions will produce a bias for events that contain high p_T particles. For these reasons, in pPb collisions, it is more difficult to estimate the impact parameter. Figure 1.8 [17] shows a drawing of two pPb collisions. Even though these collisions have the same impact parameter, they have differing number of collisions, number of particles produced, and transverse energy.

Estimating the centrality using transverse energy in a given η region, then measuring a p_T spectrum in the same η region will also produce a biased measurement. To reduce the centrality bias in pPb collisions, one can use observables that are in kinematic regions that are causally disconnected from the measurement's η region. The measurement in this thesis relies heavily on the EMCal detector, with acceptance $-0.7 < \eta < 0.7$. The V0A detector is located at $2.8 < \eta < 5.1$, making it a good candidate for a centrality measurement with minimal bias. The amplitude measured in the V0A is approximately proportional to the number of participants in a pPb collision.

Glauber Monte Carlo simulations with a Woods-Saxon nuclear density distribution is used to relate the impact parameter to information that can be collected from the detector. In the Glauber MC simulations, the impact parameter is varied and the properties of the collision geometry, such as N_{part} is determined. The negative binomial distribution (NBD) is used to describe the probability distribution of the

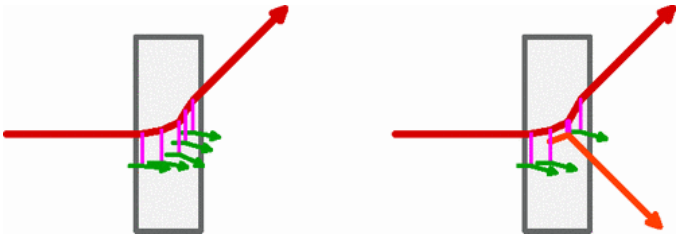


Figure 1.8: Two scenarios for pPb collisions with the same impact parameter [17]. In the left figure, there are many semi-hard collisions and a production of a high p_T particle. In the right figure, there are fewer total collisions and a single hard collision, producing a pair of high p_T particles.

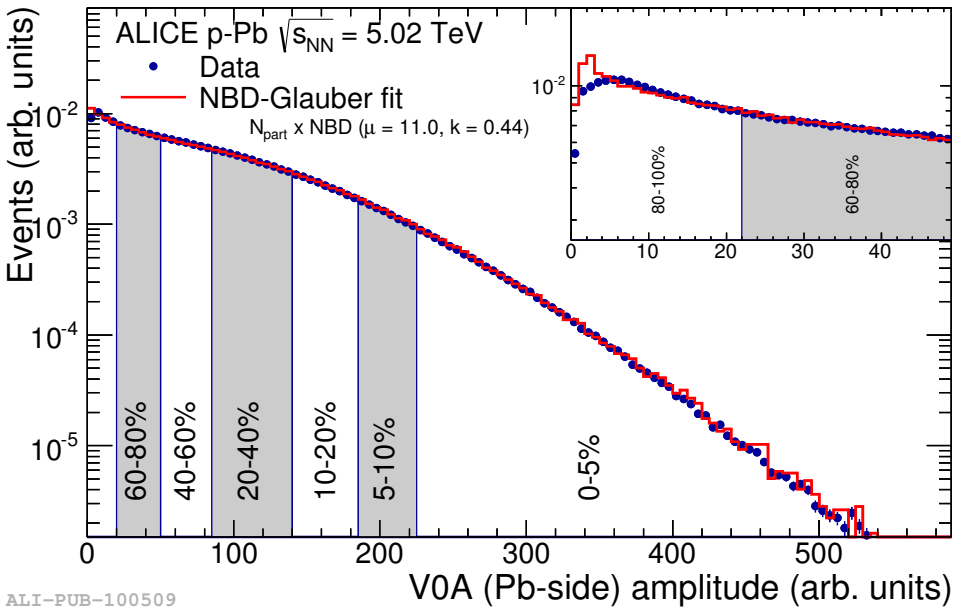


Figure 1.9: Distribution of the amplitudes in the V0A detector [16]. The fit is the negative binomial distribution (NBD). Centrality classes are shown with vertical shading. The top left corner shows a zoom-in on the most peripheral events.

contributions to the V0A multiplicity from each nucleon in the collision. The NBD-Glauber calculation for the V0A amplitude distribution is fit to the pPb data. The NBD-Glauber fit has two parameters: μ, the mean amplitude per participant and k, the dispersion parameter. The parameters μ and k are fit to the V0A amplitude data from pPb collisions, as shown in Figure 1.9 [16].

After the model is fit to the data, each event class can be defined. The 0-5% centrality class is the top 5% central collisions. The mean values for the geometric properties, N_{part} and N_{coll}, are calculated for the generated distribution in each event class. Table 1.3 lists the mean values for impact parameter, cross section, N_{part}, and N_{coll} for pPb collisions found from the V0A distribution [16].

1.4.3 Transverse Energy and Charged Particle Multiplicity

Measurements such as transverse energy and charged particle multiplicity reveal global characteristics of the colliding system. Transverse energy, E_T, is defined as

Table 1.3: Geometric properties of pPb collisions for centrality classes defined by V0A measurements [16].

Centrality	$\langle b \rangle$ (fm), σ (fm)	$\langle N_{part} \rangle$, σ	$\langle N_{coll} \rangle$, σ
0-5%	3.12, 1.39	15.7, 3.84	14.7, 3.84
5-10%	3.50, 1.48	14.0, 3.78	13.0, 3.78
10-20%	3.85, 1.57	12.7, 3.85	11.7, 3.85
20-40%	4.54, 1.69	10.4, 3.93	9.36, 3.93
40-60%	5.57, 1.69	7.42, 3.61	6.42, 3.61
60-80%	6.63, 1.45	4.81, 2.69	3.81, 2.69
80-100%	7.51, 1.11	2.94, 1.42	1.94, 1.42
0-100%	5.56, 2.07	7.87, 5.10	6.87, 5.10

the energy emitted in the plane perpendicular to the beam axis. The total E_T is a sum over all particles emitted in the event, equation 1.6 [18]

$$E_T = \sum_i E_i \sin\theta_i \tag{1.6}$$

where θ_i is the scattering angle for the i'th particle. Since all of the particles prior to the collision are traveling along the beam axis, the E_T of the initial system is zero.

The average transverse energy per unit rapidity, dE_T/dy, measures how much of the initial collision energy was converted into transverse energy directed per rapidity interval. dN_{ch}/dy is the average charged-particle multiplicity per unit rapidity.

Both dE_T/dy and dN_{ch}/dy are often normalized by number of participants, N_{part}. If a quantity scales with N_{part} then it is considered a "soft" process with small momentum transfers.

Figure 1.10 (a) shows $(dE_T/d\eta)/(0.5N_{part})$ and (b) $(dN_{ch}/d\eta)/(0.5N_{part})$ as a function of collision energy for central Au+Au and Pb+Pb collisions for experiments around the world. The PHENIX (Pioneering High Energy Nuclear Interaction eXperiment), STAR (Solenoidal Tracker at RHIC), and PHOBOS (not an acronym) experiment are at the Relativistic Heavy Ion Collider at Brookhaven National Laboratory located in New York. The CMS (Compact Muon Solenoid), ALICE (A Large Ion Collider Experiment), and the ATLAS (A Toroidal LHC ApparatuS)

experiment are at the Large Hadron Collider at the CERN lab in Geneva, Switzerland. The NA49 experiment was situated in the North Area of the Super Proton Synchrotron at CERN. The E802 experiment was at the Brookhaven National Laboratory. FOPI (named after 4π, the solid angle of the detector) was at GSI (Gesellschaft für Schwerionen-forschung) in Darmstadt, Germany. Figure 1.10 (a) and (b) are drawn as a log-log scale. $(dE_T/d\eta)/(0.5N_{part})$ and $(dN_{ch}/d\eta)/(0.5N_{part})$ both appear as a straight line after $\sqrt{s_{NN}} = 7.7$ GeV, demonstrating a power law behavior of the collision energy dependency. $(dE_T/d\eta)/(0.5N_{part})$ and $(dN_{ch}/d\eta)/(0.5N_{part})$ both seem to be consistent with Au-Au and Pb-Pb systems, indicating that transverse energy and charged particle multiplicity scales with the number of participating nucleons.

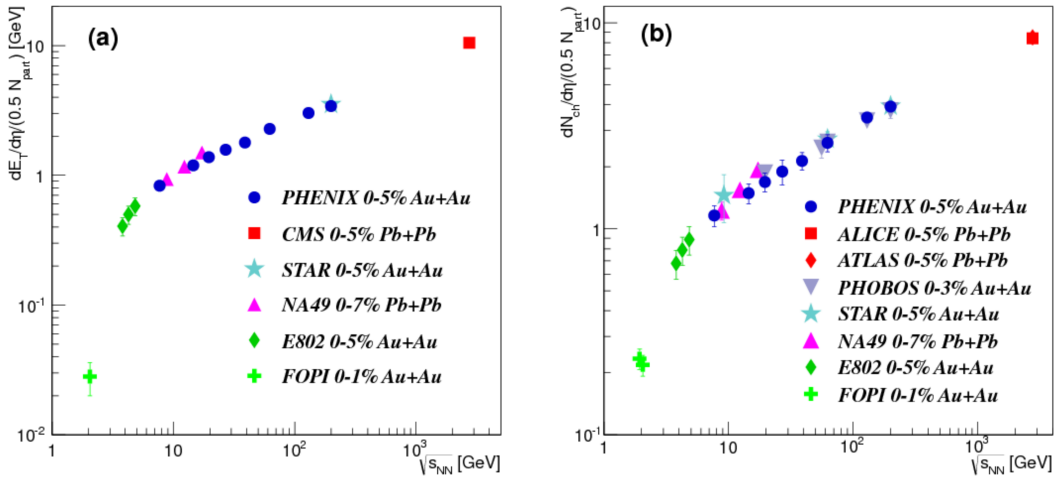


Figure 1.10: (a) Transverse energy per unit pseudorapidity scaled by number of participants, $(dE_T/d\eta)/(0.5N_{part})$, and (b) charged particle multiplicity per unit of pseudorapidity scaled by number of participants, $(dN_{ch}/d\eta)/(0.5N_{part})$, shown as a function of center of mass energy for central Au+Au and Pb+Pb collisions measured in experiments around the world. Data are summarized in [18].

1.4.4 Lund Model

A high energy proton-proton collision or proton-nucleus collision can be modeled with the Lund Model [19] [12]. In this model, the proton is treated as a vortex line

with a hard core surrounded by an exponentially damped field. When two protons collide they transfer momentum becoming longitudinally stretched objects. These longitudinally excited strings will fragment into hadrons. In this model, most of the produced particles will travel along the beam direction. The drawing 1.11 depicts a pair of quarks moving in opposite directions, left and right. Time is represented vertically. Because of confinement, there is a potential $V(r) = \kappa r$ between the pair of quarks. This potential can be described as a string with string tension κ being stretched between the pair. The string tension is $\kappa \approx 1$ GeV/fm [20]. At some point as the pair of quarks moves apart, it is more energetically favorable to pull a pair of quarks out of the vacuum than to stretch the string more. The string breaks and a new quark-antiquark pair are produced.

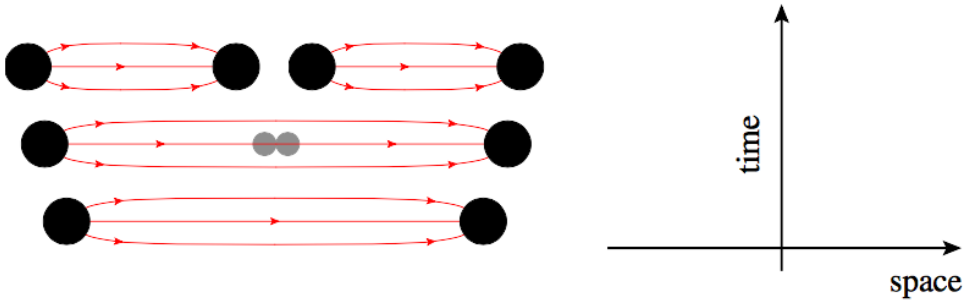


Figure 1.11: String breaking from a quark pair [20]. The x-axis is space and the y-axis is time.

The model for a proton-proton collision is similar to the fragmentation of a string stretched between a $q\bar{q}$ pair produced from the vacuum. In the figure 1.12 particles q_0 and $\bar{q}_0$ are created at the same point in space and time. After the pair is created they move in opposite directions. There is a string stretched between the particles q_0 and $\bar{q}_0$. At some point as the pair q_0 and $\bar{q}_0$ moves apart, the string breaks producing $q_1\bar{q}_1$ pair. Later, the pair $q_2\bar{q}_2$ is produced. A hadron can be formed by $\bar{q}_1$ and q_2. The process of breaking strings and producing $q\bar{q}$ pairs continues until only hadrons remain.

In a similar way, the proton-nucleus collision can also be modeled under the Lund model. The proton is viewed as a projectile that hits a series of n targets as it

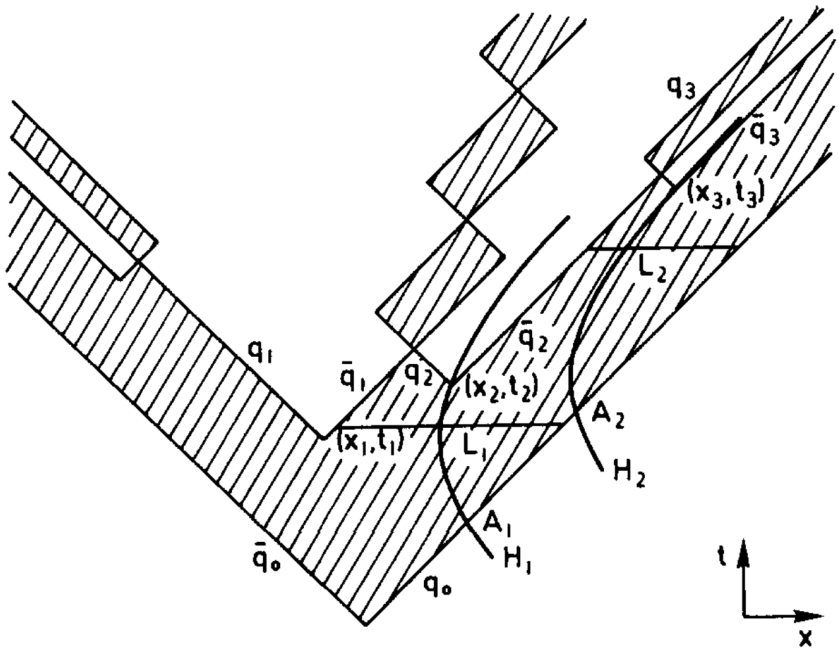


Figure 1.12: The particles q_0 and $\bar{q}_0$ are produced and move apart [21]. The x-axis represents space, while the y-axis represents time.

travels through the nucleus. The number of collisions is calculated by counting all of the nucleons in a cylinder in the projectile's path after giving each nucleon an assigned space coordinate. The time between collisions is smaller than the time that it would take to fragment. Each collision adds to the excitation and mass of the projectile string. After the n collisions there will be a total of $n + 1$ strings, which accounts for the n targets and the string from the projectile. Each string will fragment independently.

1.5 Nuclear Modification Factor

In order to quantify the effect of nuclear matter on the yields of particles produced, the nuclear modification factor can be defined. The nuclear modification factor is usually written as R_{AA}, but different subscripts can be used to signify the collision systems being considered. For p-Pb collisions, R_{pPb} can be defined as

$$R_{pPb} = \frac{dN_{pPb}/dp_T}{\langle N_{coll}\rangle dN_{pp}/dp_T} \tag{1.7}$$

where dN_{pPb}/dp_T is the yield as a function of p_T in p-Pb collisions, $\langle N_{coll}\rangle$ is the average number of binary collisions, and dN_{pp}/dp_T is the yield as a function of p_T in p-p collisions.

An R_{pPb} of unity indicates that p-Pb collisions are a superposition of p-p collisions scaled according to the binary collision assumption. An R_{pA} less than one indicates a suppression of the yield in p-Pb as compared to p-p. R_{pPb} greater than one points to an enhancement in the yield as compared to p-p collisions.

1.6 Cold Nuclear Matter Effects

Physics effects that modify processes in nuclear collisions in absence of or before the formation of the Quark Gluon Plasma are often referred to as Cold Nuclear Matter (CNM) effects. The creation of charm and beauty quarks occurs very early in the collision. Consequently the production of heavy flavor electrons is sensitive to the initial conditions and could be modified by CNM effects.

CNM effects are present in Nucleus-Nucleus, Nucleus-proton and proton-proton collisions. However only the Nucleus-Nucleus collisions are expected to create a QGP and have both cold and hot nuclear matter effects. Studying the CNM in a simpler system such as pPb collisions can help isolate the hot from the cold effects. The CNM effects include the Cronin effect, gluon shadowing, and gluon saturation at small momentum fraction [22].

1.6.1 Cronin Effect

The Cronin effect [23] is seen in nuclear modification factor plots, R_{AA}, as an enhancement, $R > 1$, at moderate p_T [24] as shown in the drawing in Figure 1.13. In other words, the observables at low p_T in pp collisions are "moved" to higher p_T in

pPb collisions. The Cronin effect is attributed to multiple parton scatterings in the initial state through cold nuclear matter before the observed hadrons are produced.

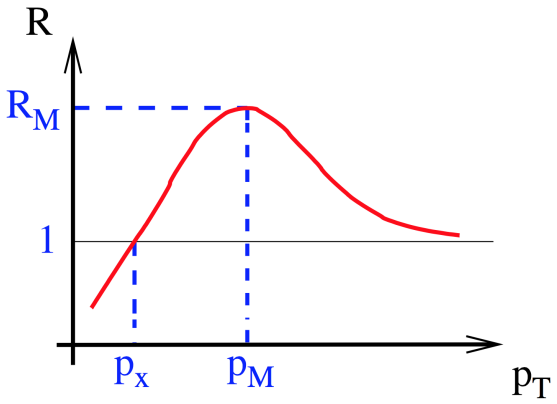


Figure 1.13: Illustration of the Cronin Effect shown in a R_{AA} plot [24].

In the initial stages of p-Pb and Pb-Pb collisions, partons might undergo multiple scattering while they traverse the nuclei before producing heavy flavor quarks. During each collision the parton's direction will change. The average transverse momentum will increase with multiple scatterings. Because of the increase of targets in p-Pb and Pb-Pb collision as compared to p-p collisions, the p_T distribution for heavy flavor electrons will be wider in p-Pb and Pb-Pb collisions as compared to p-p collisions.

The PHENIX experiment at the Relativistic Heavy Ion Collider (RHIC) observed the Cronin effect in the production of heavy flavor electrons in d+Au collisions as compared to p-p collisions at $\sqrt{S_{NN}}$ = 200 GeV [25]. Figure 1.14 shows R_{dA} for heavy flavor decay electrons as a function of p_T for the most-central centrality bins (top plot) and most-peripheral bins (bottom plot). The most-central centrality bins (top plot) shows an enhancement in the region $1.5 < p_T^e < 5$ GeV/c due to CNM effects. The most peripheral centrality collisions have a cross section closer to p-p collisions so it is expected that the peripheral nuclear modification factors (bottom plot) show less enhancement and are consistent with unity.

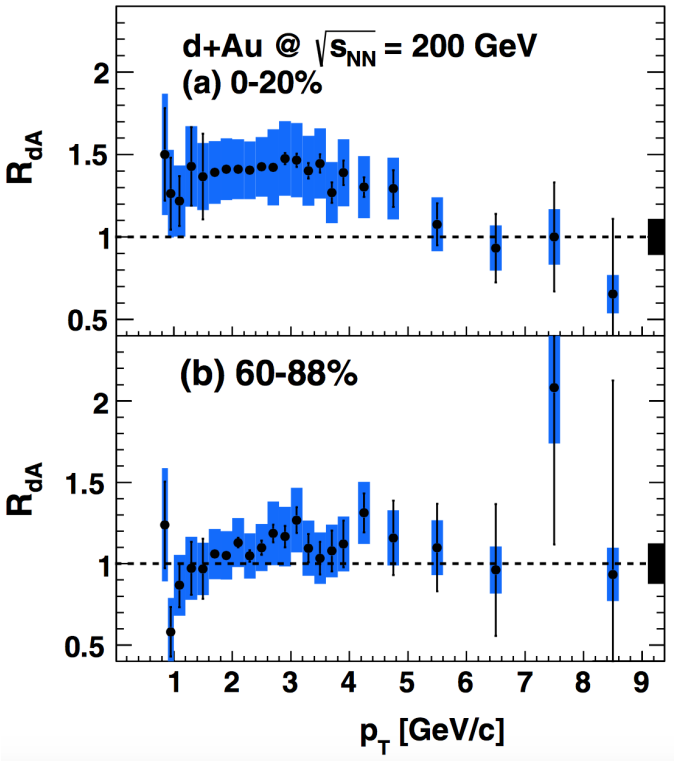


Figure 1.14: R_{dA} for heavy flavor decay electrons as a function of p_T for the most-central centrality bins (top plot) and most-peripheral bins (bottom plot), measured by the PHENIX experiment [25].

1.6.2 Shadowing and Anti-Shadowing

Deep Inelastic Scattering (DIS) of leptons and nucleons has shown that the nucleon parton distribution functions (nPDF) of a bound nucleon differ from a free nucleon [26] [27]. Quark and anti-quark distributions are described as functions of the square of the momentum transfer, Q^2, and the fraction of total momentum carried by a parton, x.

In p-Pb collisions, the partons inside of the proton can collide with more than one nucleon in the lead nucleus. A parton in the proton can "see" in the surface of the target nucleus, but the partons in the back of the target might be shadowed by the partons in front of it. Nucleons *shadowing* each other modify the nPDFs relative to those of the free nucleons. The amount of shadowing depends on Q^2 and x. The

parton density can also be enhanced in the nucleus as compared to the free nucleon, *antishadowing*.

Figure 1.15 shows the ratio, R_i^A, of the bound parton nPDF as compared to the free proton parton distribution function, for a parton flavor i. The shadowing and antishadowing regions are labeled. The EMC effect refers to the effect measured by the European Muon Collaboration. The production of heavy flavor at the LHC is mostly due to gluon fusion, making the gluon nPDF of highest interest. Figure 1.16 shows R_i^A for gluons bound in the lead nucleus at the charm quark mass threshold $Q^2 = 1.69$ GeV^2 for several theoretical nPDF models.

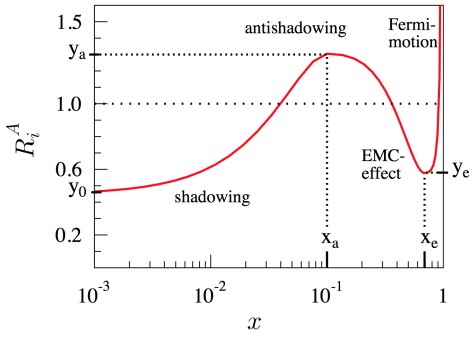


Figure 1.15: Illustration of the nuclear modification factor, R_i^A, of the bound parton as compared to the free proton parton distribution function [27].

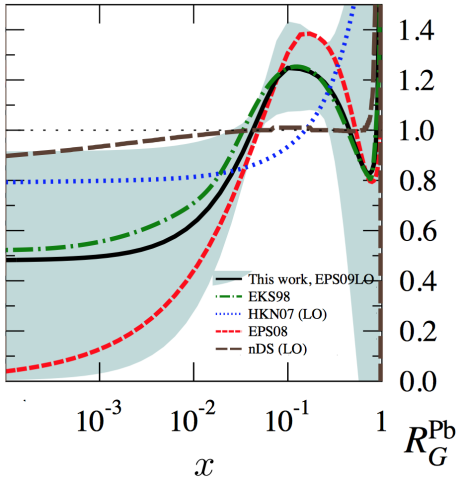


Figure 1.16: Nuclear Modification of the gluon at the charm quark mass threshold as compared to the free proton PDF as a function of momentum fraction, x for the Pb nucleus [27].

Chapter 2

Theoretical and Experimental Status

2.1 QCD prediction of heavy flavor production

Hard partonic scatterings are the main contribution to heavy-quark production. QCD has a running coupling constant α_s, which depends on distance and momentum transfer, Q^2. The coupling constant, α_s, as a function of energy, Q, is shown in Figure 2.1 [5].

The value of α_s increases with large distances, known as the principle of confinement. When trying to pull apart two quarks the energy of the system increases and at some point the energy is larger than creating a quark-antiquark pair. The new quark-antiquark pair then forms hadrons with the original quarks. Quarks are never seen as independent particles over distances greater than 1 fm.

The value of α_s decreases with small distances and high energy, leading to the concept of asymptotic freedom. An important consequence from asymptotic freedom is that at sufficiently large momentum transfers and energies α_s is small enough to use the application of perturbation theory. Since charm and bottom quarks have a large mass, their production can be described by perturbative QCD. The cross section for

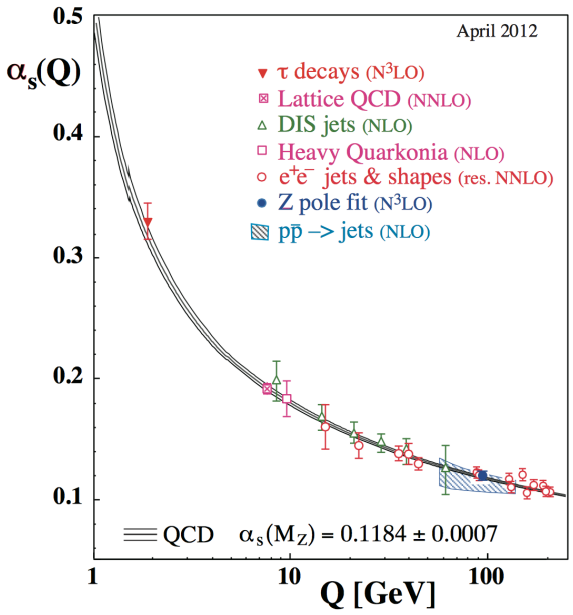


Figure 2.1: Summary of strong coupling constant, α_s, as a function of energy scale Q. The degree of QCD perturbation is shown in parenthesis. (NLO: next-to-leading order; NNLO: next-to-next-to leading order; res. NNLO: NNLO matched with resummed next-to-leading logs; N3LO: next-to-NNLO) [5].

production of heavy flavor can be expressed by a perturbation series in powers of the coupling constant, α_s.

$$\sigma = A_1\alpha_s + A_2\alpha_s^2 + ... \tag{2.1}$$

For cases where the transverse momentum, p_T, of the heavy quark is larger than its mass, m, then large logarithms with the ratio p_T/m emerge in the perturbative expansion. The logarithmic terms in the p_T expansion are classified in terms depending on their order [28]. Terms with the form $\alpha_s^2(\alpha_s \log p_T/m)^k$ are leading-logarithmic terms, or LL. Terms with the form $\alpha_s^3(\alpha_s \log p_T/m)^k$ are next-to-leading logarithmic terms, or NLL.

The order of the calculation has a large effect on the magnitude of the predicted cross section. The introduction of the α_s^3 term was found to double the total cross

section as compared to the α_s^2 calculation for collisions with center of mass energies in the range $10 < \sqrt{s} < 630$ GeV [29].

2.1.1 FONLL

FONLL [28] is a calculation for the production of heavy flavor in hadronic collisions. FONLL stands for "Fixed Order + Next-to-Leading Log". The FONLL approach combines the fixed-order next-to-leading order calculations (FO NLO), and all logarithmic terms summed to the next-to-leading logarithmic terms (NLL). The details of the calculation can be found in [28].

The fixed-order next-to-leading order calculations for the heavy flavor cross section can be written as [28]

$$\frac{d\sigma}{dp_T^2} = A(m)\alpha_s^2 + B(m)\alpha_s^3 + \mathcal{O}(\alpha_s^4) \tag{2.2}$$

The all-order resummation to next-to-leading log calculation can be written as [28]

$$\begin{aligned}\frac{d\sigma}{dp_T^2} = \alpha_s^2 \sum_{i=0}^{\infty} a_i(\alpha_s \log \mu/m)^i + \alpha_s^3 \sum_{i=0}^{\infty} b_i(\alpha_s \log \mu/m)^i \\ + \mathcal{O}(\alpha_s^4(\alpha_s \log \mu/m)^i) + \mathcal{O}(\alpha_s^2 \times PST)\end{aligned} \tag{2.3}$$

The coefficients a_i and b_i depend on the center of mass energy of the collision and p_T. PST are terms that are suppressed in the limit where p_T is large. The value μ is the scale of choice, either renormalization or factorization. The FONLL calculation combines equations 2.2 and 2.3.

FONLL [28] is used in this thesis as a calculation for the production of heavy flavor in pp collisions. The FONLL predictions used in this analysis were obtained from a publicly accessible web page [30].

FONLL has been used for many years now to predict charm and bottom production at the Tevatron and at RHIC. There has been good agreement between

FONLL theory and data. Figure 2.2 [31] shows the cross section for electrons coming from heavy flavor hadrons from the PHENIX and STAR experiment at RHIC. FONLL is drawn as two black lines, representing the theoretical uncertainty band. Theoretical uncertainties in FONLL arise from the uncertainty in the charm and bottom mass, the error in factorization and renormalization scale variations, and the uncertainty in the parton distribution functions. Results have begun to show that FONLL also agrees with the production of heavy flavor at the LHC energies as shown in Figure 2.7.

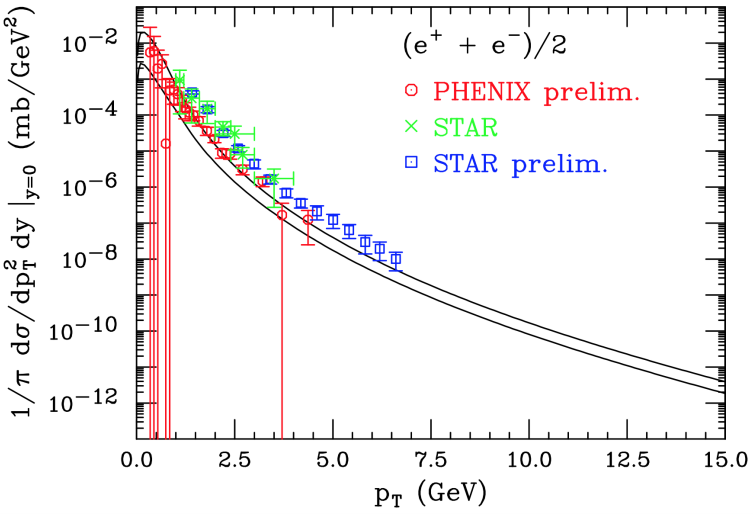


Figure 2.2: Comparison of FONLL to electrons coming from charm and bottom hadron decays at RHIC for pp collisions at $\sqrt{s} = 200$ GeV [31].

2.2 Early Single Lepton Measurements

The first measurement for single electrons from the decays of heavy-flavor was made at CERN in Switzerland with the Intersection Storage Rings (ISR). This measurement was done before the discovery of charm and the source of the single electrons was undetermined at the time. The ISR measured electrons [32] at 90° with respect to the beam line in the region $1.6 < p_T^e < 4.7$ GeV/c in pp collisions at a center-of-mass energy $\sqrt{s} = 52.7$ GeV. Figure 2.3 [32] shows the invariant cross section of single

electrons from that first measurement. The ISR ran from 1971 to 1984 and was the world's first hadron collider, and performed the first proton-proton and proton-antiproton collisions. Many techniques were developed at the ISR that made later accelerator projects possible.

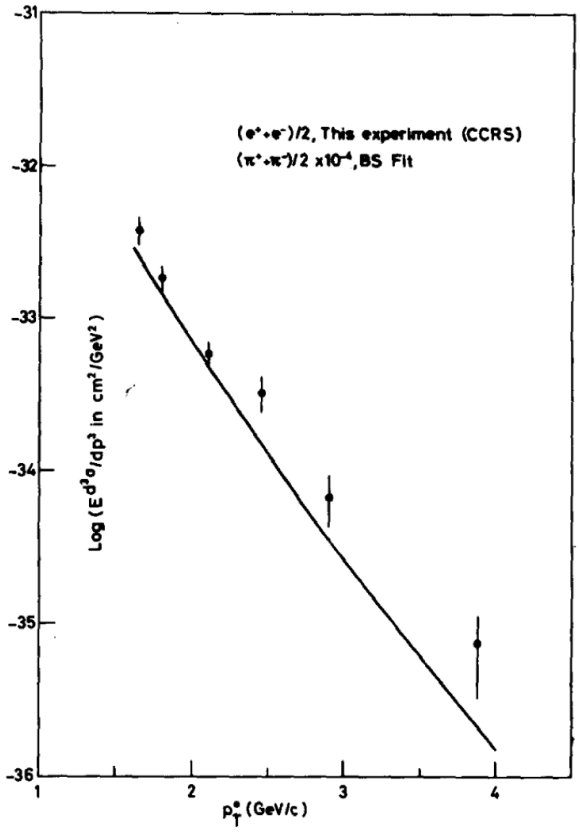


Figure 2.3: One of the first measurements of electrons from heavy flavor decays [32]. Invariant cross section of single electrons as a function of the electron p_T measured by ISR at $\sqrt{s} = 52.7$ GeV. The solid line is the fit to the pion cross-section scaled by a factor 10^{-4}.

The UA1 (Underground Area 1) and UA2 (Underground Area 2) were movable particle detectors at the Super Proton Synchrotron (SPS) collider at CERN in Switzerland. The UA1 and UA2 experiments ran from 1981 to 1990.

UA2 measured semi-leptonic decay of charm to electrons [29] (data from 1985) for the region $0.5 < p_T^e < 2.0$ GeV/c for $p\bar{p}$ collisions $\sqrt{s}$ =630 GeV. The total charm cross section was determined to be $\sigma_{tot}(c\bar{c}) = 0.68 \pm 0.56$ (stat.) ± 0.25 (sys.,

exp.) ± 0.21 (sys., theory) mb. The cross section was compared to other experimental measurements from CERN ISR and the theoretical calculations at the time as shown in figure 2.4. The cross section found from the UA2 measurement is the upper right point in this figure. The experimental cross section measured was found to agree with the theoretical next-to leading order (a_s^3) predictions of the time. However, the experimental errors were too large to make a distinction in the calculation parameters, the charm quark mass and the gluon structure function.

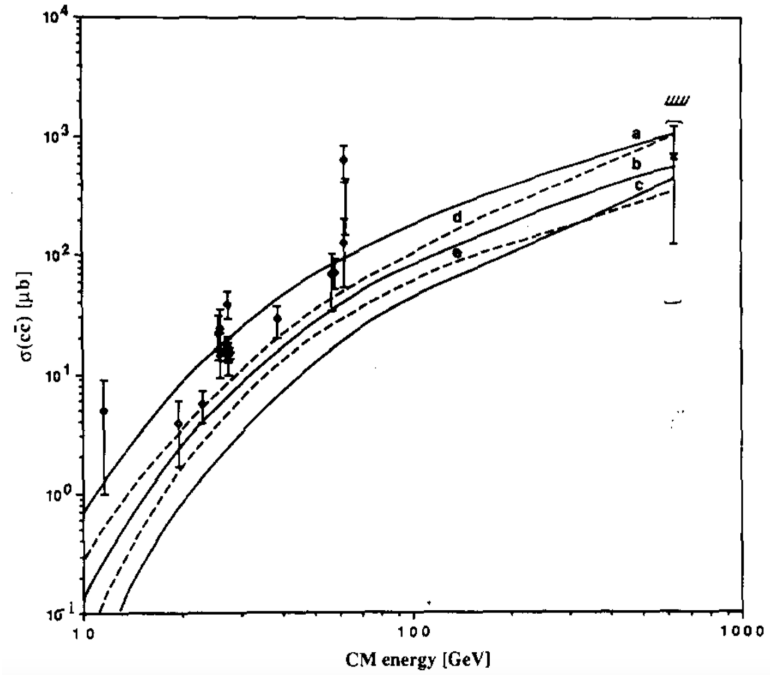


Figure 2.4: Total cross section of charm production as a function of collision energy [29]. The upper right point is $p\bar{p}$ collisions at $\sqrt{s}$ =630 GeV measured by UA2. All other points are pp collisions measured by ISR. The curves represent NLO QCD calculations with various parameters.

UA1 measured bottom production with single muons [33] (data taken 1988-89) in the region $10 < p_T^{\mu} < 40$ GeV/c for $p\bar{p}$ collisions $\sqrt{s}$ =630 GeV. The total production cross-section for b-quarks was measured as $\sigma_{tot}(b\bar{b}) = 19.3 \pm 7(\text{exp.}) \pm 9(\text{th.})\mu\text{b}$. The cross section measured was found to agree across the p_T range with the theoretical next-to leading order (a_s^3) prediction within the experimental error. The theoretical error due to the uncertainty in the bottom quark mass and the gluon structure

function allowed the theoretical prediction to match with a wide variety of values for the cross section.

The Tevatron collider was completed in 1983 and built at Fermi National Accelerator Laboratory (Fermilab) just outside Batavia, Illinois in the United States. Two experiments were at the Tevatron, the Collider Detector at Fermilab (CDF) and the D0 experiment.

During the same time (1988-89) that the UA1 and UA2 experiments were taking data at the SPS, the CDF in Fermilab was measuring bottom production by semileptonic decay electrons [34] in the range $7 < p_T^e < 60$ GeV/c in $p\bar{p}$ collisions at $\sqrt{s} = 1.8$ TeV. The theoretical next-to leading order calculation matched the shape of the p_T distribution of the cross section, but was 1.4 to 2.2 standard deviations lower than the central values in data.

For the same data set (1988-89, $p\bar{p}$ collisions at $\sqrt{s} = 1.8$ TeV), the CDF experiment also measured bottom production using decay muons [35]. This muon measurement [35] only had two p_T^μ bins, $12 < p_T^\mu < 17$ GeV/c and $17 < p_T^\mu < 22$ GeV/c. The experimental cross section measured was compared with the theoretical next-to leading order (a_s^3) prediction. For the lower p_T^μ bin, the central theoretical value was 2.1 standard deviations lower than the experimental value. The theoretical value for the higher p_T^μ bin agreed within experimental error. The NLO QCD calculation underestimates the heavy flavor production cross section.

The D0 detector measured bottom production [36] (data taken 1992-93, $p\bar{p}$ collisions at $\sqrt{s} = 1.8$ TeV) for single muons for the range $3.5 < p_T^\mu < 60$ GeV/c. Figure 2.5 is a summary of bottom production cross sections as a function of the transverse momentum of the b-quark, p_T^b, for the CDF and D0 experiments for single electrons and single muons. The D0 experiment was able to extend the p_T reach and confirm the previous findings from the CDF experiment. The theoretical next-to leading order (a_s^3) prediction is shown on figure 2.5 as a black line. Dotted lines show the theoretical uncertainty. The data and theory agree within errors, but the central value for the theoretical prediction is lower than the data value.

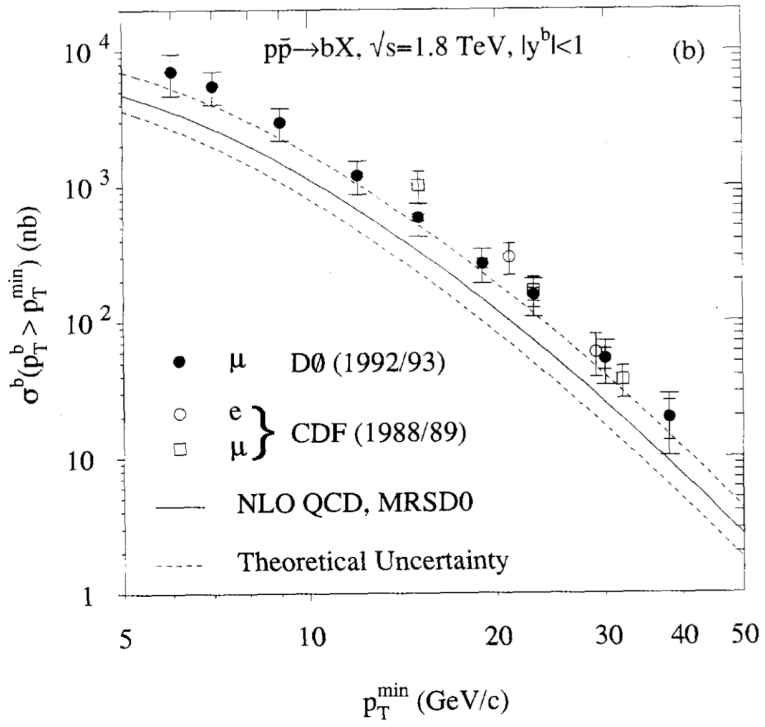


Figure 2.5: The b-quark production cross sections as a function of p_T^b shown for various measurements of inclusive leptons from CDF and D0 experiments at Fermilab [36]. Curves represent the Next-to-Leading Order calculation by Nason, Dawson, and Ellis with MRSD0 parton distribution function.

2.3 Single lepton measurements at RHIC

The PHENIX experiment at the Relativistic Heavy Ion Collider (RHIC) at Brookhaven National Lab saw a suppression of the production of electrons from heavy flavor hadrons in the 2004 run of $Au + Au$ collisions at $\sqrt{s_{NN}} = 200$ GeV as compared to the production in $p + p$ collisions scaled by the number of binary collisions [37]. However, there was a question of whether the suppression seen was caused by a quark-gluon plasma created in the $Au + Au$ collisions or from cold nuclear matter effects.

In order to answer this question, PHENIX measured heavy flavor hadrons in $d + Au$ (deuteron + gold nucleus) collisions at $\sqrt{s_{NN}} = 200$ GeV [25]. The electrons were measured in the momentum range $0.85 \leq p_T^e \leq 8.5$ GeV/c. Figure 1.14 shows

the production of heavy flavor electrons in central and peripheral $d + Au$ collisions compared to the production in p+p collisions scaled by the number of binary collisions, R_{dA}. The central most $d + Au$ collisions show an enhanced R_{dA}, in the range $1.5 < p_T < 5$ GeV/c. This implies that the suppression seen in $Au + Au$ collisions [37] can not be solely explained by initial state effects.

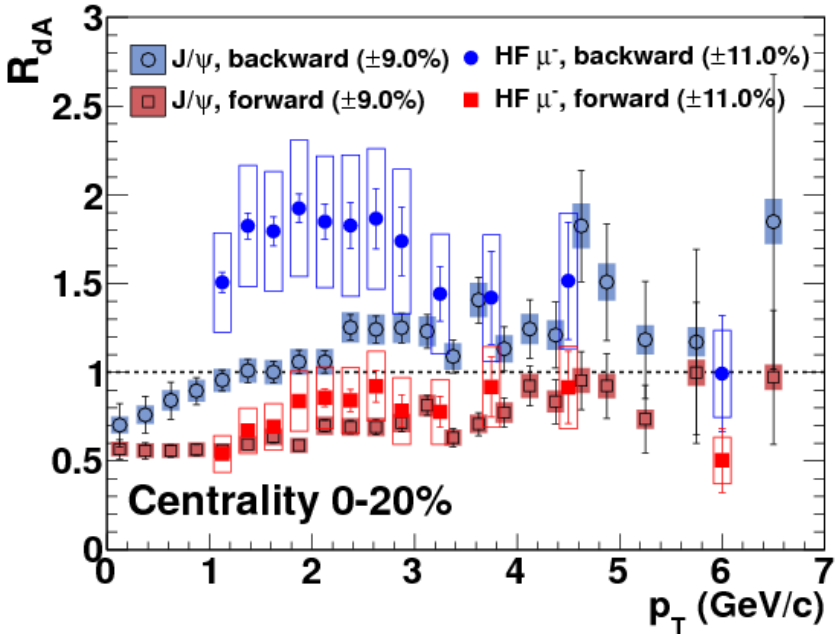


Figure 2.6: J/Ψ and heavy flavor decay muons in $d + Au$ collisions $\sqrt{s_{NN}} = 200$ GeV, for the $0 - 20\%$ centrality class measured by the PHENIX experiment at RHIC [38]. The blue points show the backward, Au-going direction. The red points show the forward, d-going direction.

The PHENIX detector measures electrons at mid-rapidity, at pseudorapidity range $|\eta| < 0.35$ [25]. The muon measurement from PHENIX offers more insight, since the muon detectors are located at forward and backward rapidity and can see the collision at a different angle. PHENIX looked at muons from heavy flavor decays in $d + Au$ collisions at center of mass energy $\sqrt{s_{NN}} = 200$ GeV [38]. Figure 2.6 [38] shows R_{dA} for muons from heavy flavor as compared to the J/Ψ (meson composed of charm and anti-charm). The heavy flavor muons from the Au-going direction, "backward" direction, $-2.0 < y < -1.4$, show an enhancement. The muons in the

d-going direction, "forward" direction, $1.4 < y < 2.0$, show a suppression. It's also interesting to note that the J/Ψ and the heavy flavor muons agree in the forward, d-going direction, but differ in the backward Au-going direction. The J/Ψ are more suppressed as compared to the open-heavy flavor in the Au-going direction. Figure 2.6 shows that the production of heavy flavor depends on initial spatial parameters and closed heavy flavor production is sensitive to cold nuclear matter effects. The leading-order perturbative QCD calculations with nuclear PDFs do not predict the large measured difference in heavy flavor production between Au-going and the d-going direction [38]. Future theoretical models will need to describe these cold nuclear matter effects.

2.4 Single lepton measurements at the LHC

2.4.1 Electrons from heavy flavor in pp collisions

The Large Hadron Collider has collided protons at center of mass energies 2.76, 7, and 8 TeV. Figure 2.7 [39] shows the invariant cross section per unit rapidity of heavy flavor electrons in pp collisions recorded during the 2010 running period for $\sqrt{s} = 7$ TeV. ALICE measured electrons at mid-rapidity ($|y| < 0.5$) and in the low transverse momentum region ($0.5 < p_T < 8$ GeV/c) [39]. Most of the total heavy-flavor production cross section is produced in the low transverse momentum region. In this measurement, a cocktail calculation was used to estimate the production of electrons from various background sources. The experimentally measured neutral pion production cross section was used as the main input for the cocktail calculation. The neutral pion decays to electrons by Dalitz decay and by decaying to photons which can convert to electrons. The production of the light mesons η, η', ρ, ω, and ϕ were calculated from the neutral pion production using transverse mass scaling. More details about the cocktail calculation can be found in reference [39].

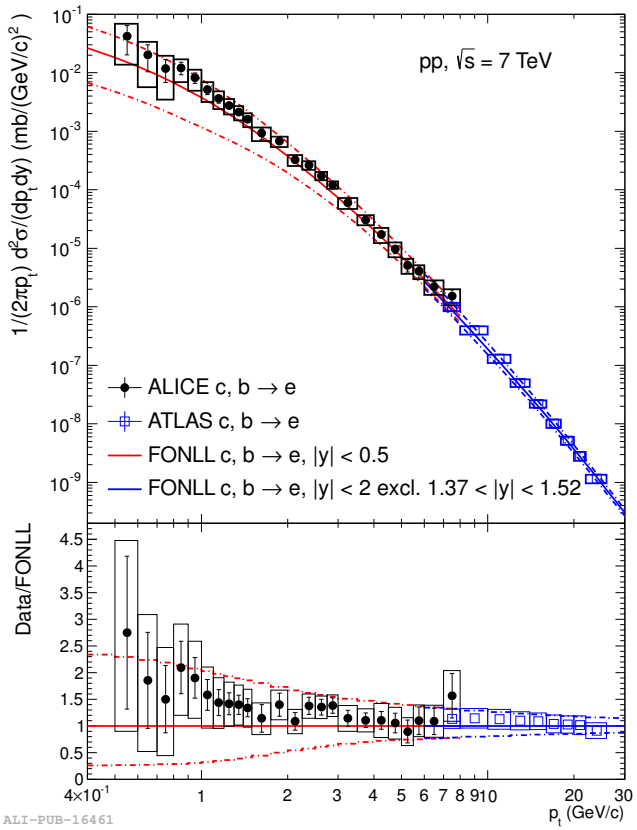


Figure 2.7: Heavy Flavor electrons in ALICE for pp collisions at center of mass energy 7 TeV. Data compared with ATLAS data, at the same energy, and FONLL [39].

Data from ATLAS from the same period in 2010 at $\sqrt{s} = 7$ TeV are superimposed on figure 2.7. ATLAS data extend the p_T reach of the ALICE data, covering $7 < p_T < 26$ GeV/c. ATLAS has a wider rapidity acceptance as compared to ALICE. ATLAS has the rapidity coverage $|y| < 2$ where the regions $1.37 < |y| < 1.52$ are excluded [39]. The data from ATLAS agree with ALICE data.

The FONLL pQCD calculation in the matching rapidity regions for ALICE and ATLAS is also shown on figure 2.7. The FONLL calculation has experimental and theoretical uncertainties due to the factorization and renormalization scales, μ_F and μ_R, and due to the uncertainty of the mass of the charm and bottom quark. The invariant cross section per unit rapidity decreases slightly with a larger rapidity

acceptance. The FONLL pQCD calculation agrees with the ALICE and ATLAS data within the FONLL theoretical uncertainty.

2.4.2 Electrons from heavy flavor in pPb collisions

The Large Hadron Collider collided proton and lead ions, pPb collisions, in 2013. Figure 2.8 shows the p_T differential invariant cross section for electrons from heavy flavor decay hadrons for the minimum-bias pPb collisions at $\sqrt{s_{NN}} = 5.02$ TeV measured in ALICE. Three methods for electron identification are shown using combinations of ALICE detectors: the Time Projection Chamber, Time Of Flight, and Electromagnetic Calorimeter. In this measurement the total transverse momentum range for all three electron identification methods is $0.5 < p_T < 12$ GeV/c. The rapidity coverage for this measurement is $-1.065 < y_{cm} < 0.135$ in the center of mass reference frame, and $-0.6 < y < 0.6$ in the lab frame. The yield of electrons from background sources was subtracted using an invariant mass technique, similar to the method used in this thesis. The invariant mass method takes advantage of the fact that electrons from background sources are mostly produced in e^+e^- pairs.

The nuclear modification factor, R_{pPb}, shows if there are any nuclear effects in pPb collisions as compared to pp collisions. Figure 2.9 [40] shows the nuclear modification factor of electrons from heavy flavor hadron decays in pPb collisions. Data for pp collisions at a matching center of mass energy to pPb collisions are needed to calculate R_{pPb}. However, there was no proton-proton $\sqrt{s} = 5$ TeV data at the time. The pp reference used in figure 2.9 was interpolated from measurements at $\sqrt{s} = 2.76$ TeV and 7 TeV from ALICE and ATLAS. R_{pPb} is consistent with unity with a slight enhancement at transverse momentum $\sim$ 1.5 GeV/c. The pQCD calculation of FONLL + EPS09NLO (nuclear shadowing parametrization) and uncertainties are plotted on figure 2.9.

The pPb measurements shown in figures 2.8 and 2.9 used the minimum bias pPb data. However, the ALICE detector also recorded EMCal triggered data for pPb

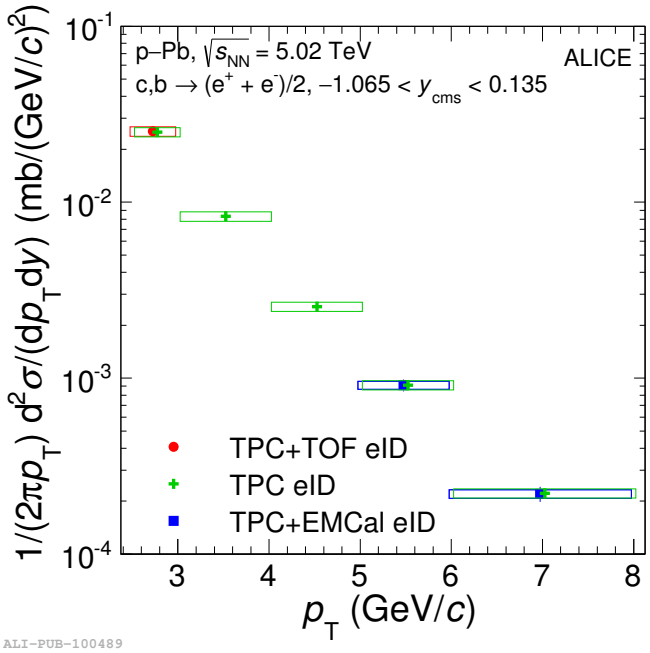


Figure 2.8: Differential invariant cross section for electrons from heavy flavor decay hadrons in minimum bias pPb collisions at $\sqrt{s_{NN}} = 5.02$ TeV measured in ALICE [40].

collisions. Using the EMCal triggered data would extend the p_T reach of the analysis since the trigger makes saving events with energetic particles a priority. This thesis focuses on the EMCal triggered data in order to extend the pPb results for ALICE.

2.4.3 D Mesons at the LHC

ALICE measured the production cross section for prompt D mesons [41] in pPb collisions at the center of mass energy $\sqrt{s_{NN}} = 5.02$ TeV. D mesons were measured in the rapidity interval $|y_{lab}| < 0.5$ which corresponds to the center of mass reference frame $-0.96 < y_{cms} < 0.04$. Prompt charmed mesons D^0, D^+, D^{*+}, D_s^+ and their charge conjugates were measured using their hadronic decay channels, listed in table 2.1. The D meson candidates were found by calculating the invariant mass of two or three tracks from kaons and pions.

The R_{pPb}, nuclear modification factor, is shown for D^0, D^+, D^{*+}, D_s^+ and their charge conjugates in figure 2.10 [41] for the transverse momentum interval $1 < p_T < 24$

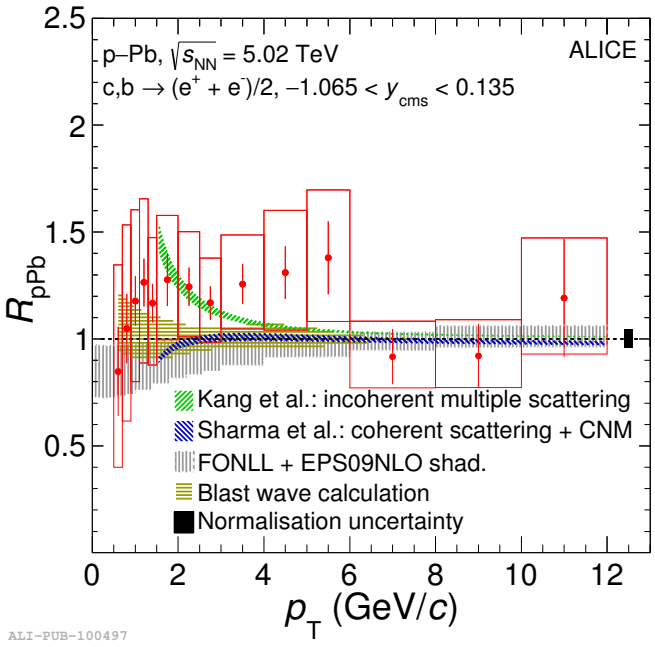


Figure 2.9: Nuclear modification factor, R_{pPb} shown for single electrons from open heavy flavor in pPb minimum bias collisions at $\sqrt{s_{NN}} = 5.02$ TeV measured in ALICE [40].

GeV/c. The R_{pPb} for the four D-mesons agree with unity within the statistical and systematic uncertainties.

The D^0, D^+, D^{*+} mesons species were averaged, weighted by their relative uncertainties. The average R_{pPb} of D mesons is shown in figure 2.11 [41] compared to the R_{PbPb} for central and peripheral Pb-Pb collisions at $\sqrt{s_{NN}} = 2.76$ TeV. The R_{pPb} for D mesons is consistent with unity, showing that the production of D mesons in pPb collisions is what is expected from binary collision scaling of the production of D mesons in pp collisions. However, the production of D mesons in Pb-Pb collisions show suppression. The most central, 0-20% centrality, collisions show the most suppression. Since the nuclear modification factor for D mesons in pPb collisions is consistent with unity, then the suppression of D mesons seen in Pb-Pb collisions can not be due to initial state effects. Figure 2.11 shows a strong case for the presence of hot partonic matter created in Pb-Pb collisions.

Table 2.1: D-mesons and their hadronic decay channels measured with the ALICE detector with the invariant mass method [41].

Decay channels measured	Branching Ratio
$D^0 \to K^+\pi^-$ and $\bar{D}^0 \to K^-\pi^+$	3.88 ± 0.05%
$D^+ \to K^-\pi^+\pi^+$ and $D^- \to K^+\pi^-\pi^-$	9.13 ± 0.19 %
$D^{*+} \to D^0\pi^+ \to K^-\pi^+\pi^+$ and $D^{*-} \to D^0\pi^- \to K^-\pi^+\pi^-$	67.7 ± 0.5 %
$D_s^+ \to \phi\pi^+ \to K^+K^-\pi^+$ and $D_s^- \to \phi\pi^- \to K^-K^+\pi^-$	2.28 ± 12%

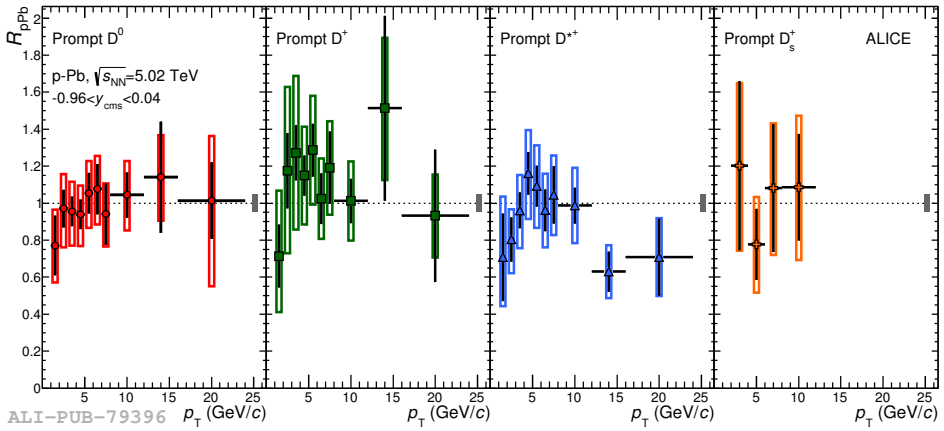


Figure 2.10: R_{pPb} of D^0, D^+, D^{*+}, D_s^+ and their charge conjugates measured [41] in the ALICE experiment at the LHC for pPb collisions at $\sqrt{s_{NN}} = 5.02$ TeV.

2.4.4 B Mesons at the LHC

CMS measured production cross sections of B^+, B^0, and B_s^0 mesons and their charge conjugates ($B^-, \bar{B}^0$, and $\bar{B}_s^0$) by their hadronic decays in pPb collisions at $\sqrt{s_{NN}} =$ 5.02 TeV with the CMS detector at the CERN LHC. Table 2.2 shows the hadronic decay modes used for B^+, B^0, and B_s^0 and their branching ratios. B mesons candidates were identified by first finding two muons of opposite charge with an invariant mass near the J/ψ mass. Then the J/ψ candidate was combined with charged tracks to create a B-meson invariant mass distribution. Tracks were reconstructed with the interval $|\eta_{lab}| < 2.5$ and muons in the interval $|\eta_{lab}| < 2.4$.

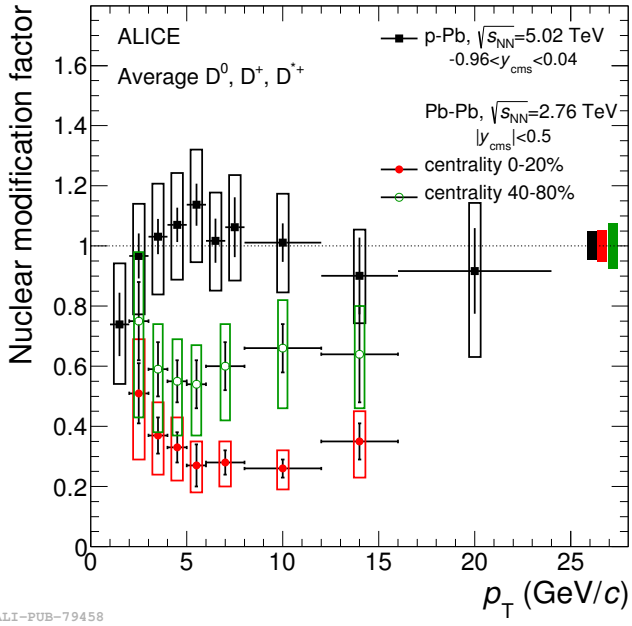


Figure 2.11: Nuclear modification factor shown for D meson production in pPb collisions at $\sqrt{s_{NN}} = 5.02$, and central and peripheral Pb-Pb collisions at $\sqrt{s_{NN}} = 2.76$ TeV. All three are measured [41] by the ALICE experiment at the LHC.

The nuclear modification factor for B^+, B^0, and B_s^0 and ($B^-, \bar{B}^0$, and $\bar{B}_s^0$) mesons compared to the pp cross sections obtained from FONLL (fixed-order plus next-to-leading-logarithm) calculations are shown in figure 2.12. The R_{pPb}^{FONLL} is shown for the transverse momentum range $10 < p_T < 60$ GeV/c. The modification factor for all B mesons species are consistent with unity. No significant suppression or enhancement is observed as compared to pp perturbative QCD calculations scaled by the number of binary collisions.

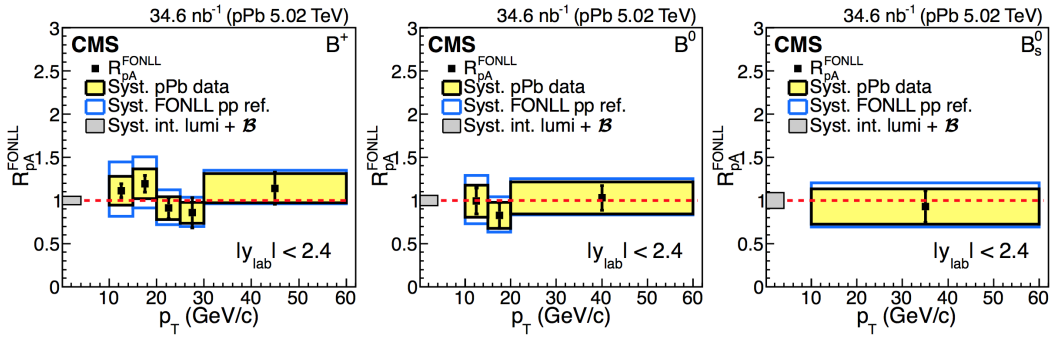


Figure 2.12: B meson production in pPb $\sqrt{s_{NN}} = 5.02$ TeV collisions as compared to the FONLL pp prediction as measured [42] in the CMS experiment at the CERN LHC. Shown are B^+ (left), B^0 (center), B_s^0 (right) with transverse momentum range $10 < p_T < 60$ GeV/c.

Table 2.2: B-mesons and their hadronic decay channels measured in the CMS detector with the invariant mass method [42].

Decay channels measured	Branching Ratio
$B^0 \to J/\psi + K^*(892) \to \mu^+ + \mu^- + K^+ + \pi^-$	$(5.24 \pm 0.24) \times 10^{-5}$ %
$B^+ \to J/\psi + K^+ \to \mu^+ + \mu^- + K^+$	$(6.12 \pm 0.19) \times 10^{-5}$ %
$B_s^0 \to J/\psi + \phi \to \mu^+ + \mu^- + K^+ + K^-$	$(3.12 \pm 0.27) \times 10^{-5}$ %

Chapter 3

Experimental Overview

This chapter describes the ALICE detector and the sub-detectors primarily used in this analysis. The VZERO, or V0, described in section 3.3, provides a trigger to record physics event data. Particle tracking is supplied by the Inner Tracking System, section 3.4, and the Time Projection Chamber, section 3.5. The Electromagnetic Calorimeter, section 3.6, provides an energy measurement. The EMCal was the primary detector used for identifying electrons in this analysis and is a major focus of this chapter. The information from the detectors for each saved event is summarized in data files, section 3.7.

3.1 Large Hadron Collider

The Large Hadron Collider at CERN (European Organization for Nuclear Research) is located on the border of France and Switzerland and is the largest and highest energy particle accelerator in the world. The LHC was designed to collide opposing beams of protons or heavy ions. During the years 2011 to 2013, the LHC has provided proton-proton collisions (p-p) at energies $\sqrt{s} = 2.76$, 7, and 8 TeV. In November and December of 2011, the LHC collided two beams of fully stripped lead ions, (Pb-Pb), at $\sqrt{s}_{NN} = 2.76$ TeV. In January and February of 2013, the LHC collided protons

and lead ions (p-Pb) at $\sqrt{s}_{NN} = 5.02$ TeV. The LHC shut down from 2013 to 2015 for a planned upgrade.

The tunnels of the LHC are about 100 m underground below the border of France and Switzerland and are 27 km in circumference. Inside the tunnels are superconducting magnets that guide and accelerate protons or lead ions. The beams circulate inside of the magnets, one clockwise and one counterclockwise, and cross at 8 fixed points known as interaction regions. The experiments ALICE, ATLAS, CMS and LHCb are situated at four of these interaction regions. For more information about the technical details of LHC, see reference [43].

3.2 ALICE Experiment

The ALICE detector [44] was specifically designed with an aim to study heavy-ion collisions. The ALICE detector is 26 m long, 16 m high and 16 m wide. It is located underground at Point 2, the second interaction region of the LHC, in St. Genis-Pouilly in France. The detector is shown schematically in Figure 3.1 [44]. The people drawn in front of the detector give a reference of size.

The collisions provided by the LHC take place at the center of the ALICE detector, inside a beam pipe that is 3 cm in radius. The ALICE detector consists of a large number of detector subsystems wrapped around the beam pipe like layers of an onion. The detector systems are all contained inside a solenoidal magnet with a magnetic field of 0.5 T. For this analysis the VZERO and Electromagnetic Calorimeter (EMCal) were used for event triggering. The Inner Tracking system (ITS), the Time Projection Chamber (TPC) and EMCal were used for tracking and particle identification. The ALICE detector subsystems were calibrated during months of running with cosmic rays in 2008 and 2009.

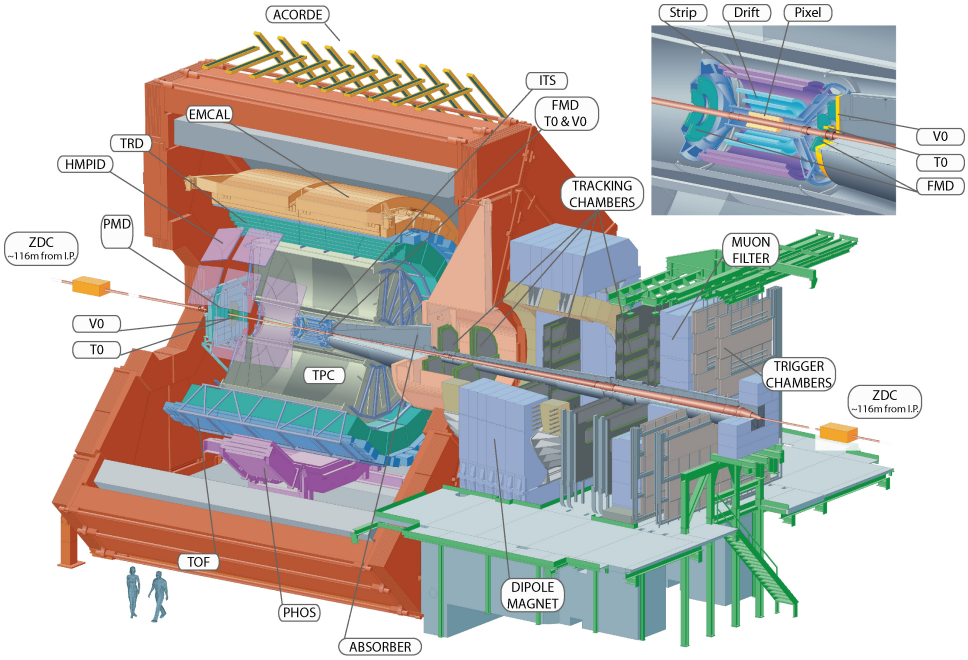


Figure 3.1: The ALICE experiment [44].

3.2.1 ALICE coordinate system

The coordinates primarily used are z, η, and ϕ. Figure 3.2 shows a drawing of the ALICE detector, cut in half and viewed from the side. Only a few of the inner detectors are drawn. In this figure, the z and y directions are labeled. The beam direction is along the z direction. The z = 0 position is the approximate region where the beams cross and collisions occur, called the interaction point. The positive z direction is towards the left of figure 3.2, towards the A side. The C side is in the negative z direction and on the right of the figure towards the Muon Spectrometer. The positive y direction is pointing up towards the sky. The positive x direction is pointing out of the page in figure 3.2. The azimuthal angle is ϕ, which has a range $0 < \phi < 2\pi$ and rotates through the page. The polar angle is related to pseudorapidity, η, where $\eta = -\ln[\tan(\theta/2)]$ and θ is the polar angle with respect to the beam line.

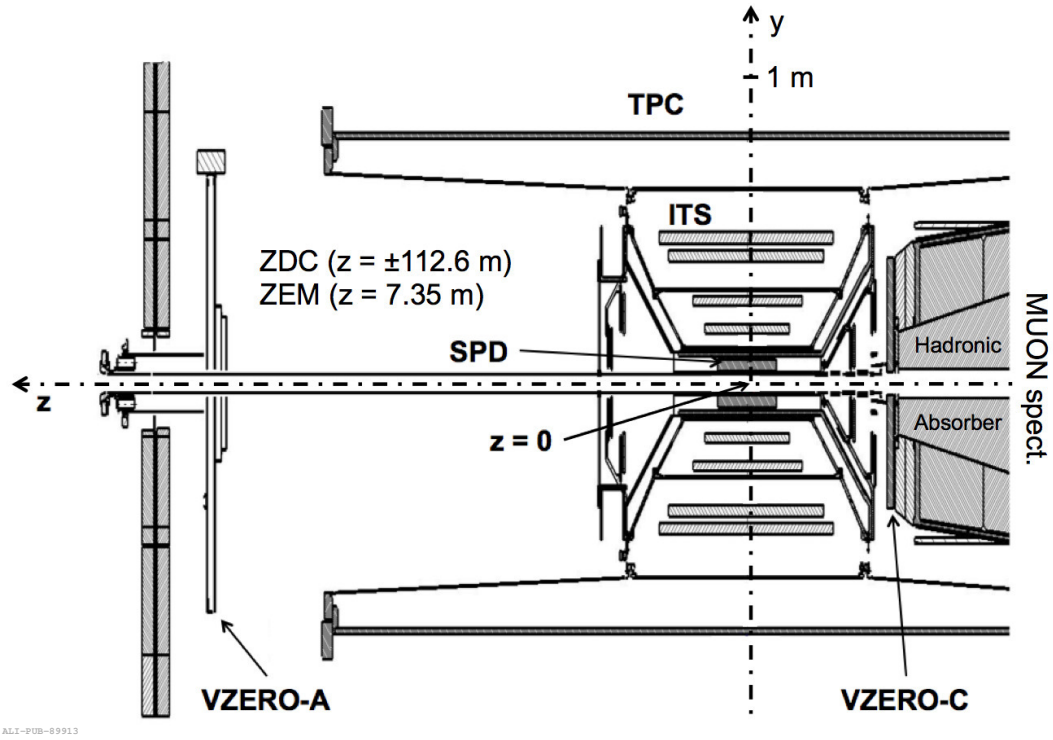


Figure 3.2: The position of the VZERO-A and VZERO-C in ALICE with respect to some of the inner most detectors in ALICE. The beam line is along the z axis [45].

3.3 VZERO

The role of the ALICE VZERO system is to provide a trigger for the ALICE experiment so that the background events such as beam gas interactions can be separated from real physics events. The VZERO also measures basic event characteristics such as centrality, multiplicity, and reaction plane direction. The VZERO also monitors the LHC beam conditions and can measure luminosity.

3.3.1 Design of the VZERO

The VZERO system is located in the forward regions of the ALICE detector. It is composed of two disks which are placed on either side of the interaction region [45] [46]. The VZERO-A is located on the A side of ALICE and VZERO-C on the C side. Figure 3.2 [45] shows the position of the V0-A and V0-C in ALICE with respect to

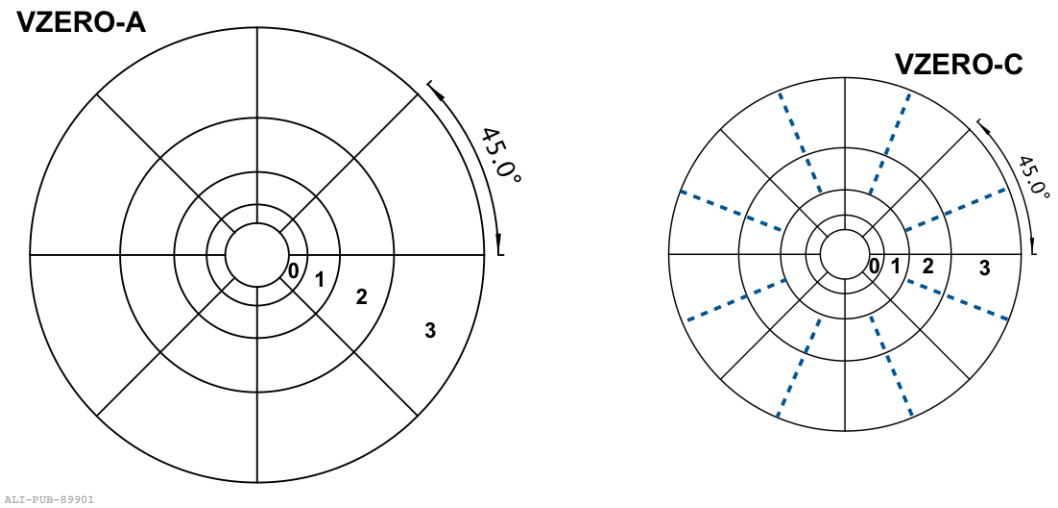


Figure 3.3: Diagram of the VZERO-A and VZERO-C detector subsystems in ALICE showing the scintillator segmentation and relative size [45].

a few other detectors. The V0A is located farther away from the interaction point as compared to the V0C. The V0A was installed in the positive z-direction 329 cm away from the interaction point. The V0C was placed in the negative z-direction 86 cm away from the interaction point. The VZERO-A covers the pseudorapidity range $2.8 < \eta < 5.1$ while the VZERO-C covers the range $-3.7 < \eta < -1.7$ [45].

Figure 3.3 shows the V0A and V0C schematically. Both of the VZERO arrays are composed of four rings with each ring having eight sections, making a total of 32 channels for each array [45] [46]. The V0A disk has a radius $4.3 < r < 41.2$ cm. The V0C is smaller with a radius $4.5 < r < 32.0$ cm. The VZERO arrays are made out of plastic scintillator and have a thickness of 2.5 and 2.0 cm for the V0A and V0C respectively. The scintillator provides a signal when hit from incoming particles by absorbing energy and emitting light. Light is then transferred through wave-length shifting fibers that are attached to the scintillator. The light travels to photomultiplier tubes (PMT) which convert the light into an electronic signal. The signal is then sent to the Front End Electronics (FEE). The time of a signal relative to the LHC clock time and charge from the PMT is measured.

3.3.2 VZERO Event trigger

There is some residual gas in the LHC vacuum chamber which will interact with the beam and produce particles that can hit the VZERO. These events are beam-gas events and considered background events where the data should not be saved. The VZERO is used to decide if an event was a beam-beam event or a background event. The background events can be separated from real physics events by using precise time measurements from the VZERO.

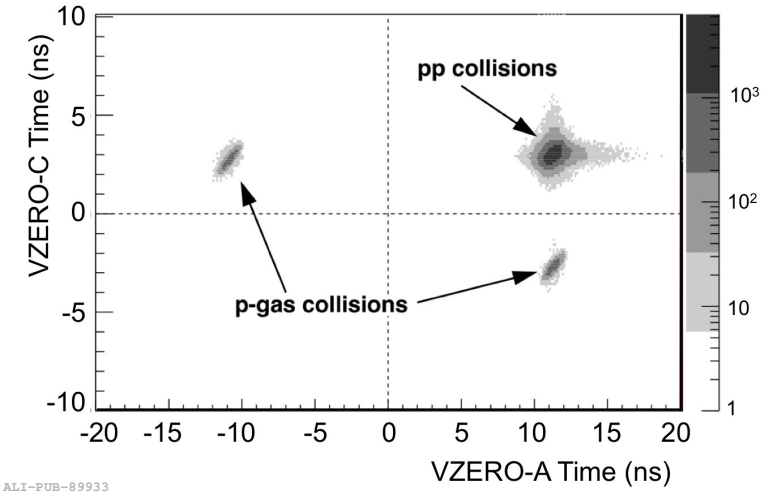


Figure 3.4: Time of flight for beam-beam and beam-gas events measured by the VZERO detector in ALICE [45].

The VZERO can discriminate between physics events and background events by using the time-of-flight difference between the V0A and V0C arrays [45] [46]. There is about a 6 ns difference between real beam-beam events and beam-gas events. Particles coming from the interaction point during beam-beam physics events will take 11 ns (with respect to the LHC clock time) to hit the VZERO-A, and 3 ns to hit the VZERO-C. The time of flight difference for these beam-beam physics events is about 8 ns. The time of flight difference for beam-gas events is about 14 ns. This is caused by a coincidence of a signal coming from the C side to the V0A with a time of 11 ns and a signal coming from the A side to the V0C with a time of -3 ns. It is also caused by a signal coming from the A side to the V0C with a time of 3 ns and a signal

coming from the C side to the V0A with a time of -11 ns. This is shown in Figure 3.4 [45]. The beam-beam events (pp collisions) are shown in the upper right quadrant with a VZERO-A and VZERO-C time of flight of 11 and 3 ns. The beam-gas (p-gas collisions) are shown in the upper left and lower right quadrant and have a time of flight of -11, 3 ns and 11, -3 ns in the VZERO-A and VZERO-C. The darkness of the points in the plot corresponds to the density of counts.

3.3.3 VZERO Centrality and Multiplicity measurement

The VZERO system can provide a charged particle multiplicity measurement based on the energy deposited in the scintillator arrays and this signal is often used for centrality determination. The centrality measurement is explained in detail in section 1.4.2.

3.4 Inner Tracking System

The Inner Tracking System is the innermost detector in ALICE. The ITS sits between the beam pipe and the Time Projection Chamber. The ITS provides a measurement of primary vertex, particle identification, and particle momentum and position measurements. Refer to figure 3.2 for a graphic of the cross section and location of the ITS as compared to the other inner detectors in ALICE.

The ITS is made up of six layers and is drawn schematically in figure 3.5. In figure 3.5, the beam pipe is drawn as a copper colored tube that goes left to right across the middle of the picture. The proton and lead ions travel in bunches inside of the beam pipe. Collisions occur in the center of the detector, near the middle of the picture, and particles created in the collision will travel outwards through the layers of the detector. The first layer of the ITS surrounds the beam pipe. The Silicon Pixel Detector, SPD, comprises the first and second layer of the ITS. The inner layer of the SPD has a pseudorapidity coverage $|\eta|$ <1.75, a wide coverage. The rest of the ITS

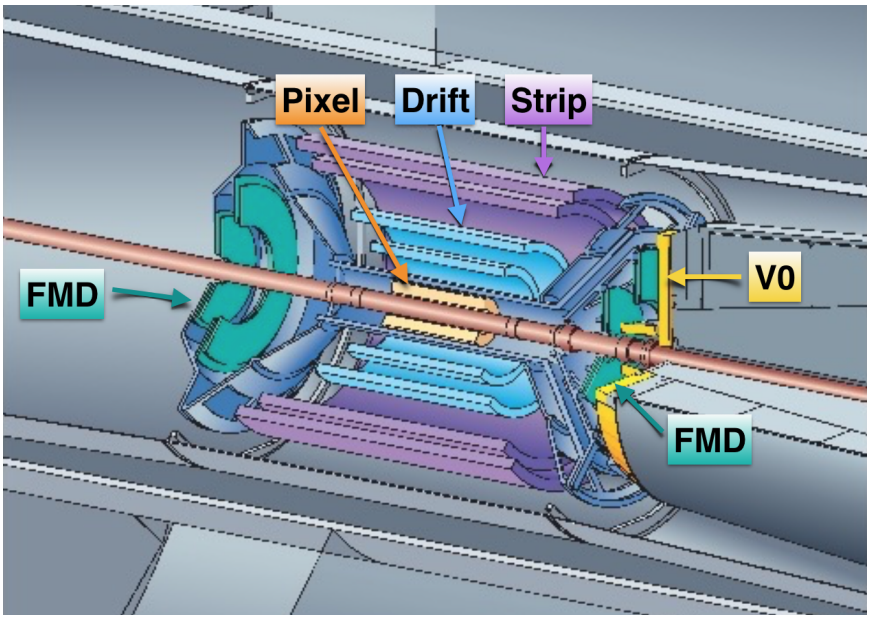


Figure 3.5: The layout for the ALICE Inner Tracking System [47]. The ITS is composed of the Silicon Pixel Detector, Silicon Drift Detector, Silicon Strip Detector. Also shown is the Forward Multiplicity Detectors (FMD) and V-Zero (V0) detector which provide centrality measurement and event triggers.

and the TPC spans $|\eta| < 0.9$. The third and fourth layer of the ITS, the Silicon Drift Detector, SDD, are drawn in blue on figure 3.5. The fifth and sixth layer of the ITS, the Silicon Strip Detector, SSD, are shown in purple in the figure. Table 3.1 [48] lists the dimensions and the detector types of the ITS layers.

Table 3.1: Active Areas of the ALICE Inner Tracking System [48]

Layer	Detector Type	Radius (cm)	$\pm z$ (cm)	Area (m^2)
1	pixel	4	16.5	0.09
2	pixel	7	16.5	0.18
3	drift	14.9	22.2	0.42
4	drift	23.8	29.7	0.89
5	strip	39.1	45.1	2.28
6	strip	43.6	50.8	2.88

The ITS provides a good measurement of the primary vertex and of secondary vertices for particles, such as D and B mesons, that decay near the primary vertex. The SPD, SDD, and SSD have spatial resolutions ($r\phi \times z$) of 12×70, 38×28, 20×830

μm respectively [48]. Figure 3.6 [48] shows the ITS resolution of the distance of closest approach from the track to the primary vertex as a function of p_T for various particle species. D and B mesons have a decay length, or impact parameter, of $\sim$ 300 - 500 μm. The electrons from the decays of D and B mesons measured in this experiment have a transverse momentum $p_T > 1$ GeV/c. The resolution of the impact parameter from the ITS is excellent for electrons from heavy flavor mesons.

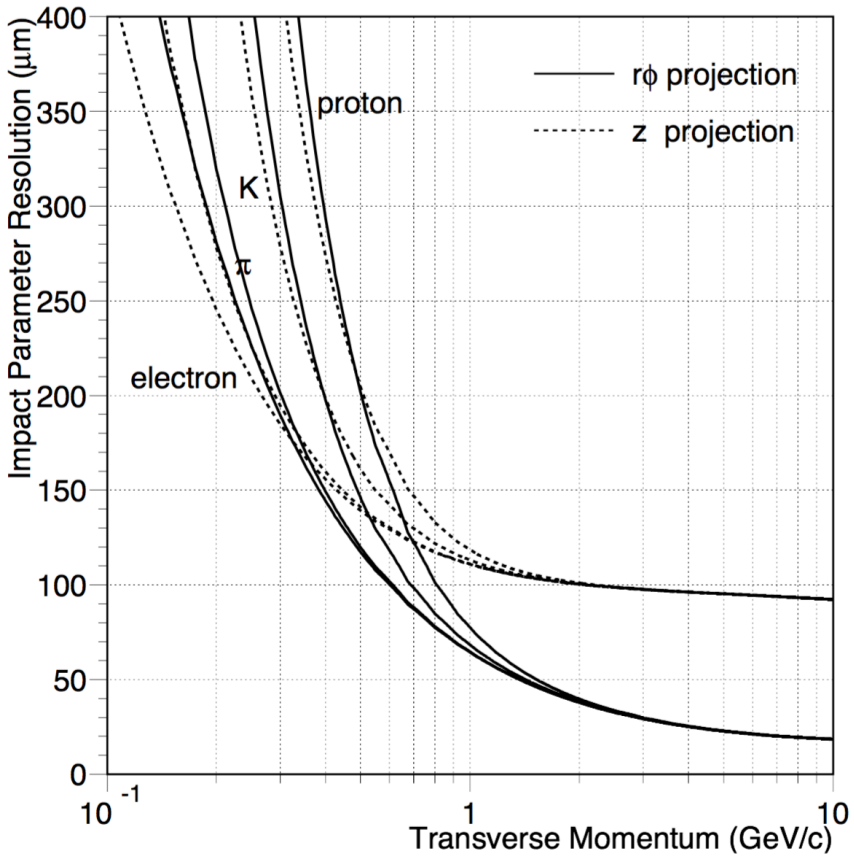


Figure 3.6: Performance of the ITS on the impact parameter resolution with respect to transverse momentum for protons, kaons, pions and electrons [48].

The drift and strip layers in the ITS perform particle identification using dE/dx, specific energy loss. The dE/dx measurement uses the fact that a charged particle ionizes the detector material as it crosses the detector. A drift field pushes the electrons freed from the ionization to read-out pads at the edge of the detector. Figure 3.7 shows particle identification using the ITS for pPb collisions in ALICE.

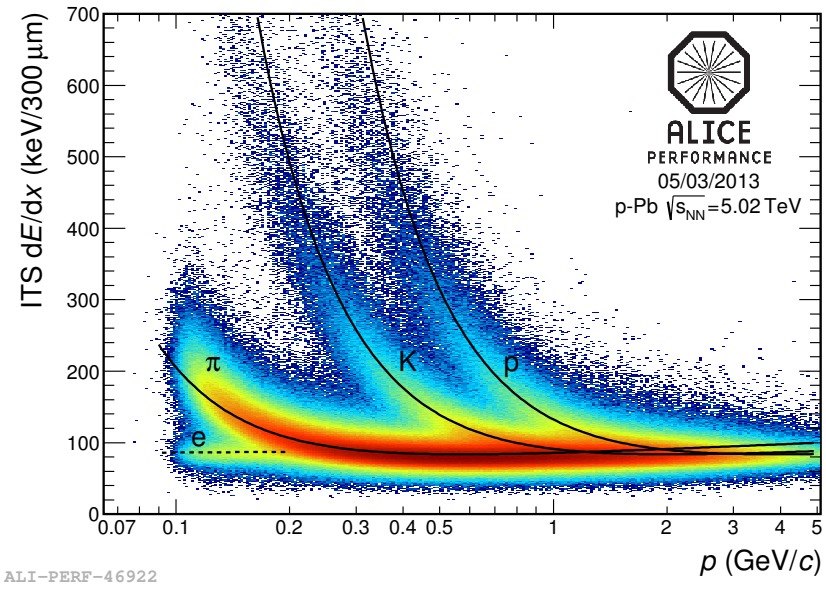


Figure 3.7: Particle identification in the ITS [49]. The dE/dx of charged particles as a function of momentum is shown for minimum bias pPb collisions at $\sqrt{s} = 5.02$ TeV measured in ALICE. The color shows the density of hits; red is the highest and blue is the lowest. The black lines show the parametrization of the detector response based on the Bethe-Bloch formula for electrons, pions, kaons, and protons.

The ITS is wonderful for separating low momentum particles, $p < 1$ GeV/c. However for particles with momentum greater than 1 GeV/c, the ITS can not identify particle species. Since this analysis is focused on electrons with $1 < p_T < 30$ GeV/c, the ITS is not used to identify electrons in this analysis.

The Time Projection Chamber (see section 3.5 for more information on the TPC) is a much larger and deeper detector with more space points than the ITS. For this reason, the TPC provides the main particle tracking in ALICE. However, the ITS improves on the momentum, impact parameter, and position measurements. The outer layers of the ITS connect the tracks from the ITS and TPC. The ITS improves the low momentum range of ALICE, and can track particles as low as $p \sim 0.1$ GeV/c.

3.5 Time Projection Chamber

The ALICE Time Projection Chamber [50] [51] is the main tracking detector in ALICE. The TPC can provide particle identification and momentum measurement for charged particles with transverse momentum, $p_T < 10$ GeV/c.

The TPC is shaped as a cylinder with the center axis along the beam line. Figure 3.8 shows a drawing of the TPC and components. The TPC has a volume of about 95 m^3, with an inner radius of 85 cm and an outer radius of 250 cm and length of 510 cm. This translates to a coverage of pseudorapidity in the range $-0.9 < \eta < 0.9$ and azimuthal range of $0 < \phi < 2\pi$. The TPC sits inside of the 0.5 T solenoidal magnetic field. The TPC is filled with gas that is a mixture of neon, carbon dioxide, and nitrogen. A conducting electrode, charged to 100 kV, divides the detector in half creating two drift regions of 250 cm in length. The TPC has a uniform electric field of 400 V/cm that runs parallel to the beam line.

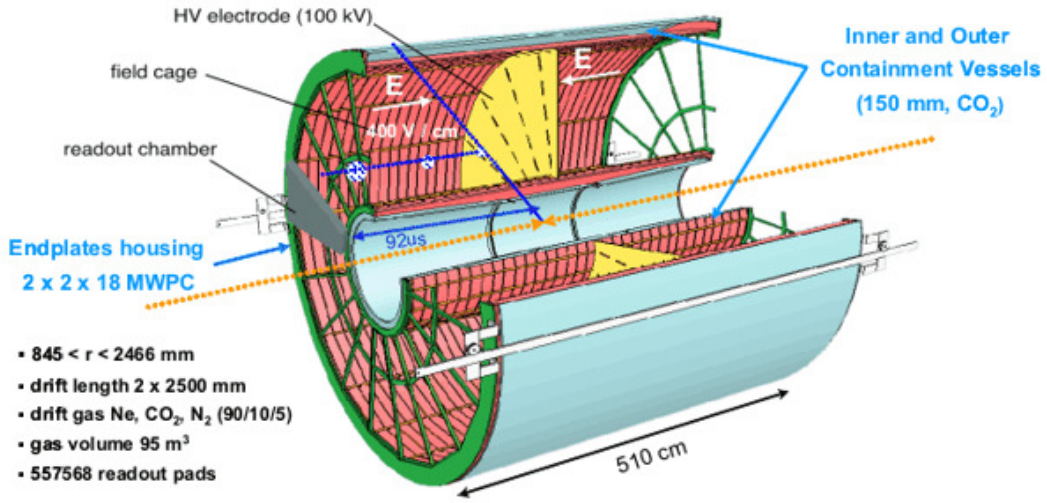


Figure 3.8: The layout for the ALICE Time Projection Chamber [52].

3.5.1 Charged particles interactions with the TPC

When charged particles travel through the TPC, they will trace out a path by ionizing the gas liberating electrons on the way. Due to the electric field, the free electrons drift to the ends of the TPC to the readout pads. The position, r and ϕ, and time of the hit on the end plates by the ionization electrons is recorded. Then the position along the beam axis, z, can be determined using the arrival time and the known drift velocity. The trajectory that a charged particle took while traveling in the TPC can be reconstructed using these hits. The reconstructed trajectory is called a track. Figure 3.9 shows tracks in the TPC from a beam gas interaction that was recorded in March 2010 [53].

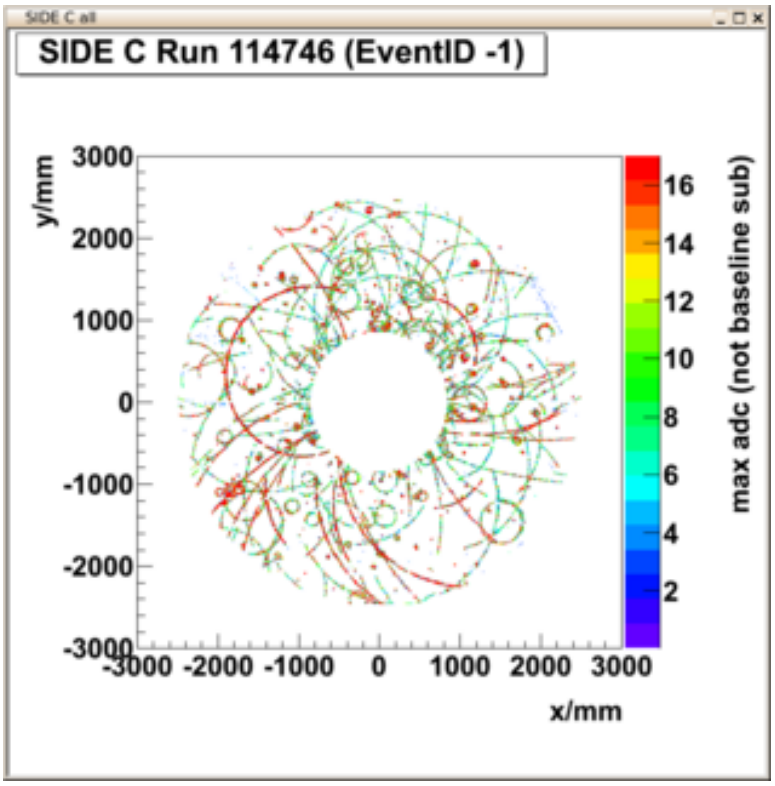


Figure 3.9: Tracks in the TPC from an event display from beam gas interactions from March 2010 [53].

The 0.5 T magnetic field, will cause the charged particles to have a spiral track. The momentum can be determined by the radius of curvature of the charged particle's

track. The direction that the track bends will tell the charge, either positive or negative, of the particle. The density of the ionization can give a dE/dx measurement which will help determine the identity of the particle.

3.5.2 TPC dE/dx

The TPC can give mean rate of energy loss measurements, dE/dx, for charged particle tracks. Relativistic charged heavy particles traveling through a gas will lose energy over a distance due to ionization of the atoms in the gas. The mean rate of energy loss depends on the particle's speed and mass described by the Bethe-Bloch equation [54].

$$-\left\langle \frac{dE}{dx} \right\rangle = Kz^2 \frac{Z}{A} \frac{1}{\beta^2} \left[\frac{1}{2} ln \frac{2m_e c^2 \beta^2 \gamma^2 T_{max}}{I^2} - \beta^2 - \frac{\delta(\beta\gamma)}{2} \right] \tag{3.1}$$

Here, T_{max} is the maximum kinetic energy which can be imparted to a free electron in a single collision, ze is the charge of the incident particle, m_e is the electron mass, c is the speed of light, $\beta = v/c$, and I is the mean excitation energy. K, Z, and A are properties of the gas absorber. In a given material, dE/dx is a function of the incident particle's velocity and mass.

Figure 3.10 shows dE/dx versus momentum of charged particles measured by the TPC. The lines are a parametrization of the detector response based on the Bethe-Bloch formula. Various particles can be seen in Figure 3.10 along these curves: pions (π), kaons (K), protons (p), deuterons (d) which are composed of a proton and a neutron, and tritons (t) which are one proton and two neutrons. Electrons (e) are along the horizontal line on this figure. Since electrons have a small mass, they lose energy differently. Relativistic electrons lose energy passing through matter mostly by bremsstrahlung. A sample of particles with momentum below 10 GeV/c can be enhanced with electrons by using dE/dx measurements in the TPC.

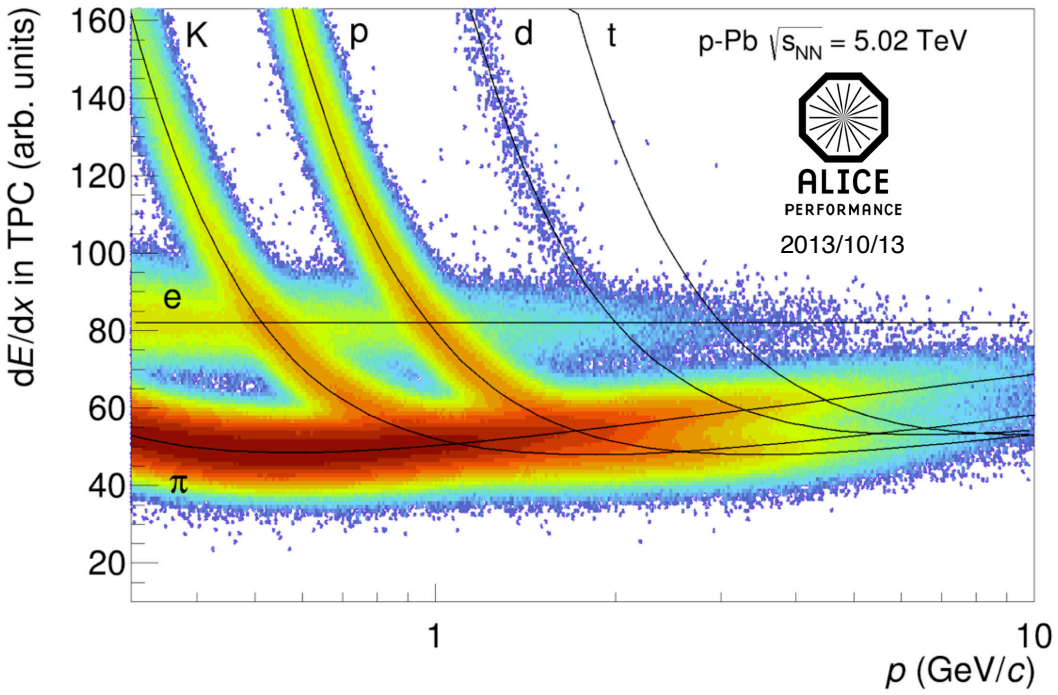


Figure 3.10: Charged particle dE/dx measurement in the TPC. Black lines are drawn based on the Bethe-Bloch predictions for various particles. ALI-PERF-60751 [55]

3.6 Electromagnetic Calorimeter: EMCal

The Electromagnetic Calorimeter [56] [57] provides the primary electron particle identification for high momentum particles and a triggering mechanism for saving events that are most likely to be populated with electrons. Our group at ORNL and UT played a major role in building and maintaining the EMCal. For these reasons the EMCal is an important component of this analysis and is described in significant detail in the following sections.

Calorimeters are used to measure the energy of incident particles. While other detectors can only measure charged particles, calorimeters can measure charged and neutral particles, including photons, neutrons, electrons and pions. Calorimeters are useful because they can distinguish electrons from pions by their interactions with the

material in the calorimeter. Electrons and photons will interact electromagnetically, through bremsstrahlung and pair production. Hadrons, such as pions, will interact hadronically, through strong and electromagnetic interactions.

3.6.1 Electron and Photon interactions with the EMCal

Charged particles incident on the EMCal will have a momentum of at least 0.5 GeV/c. ALICE's 0.5 Tesla magnetic field bends the charged particle's tracks. The EMCal sits 450 cm radially away from the beam line [57]. Consequently, charged particles with less momentum than 0.5 GeV/c will spiral too tightly to be able to reach the EMCal. At these high energies, electrons primarily lose energy through bremsstrahlung. Charged particles lose energy by bremsstrahlung when the particle is deflected by atoms in a material and emits radiation in the form of photons. At low energies, electrons lose energy by ionization and thermal excitation, by collisions with the atoms in materials.

At high energies, photons lose energy in matter through pair production, where a photon converts to an electron-positron pair, $\gamma \rightarrow e^+e^-$. At low energies, photons lose energy by Compton scattering and the photoelectric effect.

The Electromagnetic Calorimeter is very effective at detecting and measuring the energy of electrons and photons. The EMCal measures energy by absorbing the particle shower. When an electron passes through the dense material in the EMCal, it will lose energy through bremsstrahlung, and will emit radiation in the form of photons. Each of these photons will go through pair production. The number of particles will increase, but the particles will have lower energy at each step. When the energy of the particles generated fall lower than the critical energy, E_c, then the particles are less likely to lose energy by the generation of particles and the electromagnetic shower will stop. The EMCal measures the energy released in the detector material from the electromagnetic shower, which is proportional to the energy of the incident particle.

The critical energy, E_c, is the energy at which the electron's energy loss by bremsstrahlung and ionization are equal. In lead, the critical energy is about 7 MeV for solids (gases) [58],

$$E_c = \frac{610(710)\, MeV}{Z + 1.24(0.92)}. \tag{3.2}$$

The radiation length, X_0, describes the rate that electrons lose energy by bremsstrahlung [58]. The radiation length is the mean distance that an electron travels to fall to $(1/e)$ of its original energy, E_0,

$$\langle E(x) \rangle = E_0\, e^{-(x/X_0)}. \tag{3.3}$$

In one radiation length, an incident electron will give up about two-thirds of its energy. The radiation length depends on the atomic number and weight of the material, Z and A. Materials with a higher Z will have a shorter radiation length.

$$X_0\, (g/cm^2) \simeq \frac{716\, g\, cm^{-2}\ A}{Z(Z+1)\ \ln(287/\sqrt{Z})} \tag{3.4}$$

The EMCal is made from lead and scintillating material, and has an effective radiation length of 12.3 mm. The growth of the shower scales with the radiation length and the energy of the incident particle. The shower length is given by $X_s = X_0/b$, where b depends on the material Z and energy of the incident particle.

The shower spread is described by the Molière radius R_M, which is the average deflection of electrons transverse to the shower axis after one radiation length. About 90% of the shower energy is contained in a cylinder with a radius equal to the Molière radius. The effective Molière radius for the EMCal is 3.20 cm [57]. The EMCal tower's front face has dimensions of 6 $\times$ 6 cm. Most of the deposited energy is expected to be contained within one EMCal tower if an electron is incident on the center of the tower

$$R_M = \frac{X_0\, E_S}{E_c} = 21\, MeV \frac{X_0}{E_c\, MeV}. \tag{3.5}$$

The shower maximum t_{max}, measured in radiation lengths, is the depth at which most of the secondary particles are produced

$$t_{max} \simeq \ln\left(\frac{E_0}{E_c}\right) + t_0. \tag{3.6}$$

In this equation t_0 is -0.5 for electrons and +0.5 for photons. The detector thickness needed to absorb a shower only increases logarithmically with the energy of the incident particle. This makes calorimeters space effective. The electrons seen in the EMCal for pPb collisions have an energy below $\sim$ 40 GeV. The electron shower is well contained in the EMCal, which has a thickness of 20.1 radiation lengths.

Table 3.2: EMCal parameters [57]

Sampling Ratio	1.44 mm Pb / 1.76 mm Scintillator
Effective Radiation Length X_0	12.3 mm
Effective Moliere Radius R_M	3.20 cm
Number of Radiation Lengths	20.1

3.6.2 Other particle interactions with the EMCal

Hadronic showers show larger spatial fluctuations than electron showers [59] [60]. There isn't a typical hadronic shower profile, but instead it depends on energy and can vary event to event. Hadronic showers consist of two different components, electromagnetic and non-electromagnetic. The non-electromagnetic component is defined as everything that is not included in the electromagnetic component.

The hadronic interaction can produce neutral and charged pions. Neutral particles such as π^0 and η will generate an electromagnetic response. The neutral pion, π^0, has a main decay mode, with branching ratio of 0.98823, into two photons, $\pi^0 \rightarrow \gamma + \gamma$ [3]. The secondary photons from the π^0 will induce an electromagnetic shower in the EMCal.

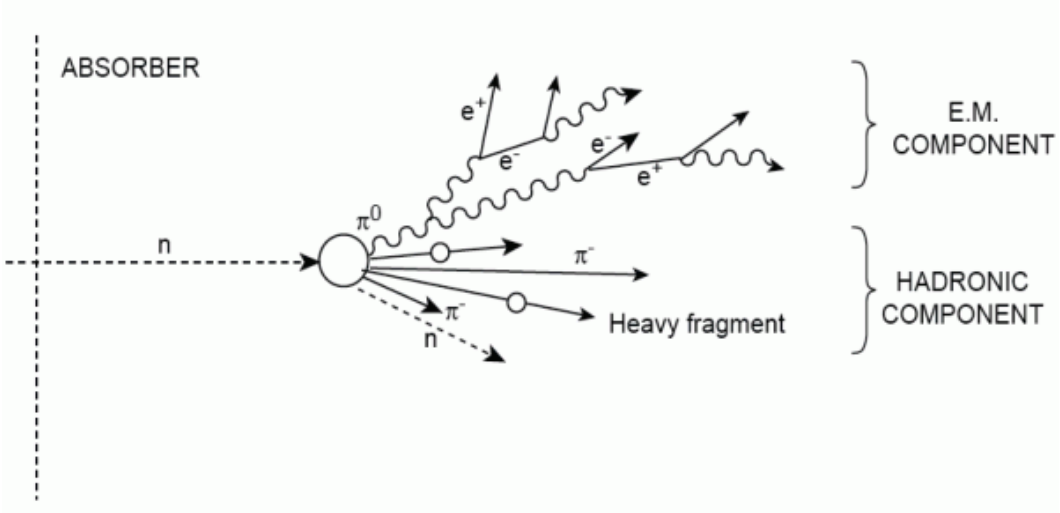


Figure 3.11: Neutron interacts with an absorber and showers with hadronic and electromagnetic components [61].

The charged pions, π^- and π^+, have a main decay mode with a branching fraction of 0.999877 into a muon and a muon neutrino, $\pi^- \rightarrow \mu^- + \bar{\upsilon_\mu}$ and $\pi^+ \rightarrow \mu^+ + \upsilon_\mu$ [3]. Charged pions will have a hadronic interaction with the detector.

Figure 3.11 shows a neutron encountering an absorber and showering with electromagnetic and hadronic components. When a π^0 is created in the absorption process it drops out of the hadronic cascade and only contributes to the EM component. The charged pion, π^-, continues to contribute to the hadronic component of the shower.

An additional complication is that calorimeters usually have different response to electromagnetic and non-electromagnetic shower components. Hadrons will generate a lower signal from the EMCal than electrons with the same incident energy. The electromagnetic shower includes bremsstrahlung and pair production. These EM processes involve small momentum transfers and do not disrupt the nucleus of the absorber material. However for hadronic processes, the nucleus can be disrupted. Some fraction of the energy of the incident particle can go into binding energy. This fraction can vary largely event to event.

Energy is also lost due to neutrinos. When a charged pion decays into a muon and neutrino, the neutrino does not interact with the detector. The energy that the neutrino carried is not measured by the detector and is lost.

Muons can also contribute to energy losses in the cascades. Some particles, for example muons, will not shower at all and will lose a minimum rate, dE/dx, of energy as they travel through the depth of the EMCal. These particles are said to be Minimum Ionizing Particles, or MIP. The minimum ionizing particles do not deposit all of their energy into the EMCal. For particles such as electrons the EMCal is a destructive detector. However for MIPs, they can be further measured after passing through the EMCal. MIPs will enter the detector, deposit some energy in the detector, and continue through. If muons are created in the hadronic cascade, then a fraction of their energy will not be measured.

In EM showers, a detector with a certain amount of depth is needed to contain the full length of the shower and collect the most amount of incident energy. The hadronic showers also need a detector with a certain depth in order to be measured.

As the unit of length of electromagnetic showers is the radiation length, X_0, the hadronic showers length is described by the nuclear absorption length, λ_0. The nuclear absorption length is usually larger than the radiation length. For the same absorber material, a thicker detector is needed to measure hadronic showers than is needed to measure electromagnetic showers. The ratio λ_0/X_0 scales as Z, the atomic number of the absorber material [60].

$$\lambda_0 \sim [35(g/cm^2)][A^{1/3}] \tag{3.7}$$

Hadronic showers begin at a larger depth and are more diffuse than electromagnetic showers. For example, in lead the radiation length for electromagnetic shower is 6.3 g/cm^2 while the hadronic shower's nuclear interaction length is 193 g/cm^2. The EMCal was not designed to be thick enough to fully contain the hadronic shower. Some hadrons will go through the EMCal without showering and will behave as

MIPs. In these cases, the energy deposited and measured in the EMCal will be less than the hadron's original energy.

3.6.3 Design of the EMCal

EMCal is a Pb-scintillator sampling calorimeter [57]. Sampling calorimeters are made of alternating layers of material. One material degrades the energy of the incident particle and produces the particle shower, the lead material in the EMCal. The other material provides a detectable signal by absorbing the energy and re-emitting it in the form of light, the scintillating material in the EMCal. The light produced in the scintillating material provides a measurement of the original particle energy.

The sandwich of Pb and scintillating material makes up an EMCal module. The photons converted from the scintillating layers are carried along the wavelength shifting fibers that run down the modules. The photons are then converted into an electric signal that can be measured. When an electron hits the EMCal then this signal will be proportional to the energy deposited by the electron in the calorimeter.

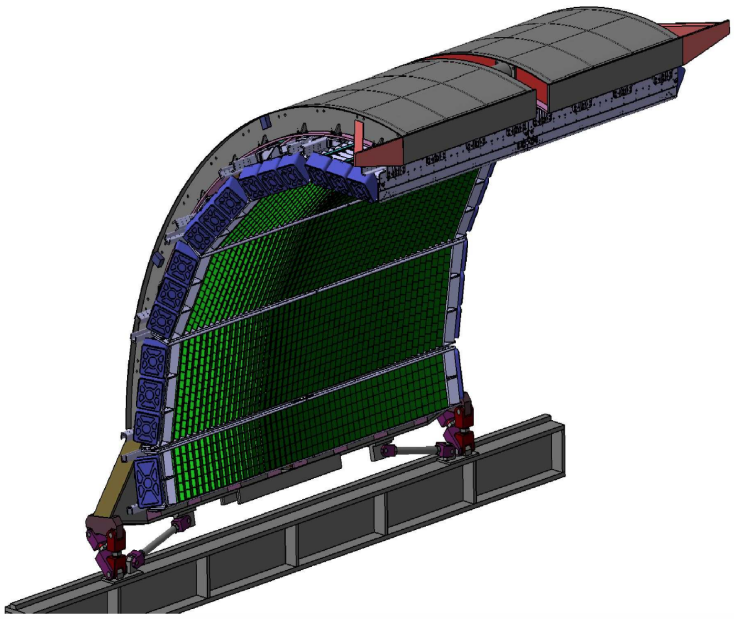


Figure 3.12: The ALICE EMCal super modules and support structure [57].

Calorimeters are destructive detectors, making any further measurements of the particles unreliable. For this reason, the ALICE EMCal was installed outside of the ITS and TPC. It sits inside of the solenoid magnet. The front face of the EMCal sits 450 cm radially away from the collision point. The EMCal spans -0.7 $< \eta <$ 0.7 in pseudorapidity and 110° in azimuth. The EMCal weighs roughly 90 tons and the support structure for the EMCal, the CalFrame, weighs 25 tons. Figure 3.12 shows the ALICE EMCal mounted in its support structure.

The smallest building block of the EMCal is a module which is a self supporting and self contained detector unit [57]. Each module is made up of $2 \times 2 = 4$ towers, also referred to as cells. Each tower is an independent detection channel. The modules are built from stacking 76 and 77 alternating layers of Pb and scintillator. The module is closed around the sides by a thin layer of stainless steel. The module has an aluminum front, back, and compression plate. 36 wavelength shifting fibers are inserted longitudinally through the tower. The fibers connect through the light guide to the Avalanche PhotoDiode photosensor and a preamplifier. Figure 3.14 shows the cross section of a module and two towers. Figure 3.13 shows the rear of a prototype EMCal module with green fibers, black plastic tube light guide and APD and preamplifier.

A tower has active dimensions of 6.0 $\times$ 6.0 $\times$ 24.6 cm^3. The acceptance of the front face of the tower at $\eta = 0$ is $\Delta\eta \times \Delta\phi \sim 0.014 \times 0.014$. The ALICE EMCal is comprised of 12,288 towers [57].

In order to stabilize and install the modules into their final position inside of the ALICE magnet, the modules were assembled into strip modules and then into super modules [57]. The strip modules are 12 $\times$ 1 modules held in a structural strong-back. The super module is assembled by stacking and securing 24 strip modules into a crate. The strip modules are installed to be projective in the η direction. The super module is made from a total of 288 modules or 1152 towers. Like the module, the strip and super modules are also self-supported detector units. ALICE has a total of 10 super modules and 2 one-third size super modules, as shown in Figure 3.12. The one-third



Figure 3.13: Module prototype with fibers, APD and preamplifier [57].

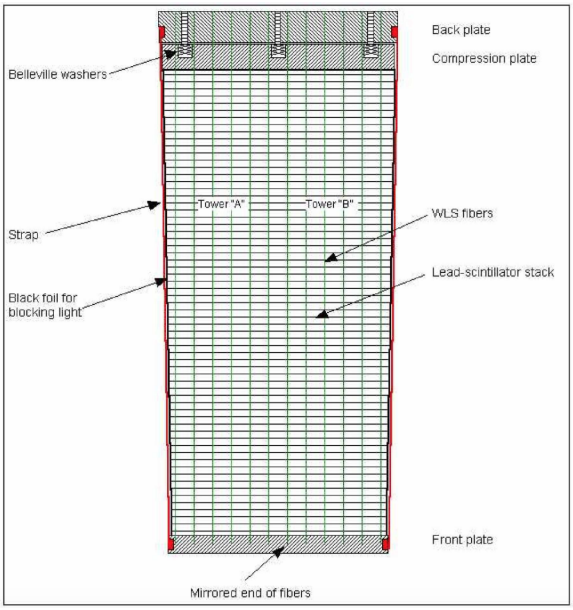


Figure 3.14: Cross section of one module [57].

size super module was assembled from $4\times\ 24 = 96$ modules (384 towers). The super modules were mounted and installed as a unit on the support structure and inside of the ALICE magnet.

3.6.4 EMCal Electronics

Energy deposited into the EMCal are converted into visible photons in the lead and scintillating layers of the EMCal modules. The photons are guided along by the optical fibers that run along vertically through the modules. The optical fibers from a tower connect to an Avalanche PhotoDiode photosensor and a Charge Sensitive Preamplifier. The APD converts the visible photons into an electric signal.

The raw signal, called ADC counts, is in the form of a semi-Gaussian pulse shape. The ADC signal as a function of time can be described as equation 3.8, [57]

$$ADC(t) = Pedestal + A \cdot x^{\gamma} \cdot exp^{\gamma(1-x)},\ \ where\ x\ = (t - t_{max} + \tau)/\tau \qquad (3.8)$$

where *Pedestal* is the threshold for background energy of the towers. The function peaks at time value of t_{max}. The decay constant is τ. The power parameter of the fit is γ. The energy deposited in the tower is proportional to the parameter A.

The raw signal from the Charge Sensitive Preamplifier has high gain and low gain signals which are sampled separately. The signal is split into energy and trigger shaper channels by the Front End Electronics, FEE, boards. One FEE board reads the signal in 32 EMCal towers [57]. Each FEE board requires four ALTRO chips. These chips were originally designed for the TPC and ALTRO is an abbreviation for ALICE Time Projection Chamber ReadOut chips. Each ALTRO chip has 16 10-bit flash ADC buffers, so four ALTRO chips are required to read 32 EMCal towers with 32 high and 32 low gain channels. The raw signal is a 10-bit ADC word and the ALTRO chip converts the data into 40-bit words.

Each FEE card sums 2×2 tower signals to provide Level-0 and Level-1 triggers. This signal is passed to the Trigger Region Unit that can make a decision to generate a trigger. See section 3.6.7 for more detailed information about EMCal triggers.

The FEE boards are connected to the Gunning Transceiver Logic (GTL) bus and then the Readout Control Unit (RCU) [62]. The GTL bus transmits data and commands from the RCU to the FEE boards. A single GTL bus is connected to 9 FEE cards and subsequently 384 EMCal towers. An RCU card can drive two independent GTL buses. The RCU relays commands from the ALICE DAQ (Data Acquisition) system. The DAQ control system makes programmed decisions, but the operator can issue commands through user interfaces.

Reading a single channel on the GTL bus takes 0.5 μs. By only reading the ALTRO channels with hits, the readout time of the EMCal has a minimum time of 270 μs [62].

3.6.5 EMCal Calibration

The towers in the EMCal each have some slight variation and will generate a slightly different response to the same energy deposit unless they are relatively calibrated. A method for calibrating a calorimeter is to study the interaction of particles with known energy with the detector. Some particles, like muons, pass through the EMCal without creating a shower, instead they lose energy at the minimum rate while interacting with the matter in the detector. These are known as minimum ionizing particles, or MIPs.

Cosmic muons are useful for calibrating the detector because they are a permanent and free source of particles with known energy. These are muons created in the upper atmosphere by cosmic rays. Cosmic muons can test the full span of the detector and behave as a MIP.

Cosmic muons calibration was performed on the full EMCal before it was inserted in the ALICE experiment [63]. Figure 3.15 shows the experimental setup of the cosmic muon calibration. Scintillator paddles were placed above and below the strip modules, which are 12 modules (and 48 towers) in a strong back. When a cosmic muon with MIP behavior passes through the strip modules, then a signal will be present in the pair of scintillator paddles above and below the strip modules. When this signal is seen, a trigger is prompted and the data from the 1/3 super module section is read. Data were taken for 24 hours.

To get a clear signal, muons that crossed multiple towers were eliminated. This was done by choosing events that had signal in only one tower with no signal or low signal seen in the neighboring towers. A calibration factor was given to every tower based on the response to the minimum ionizing cosmic muons signal. All towers in the EMCal were normalized using the MIP signal.

Another calibration was done to track the EMCal's response over time and due to temperature fluctuations [57]. Each full EMCal Super Module has 37 FEE boards. Of the 37 FEE boards, 36 FEE cards read data from 1152 towers and one FEE board is

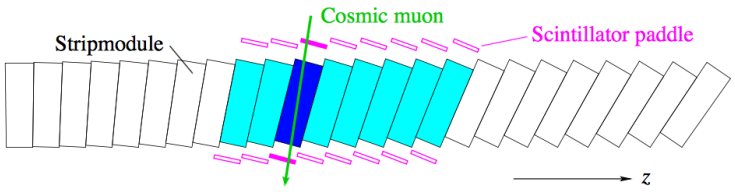


Figure 3.15: Schematic of the experimental setup for the cosmic muon calibration [63].

used for an LED calibration channel [62]. In an LED event, all towers view a calibrated pulsed LED light source. The LED event, temperature, and time is recorded. The LED events are separated from the physics events and used for calibration purposes. The LED calibration addresses the EMCal ADC count's dependence on temperature and operation time.

3.6.6 Cluster Algorithms

When an electron hits the EMCal, it will deposit some energy across several towers. The energy needs to be summed together to a single cluster. The basic algorithms will be described here, the Version 1, Version 2 and the N×N clusterizer [64] [65].

The Version 1, V1, clusterizer sorts the towers by the signal from highest to lowest. The towers with the highest signal are the seed towers. The clusterizer will then look at the 4 adjacent towers. If the neighboring towers have a signal greater than a minimum then the energy will be added to the cluster. This will continue until there is no more neighbors with signal. This algorithm is useful because it can accept clusters with any size. Some hadrons will leave a huge shower in the EMCal across many towers and the V1 clusterizer can accommodate it. Figure 3.16 shows different cluster algorithms. The upper left picture shows the EMCal with a signal in 17 towers. The V1 clusterizer accepts the entire signal as a single cluster. The V1 algorithm does a good job finding the correct clusters if the density of signal in the EMCal is low, like in pp collisions. However if the EMCal has a high hit density, as seen in PbPb collisions, then the V1 clusterizer can merge energy deposits

from multiple particles into a single cluster. In figure 3.16 in the upper right hand picture, two particles have deposited energy in the EMCal next to each other. The V1 algorithm has merged them into a single cluster. The V1 algorithm does not have a maximum cluster size and could merge the entire area of the EMCal into a single cluster.

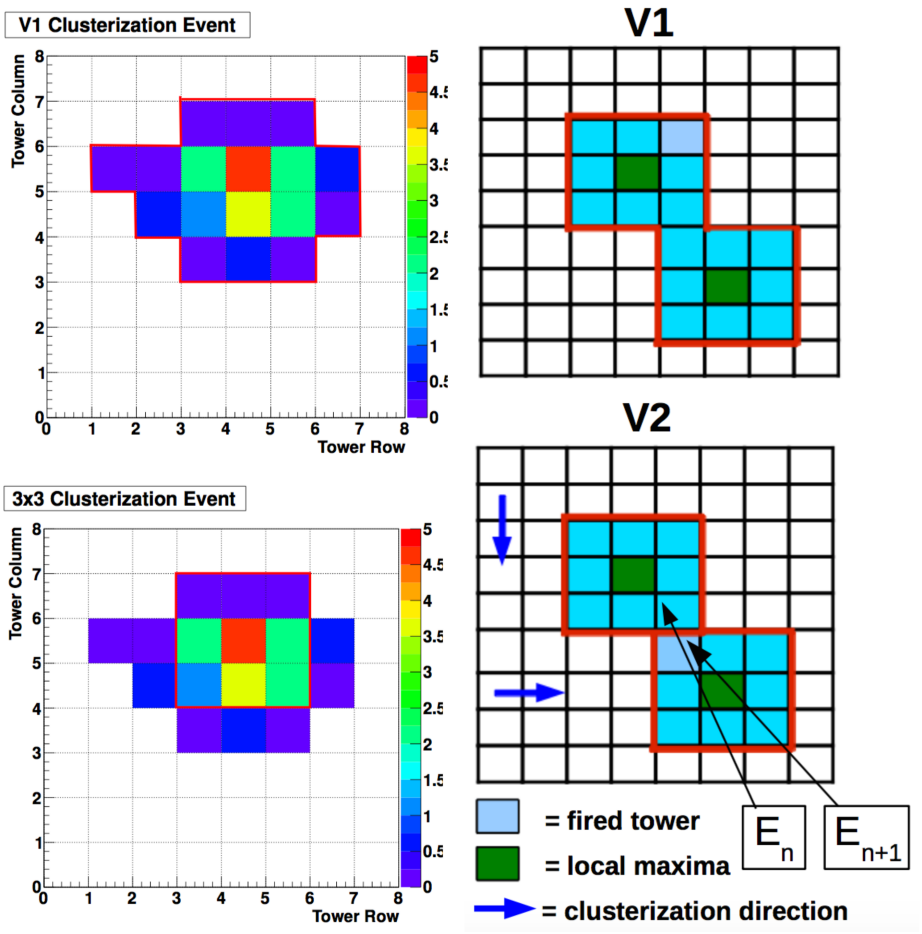


Figure 3.16: EMCal clusterizers Version 1, Version 2 and 3×3 [64] [65].

The Version 2, V2, clusterizer works similar to the V1 clusterizer. However V2 limits the size of the cluster by requiring that a cluster can only contain one energy maximum. The V2 clusterizer starts with a seed tower and then adds neighboring tower energies. V2 stops adding when it encounters a neighboring tower that has an energy larger than the energy of a tower already in the cluster. This way, the

V2 clusterizer stops when it finds another local maximum and the energy gradient is reversed. In the lower right image in figure 3.16 shows the V2 clusterizer. The V2 clusterizer separates the two local maximums into their own clusters where the V1 clusterizer merged them.

The N×N clusterizer also starts with a seed tower with the highest energy. However, the N×N clusterizer has geometrical limits to the cluster that can be found. It will only add a square area of N×N towers together to form a cluster. The 3 × 3 clusterizer will only make a cluster with 9 adjacent towers, with the seed tower being in the center. The lower left image in figure 3.16 shows the 3 × 3 clusterizer. The cluster formed has some remnant energy that was not added into the cluster. This creates two effects. First, the 3 × 3 clusterizer can underestimate the energy deposited by some particles with large showers. Second, the remnant energy gets picked up as new 3 × 3 clusters with small energy, creating a lot of lower energy clusters. However the 3 × 3 clusterizer has the benefit that it is conceptually easy to understand and it will not merge separate signals together.

The raw signal from the EMCal is converted to clusters and saved into ALICE data. The default clusterizer used for this reconstruction is the V1 clusterizer. However, there is no single clusterizer than the entire EMCal group uses. A specific analysis can choose the best cluster algorithm for their analysis by running a task that reclusterizes. The EMCal 'tender' is such a task that runs before the user task and can use any of these clustering algorithms. The tender also cleans up the data for EMCal analysis by removing bad channels. The EMCal tender default clusterizer is V2.

The size of electron clusters is usually less than 10 cells. A 3 × 3 clusterizer would be an adequate size to find electron clusters. The pPb data have low EMCal hit density, with only about 8 clusters in the EMCal per event on average. The V1 clusterizer would work fine in this low hit density environment. Since this analysis is on electrons and on pPb data, it is not sensitive to the clusterizer chosen. The clusterizer used for analysis is the EMCal tender default V2 clusterizer.

3.6.7 EMCal Trigger

The rate of collisions at the LHC is higher than the rate that the ALICE detector can read and record data. The EMCal trigger provides a way to record events with a high potential for interesting physics. The EMCal trigger is issued for events with EMCal activity.

The EMCal has a Level 0 trigger, Level 1-gamma trigger and Level 1-jet trigger [66] [56]. The triggers of interest for this analysis are the Level 0 and Level 1-gamma triggers. The Level 0 and Level 1-gamma triggers are designed specifically to record events with photons and electrons. The EMCal trigger works by dividing the EMCal into predetermined areas called a patch. If the summed signal in a patch is higher than a certain threshold, then the trigger is fired. Table 3.3 shows the EMCal trigger names and thresholds for the 2013 pPb data in ALICE.

Table 3.3: EMCal triggers for pPb events

Trigger Name	Level	Threshold
EMC7	Level 0	3 GeV
EG1	Level 1-gamma	11 GeV
EG2	Level 1-gamma	7 GeV

Figure 3.17 shows a flat view of the entire EMCal with the 10 full size Super Modules and two 1/3 size Super Modules along with the trigger electronics. Each Super Module is divided into three regions. Each region is read out by 12 Front End Electronic (FEE) cards, which computes the local L0 trigger. The signal goes to The Trigger Region Unit, TRU, which then computes the global L0 trigger. The Summary Trigger Unit, STU, then uses the TRU data and computes the L1 trigger.

For the Level 0 and Level 1-gamma trigger, the EMCal is divided into trigger patches of predetermined areas of 4×4 adjacent towers, or 2×2 adjacent modules[66]. The patches overlap by 2 towers, 1 module. Since the L0 trigger is determined from the TRU's, the patches that can fire an L0 trigger are limited to

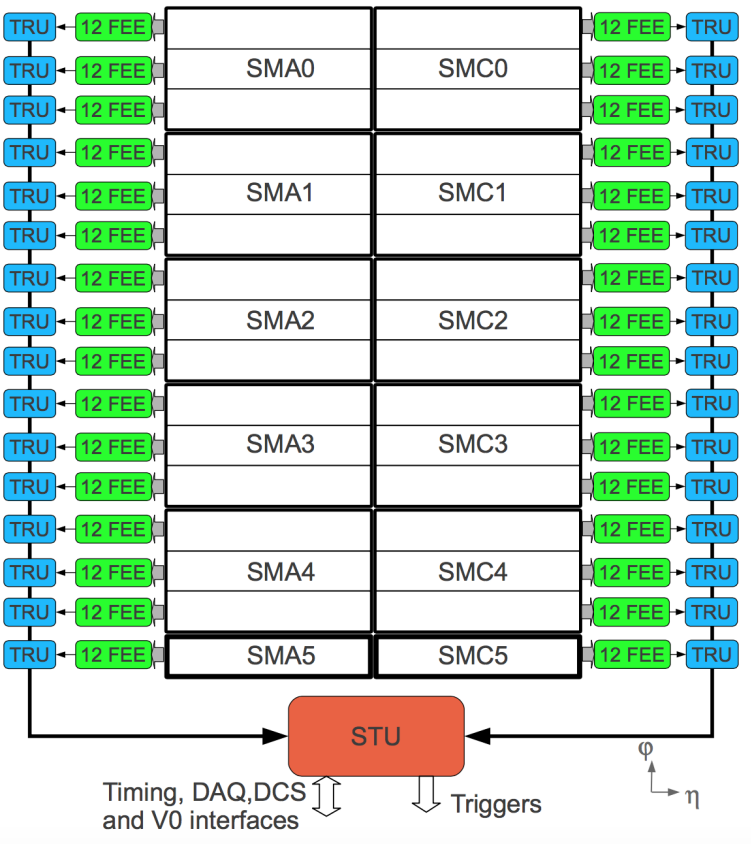


Figure 3.17: EMCal Super Modules with the trigger electronics, Front End Electronics, Trigger Region Unit, and Summary Trigger Unit [66].

the region that a single TRU is connected which is 1/3 of a Super Module. The L1 trigger is computed later, at the STU level, and can cross these boundaries.

Figure 3.18 shows a drawing of a 1 and 1/3 of a Super Modules of the EMCal. Each cell in this figure is one module (2×2 towers). The two yellow squares show that energy has been deposited into these modules. If the energy deposit is high enough, then it can fire a trigger. The red and green square show the L0 and L1-gamma trigger patch size of 2 × 2 modules and possible trigger patch locations. The L0 trigger patches are limited to boundaries of 1/3 of a Super Modules which are shown by the thick black lines. The L1 trigger patch can cross these regions and is shown sitting on a boundary. Due to these spatial inefficiencies, there are fewer L0 trigger patches than L1. There are a total of 2208 L0 trigger patches and 2961 L1-gamma

trigger patches. However, the L0 trigger is processed faster than the L1 trigger. The L0 trigger is decided 1.2 μs after the event while the L1 trigger is decided 6.5 μs after the event [66].

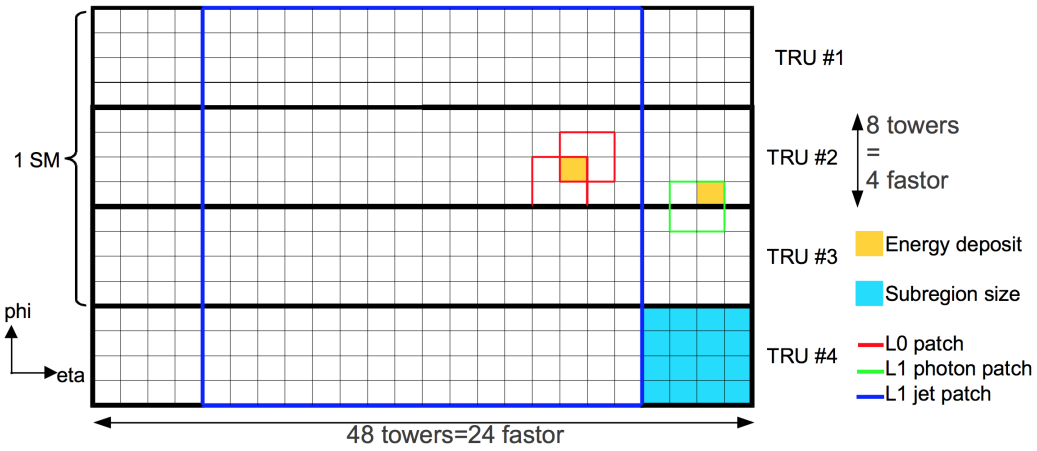


Figure 3.18: A cartoon of 1 and 1/3 Super Module. Each cell is one module. Possible L0, L1-gamma (labeled as L1 photon patch) and L1-jet trigger patches are shown [66].

3.7 Data Objects

The raw data from the collisions are converted into calibrated objects and put into ESD files, Event Summary Data, and AOD files, Analysis Object Data. AOD files contain less information than ESD files. For example, the ESD contains several values for momentum. The ESD contains information for the momentum near the collision vertex as a result of the ITS and TPC tracking, the TPC only momentum, and the momentum at the front face of the TPC. When running over AOD files, only two choices are available: tracks with momentum measured by the ITS+TPC, or tracks with momentum measured from the TPC. Since the AOD files are more condensed, they require much less CPU cost and running time in order to analyze them. This analysis used AOD files since the information in the AOD files was sufficient.

The event, track, and EMCal objects can be accessed in the ESD and AOD files. Event object information available from the data files includes the primary vertex position, centrality, trigger class, and run number. The ITS and TPC track information includes the η and ϕ position of the track, the TPC dE/dx, momentum of the track, the charge of the particle that made the track, and the number of space points that made the track. Some EMCal cluster objects available are the η and ϕ position of the cluster, the energy deposited, the shower shape parameters (see 4.6.3), and the number of cells in the EMCal shower.

Chapter 4

Analysis

4.1 pPb Collisions in ALICE

The Large Hadron Collider collided protons with lead ions in January and February of 2013. To collide proton and lead ions, the LHC circulated bunches of protons with energy of 4 TeV and fully stripped lead ions at 82×4 TeV [67]. The bunches crossed at the interaction points along the LHC. The pPb collisions had center of mass per nucleon energy of 5.02 TeV. One of the interaction points was in the center of the ALICE detector.

Charged particles coming away from the collision can create tracks in the TPC. The TPC covers the range $0 < \phi < 2\pi$, but the EMCal covers a smaller range, of $1.4 < \phi < 3.3$ or $80^\circ < \phi < 187^\circ$ [44]. ALICE has a 0.5 Tesla magnetic field that makes the charged particles spiral as they travel. The momentum of the particles can be measured using the curvature of the bend of the tracks. However, if the momentum of the particles is low, then the particles will spiral too tightly to make it out to the EMCal. To be able to hit and deposit energy into the EMCal, charged particles must have a momentum of at least around 0.5 GeV/c and be heading towards the region of the EMCal, $1.4 < \phi < 3.3$ and $-0.7 < \eta < 0.7$. The signal from the energy deposited in the cells of the EMCal is later reconstructed into EMCal clusters. The

total energy and position of the EMCal clusters are calculated and saved as objects that can be accessed in the data files. See section 3.7 for a discussion of objects available in ALICE data files.

For minimum bias p-Pb collisions in ALICE, there are about 24 total number of tracks in the TPC per event on average. The number of tracks that are in the region of the EMCal are about 3 per event. There are about 8 clusters in the EMCal per event. Of these EMCal clusters about 1.5 are matched to tracks. Only a few of these matched clusters pass the particle identification criteria for being an electron candidate. The number of electron candidates found using the TPC tracks and the EMCal is 0.003 per event on average.

The track multiplicity varies considerably for different event classes. For the highest multiplicity events, centrality of 0-20%, the number of tracks per event is about 47 on average. For the lowest multiplicity, centrality 80-100%, the number of tracks per event is about 6 on average. The tracks in the region of the EMCal are about 6 and 0.6 for high and low multiplicity events respectively. The number of electron candidates is 0.006 and 0.0006 per event for high and low multiplicity events.

4.2 Run selection

A single run is minutes or hours of data taking, thousands to millions of events. Run periods are days or weeks of these runs. The labels for run periods and run numbers are specific to each experiment.

The run periods for pPb collisions used in this analysis were LHC13b, LHC13c, LHC13d, LHC13e, and LHC13f. See Table 4.1 for a summary of run periods used for this analysis. All run periods have Minimum Bias data, but only LHC13d, LHC13e, and LHC13f have EMCal triggered data as well. (See section 4.5 for more information about Minimum Bias events and EMCal triggered events.) In LHC13f, the directions of the circulating proton and lead ions were switched.

Table 4.1: Runs used for this Analysis. Information obtained from the MonALISA Repository[68].

Configuration	Run Period	Total number of physics events	EMCal triggered data	Date of data taken in 2013
p - Pb	LHC13b	36 million	no	Jan 20-22
p - Pb	LHC13c	102 million	no	Jan 22-25
p - Pb	LHC13d	26 million	yes	Jan 25-27
p - Pb	LHC13e	38 million	yes	Jan 28 - Feb 1
Pb - p	LHC13f	111 million	yes	Feb 2 - Feb 10

Runs from these run periods that had the EMCal on and running normally and had good global quality were selected. Runs were determined to be good (Quality Assurance) by creating histograms and checking if the particle identification measurements, energy distribution in the EMCal, and other distributions are as expected. No detector is perfect. A run can be labeled as good even if some parts of the detector have dead or noisy areas.

4.3 Event and Track Selection

Events that could not be well measured were rejected. To be considered good, an event must have a well-defined primary vertex position. In order to find the primary vertex, tracks in the ITS and TPC are propagated inward to the center of the detector. Events were required to have a minimum of two contributors that were used to reconstruct the primary vertex, from either the Silicon Pixel Detector, VZERO-A or VZERO-C detector. The number of contributors, before any event cuts, for pPb collisions in ALICE is shown in figure 4.1. In this plot, there are very few events with only a single contributor to the primary vertex. This cut removes beam-gas events or events that were not well measured by ALICE.

The event was also required to be near the center of the detector, where the detector has the best performance. The primary vertex was required to be within ± 10 centimeters of the center of the detector along the beam direction, in the z-direction.

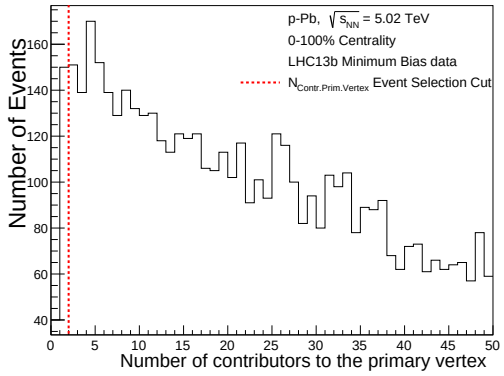


Figure 4.1: Number of contributors that were used to reconstruct the primary vertex for collisions in ALICE.

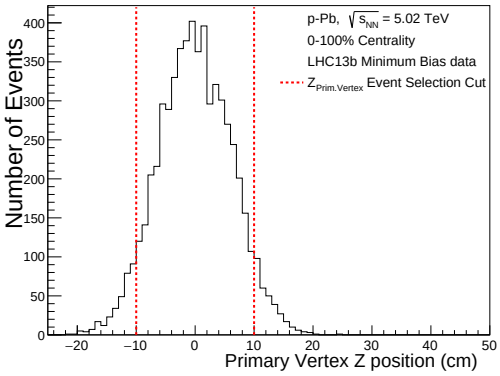


Figure 4.2: Position along the beam line of the primary vertex for collisions inside of ALICE.

This cut should not bias the data sample because the physics of the collision should be independent on the location of the collision. The z-vertex position, before event cuts, for collisions in ALICE are shown in figure 4.2. Most physics collisions do occur within ± 10 centimeters of the center of the detector, and almost no collisions occur outside of ± 20 cm.

Tracks in the ITS and TPC were required to be well measured. The number of pad rows hit as particle crossed while traveling through the ITS is shown in figure 4.3. The ITS is a small detector, only 6 layers, making the maximum number of possible hits very small. Tracks were required to have at least one hit in the inner layer of the ITS, one of the Silicon Pixel Detector layers. The TPC is a larger detector with many readout pads. A track can leave many hits in the TPC as shown in figure 4.4. The minimum number of hits allowed in this analysis for a track in the TPC was 50.

Hits in the ITS and TPC are reconstructed into tracks, starting from the outermost points on the TPC and tracking inwards to the ITS and back to the primary vertex. Then the track reconstruction is restarted from the primary vertex outwards to the ITS and TPC and extrapolated to the outer detectors. Then the tracks are "refit" back to the primary vertex. To assure tracks with good momentum resolution and vertex parameters, tracks were required to pass the final refit in the ITS and TPC.

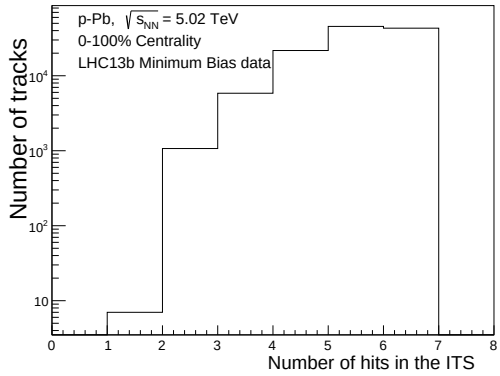


Figure 4.3: Number of pad rows hits for ITS tracks.

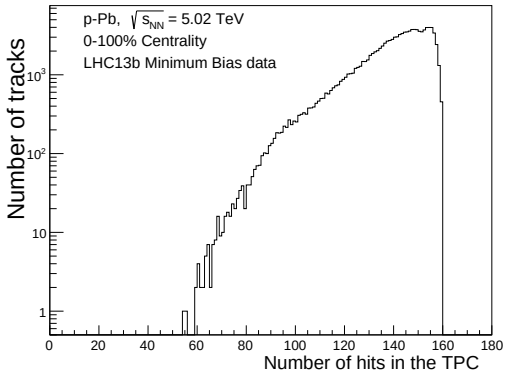


Figure 4.4: Number of hits for the TPC.

The raw signal of hits in the TPC are traced and reconstructed as tracks. The tracks in the TPC need to be a good fit in order to be considered a good track. The χ^2, or "chi-square", tests the quality of the fit of the track on the TPC hits. The TPC χ^2/NDF, chi-square per degree of freedom, is shown in figure 4.5. Tracks were required to have a TPC χ^2/NDF less than 4. Tracks were also required to have χ^2 per hit in the ITS less than 36.

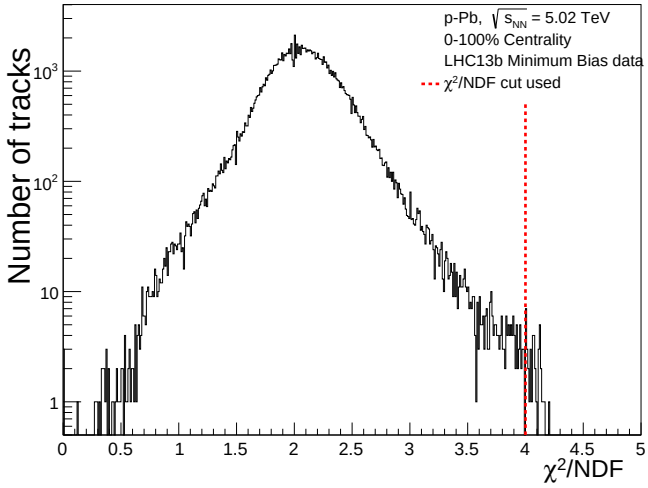


Figure 4.5: Quality of the the fit of the TPC track, χ^2 per degree of freedom, is shown for pPb collisions in ALICE.

To narrow down the large data set and to identify electrons produced from heavy flavor decays, several cuts were applied on the tracks. Heavy flavor mesons have a

decay length of a couple hundred micrometers, so they will appear to originate very close to the primary vertex. The DCA, distance of closest approach of the track to the primary vertex, will be very small for electrons from heavy flavor decays. To enhance the sample of heavy flavor electrons, a loose DCA cut was used on the tracks. The maximum distance from the track to the primary vertex in the transverse plane (DCA_{XY}) was 2.4 cm. The maximum longitudinal distance (DCA_{Z}) allowed was 3.2 cm.

Some tracks can have a 'kink'. If a particle decays while traveling through the detector, the reconstructed track can have a decay vertex, with mother and daughter tracks. Since heavy flavor mesons will decay before reaching the detector, electrons from heavy flavor decays are not expected from tracks with a kink. Any tracks with a kink were rejected in this analysis.

4.4 EMCal Cluster and Track Matching

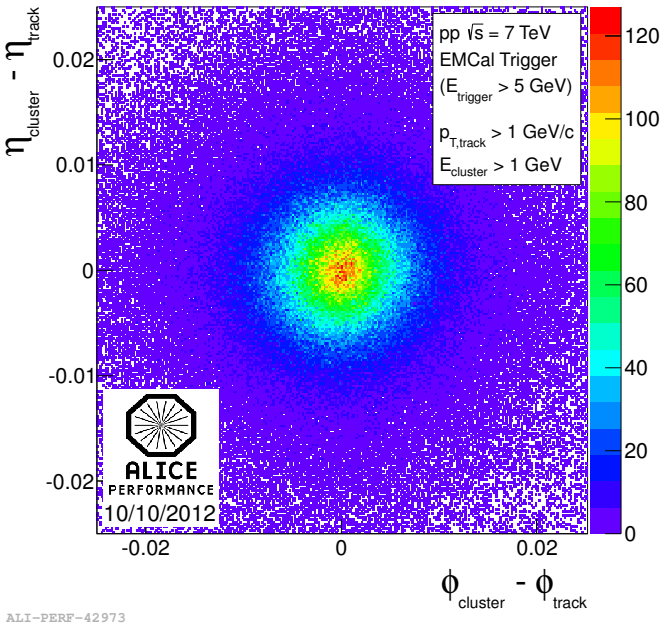


Figure 4.6: EMCal cluster and track matching [69] for pp collisions at $\sqrt{s} = 7$ TeV measured in ALICE.

Charged particles traveling from the collision out through the detector can make a track in the TPC and a cluster in the EMCal. These tracks need to be matched to the clusters in the EMCal. This is accomplished by extrapolating the position of the TPC track and the EMCal cluster position to the surface of the EMCal. Then the difference in position, $\delta\eta$ and $\delta\phi$, of the track and clusters at the surface of the EMCal are calculated. Figure 4.6 shows the distribution of residuals for all tracks and clusters with $p_{T,track} > 1$ GeV/c and $E_{cluster} > 1$ GeV in p-p collisons at $\sqrt{s} = 7$ TeV. The color on figure 4.6 represents the density of counts.

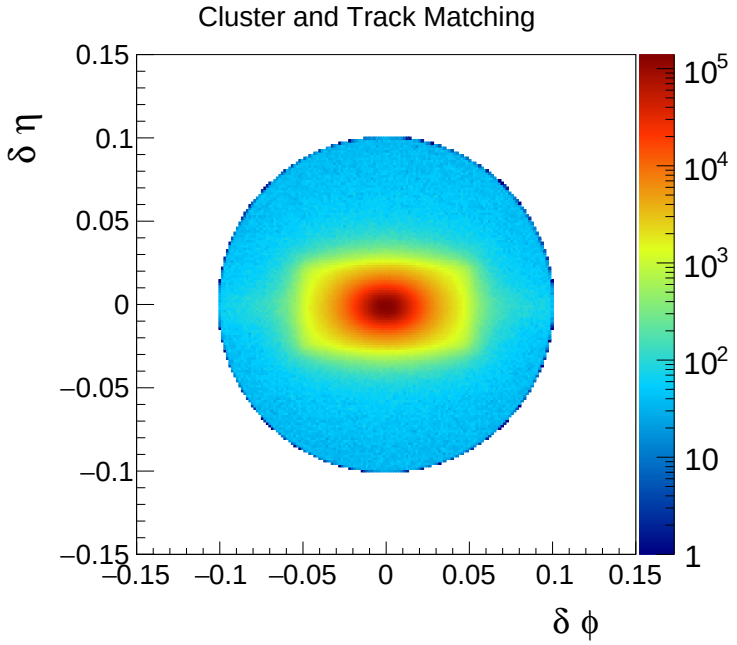


Figure 4.7: The difference in position, $\delta\eta$ and $\delta\phi$, of the track and clusters at the surface of the EMCal. The cut $\sqrt{\delta\eta^2 + \delta\phi^2} < 0.1$ has been applied. pPb collisions at $\sqrt{s_{NN}} = 5.02$ TeV measured in ALICE.

Tracks and clusters that are really from the same particle will have a small $\delta\eta$ and $\delta\phi$. The radius, or the distance between the track and the cluster, can be defined as $\sqrt{\delta\eta^2 + \delta\phi^2}$. The cluster and track are found to be matched if $\sqrt{\delta\eta^2 + \delta\phi^2}$ is less than 0.1. Figure 4.7 shows the track and cluster $\delta\eta$ and $\delta\phi$ for tracks and clusters that are labeled as matched. In this plot, a cut is applied removing any track and cluster matches with a radius, $\sqrt{\delta\eta^2 + \delta\phi^2} > 0.1$. The color on the figure 4.7 represents the

density of counts with red being the most counts. The color on the figure shows that most matched tracks and clusters have a radius near 0.014 (the size of an EMCal cell). Clusters with a radius further away from tracks are less likely to be matched.

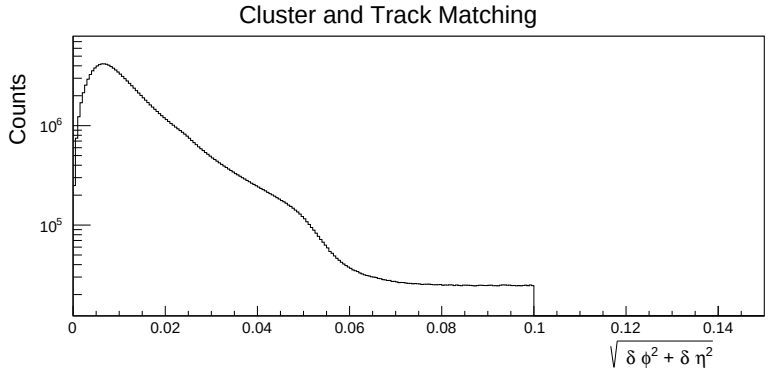


Figure 4.8: EMCal cluster and track matching. The cut $\sqrt{\delta\eta^2 + \delta\phi^2} < 0.1$ has been applied. pPb collisions at $\sqrt{s_{NN}} = 5.02$ TeV measured in ALICE.

Figure 4.8 shows the radius, $\sqrt{\delta\eta^2 + \delta\phi^2}$, of matched tracks and clusters. Figure 4.8 is consistent with figure 4.7, showing that there is a maximum of counts with a radius about the size of an EMCal cell. The number of matches decreases with an increasing radius.

4.5 Trigger Scaling

The ALICE detector cannot record every event that occurs. The rate of collisions is faster than the rate that the detector can collect data and save the events. ALICE must decide which events to record and save. The Minimum Bias trigger is activated when the detector determines that an event has occurred, and the detector is not busy writing a past event. The minimum bias trigger requires a signal in the VZERO-A and VZERO-C detector [70].

The EMCal detector implements the EMC7, EG1 and EG2 triggers. The EMCal is divided into areas of 2 × 2 adjacent towers. When the EMCal records an energy in these towers that is higher than a threshold, then the EMCal trigger is activated. The EMC7, EG1 and EG2 triggers send a signal to record an event if the EMCal has

a hit in the 2 × 2 EMCal towers that has a total energy higher than about 3, 11, and 7 GeV respectively. See section 3.6.7 for a more detailed review of the EMCal triggers.

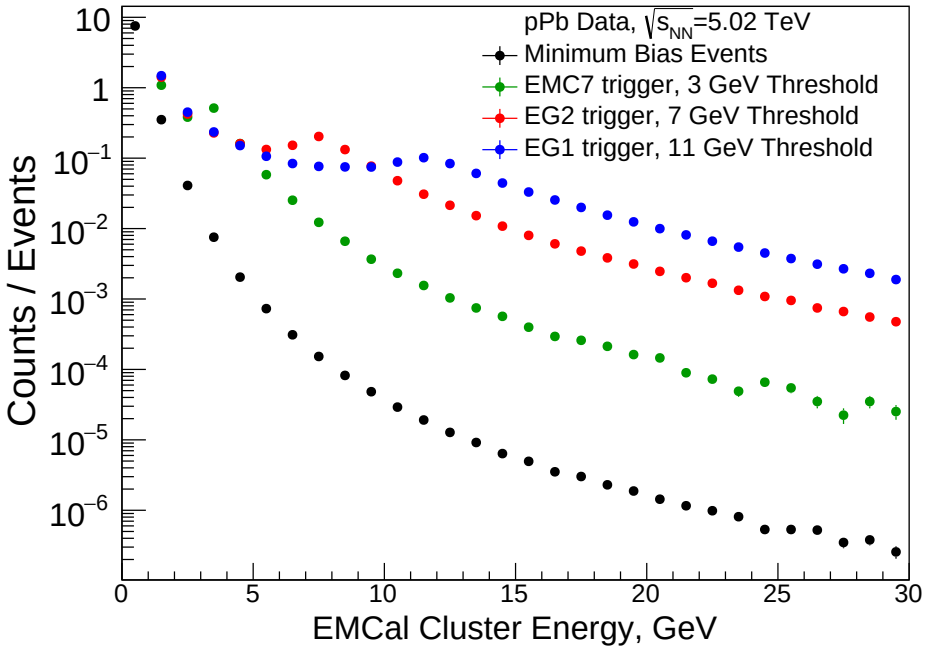


Figure 4.9: EMCal cluster energy per event for EMC7, EG1 and EG2 triggered events for pPb collisions at $\sqrt{s_{NN}} = 5.02$ TeV measured in ALICE.

Figure 4.9 shows the EMCal Cluster Energy spectrum for various triggers. The x-axis is the energy for every cluster in the EMCal. The y-axis is the number of clusters per event from energy deposited by photons, electrons, and hadrons that hit the detector. Most of the hits in the EMCal have a low energy. The Minimum Bias trigger, the black points, peaks near zero and falls with increasing energy. The EMC7 triggered events, green points, peaks around the EMC7 trigger threshold of 3 GeV and then follows the shape of the Minimum Bias triggered events. The EG1 and EG2 trigger peak at their trigger thresholds of 11 and 7 GeV. The EMC7 triggered events is a biased sample that has more 3 GeV cluster energies per event than a sample of random events. In order to compare to the minimum bias data and eventually

calculate cross sections, the amount of enhancement of triggered events needs to be determined.

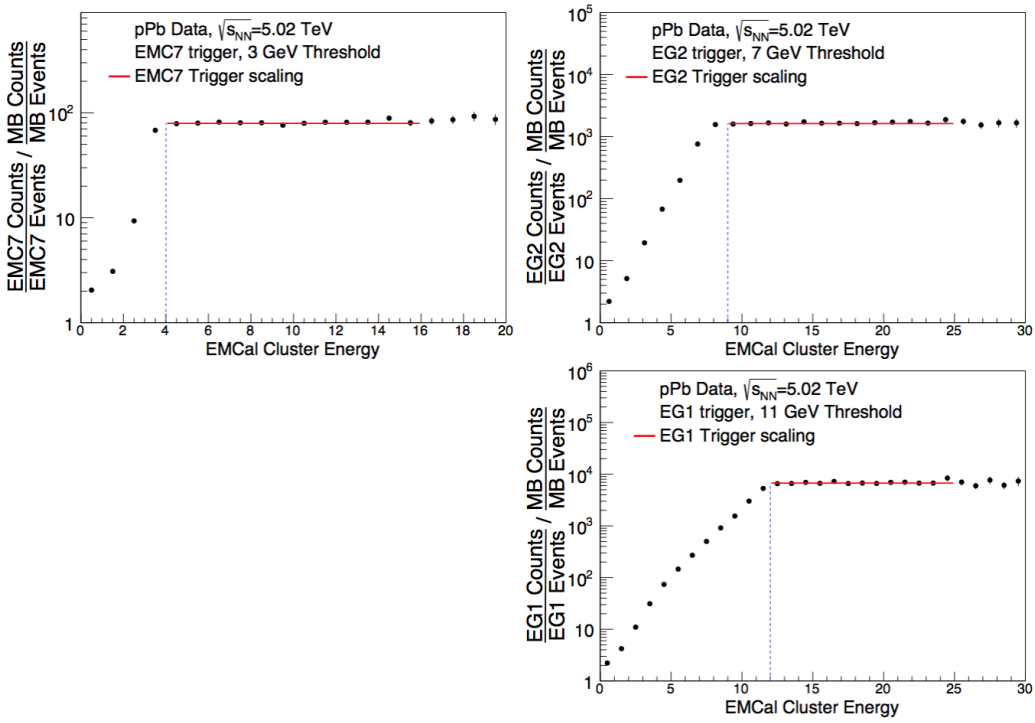


Figure 4.10: Determining the EMC7, EG1 and EG2 Trigger Efficiency. The number of clusters per event in triggered events is divided by the number of clusters per event in minimum bias events. The y-coordinate of the fit is the trigger scaling. pPb collisions at $\sqrt{s_{NN}} = 5.02$ TeV measured in ALICE

The triggered events have a higher number of electrons per event as compared to the minimum bias events. The trigger scaling factor corrects the triggered events to make them equivalent to minimum bias events.

$$\frac{\text{Electrons}_{MB}}{\text{Events}_{MB}} = \frac{\text{Electrons}_{trigger}}{(\text{Trigger Scaling}) \times \text{Events}_{trigger}} \tag{4.1}$$

By dividing the cluster energy spectrum for each trigger with the minimum bias spectrum, the trigger scaling factor can be extracted as seen in figure 4.10. Since the cluster spectrum for the EMC7 triggered events follows the shape of the Minimum Bias triggered events after the trigger threshold, the EMC7 divided by Min Bias cluster spectrum is consistent with a straight line after the trigger threshold. The

y-coordinate of the straight line indicates trigger scaling factor. The same technique was repeated to find the trigger efficiency for EG1 and EG2 triggered events.

Figure 4.11 shows the same plot as figure 4.9 after all of the trigger efficiencies are applied. After the trigger thresholds are applied all of the triggered data points align with the minimum bias data points.

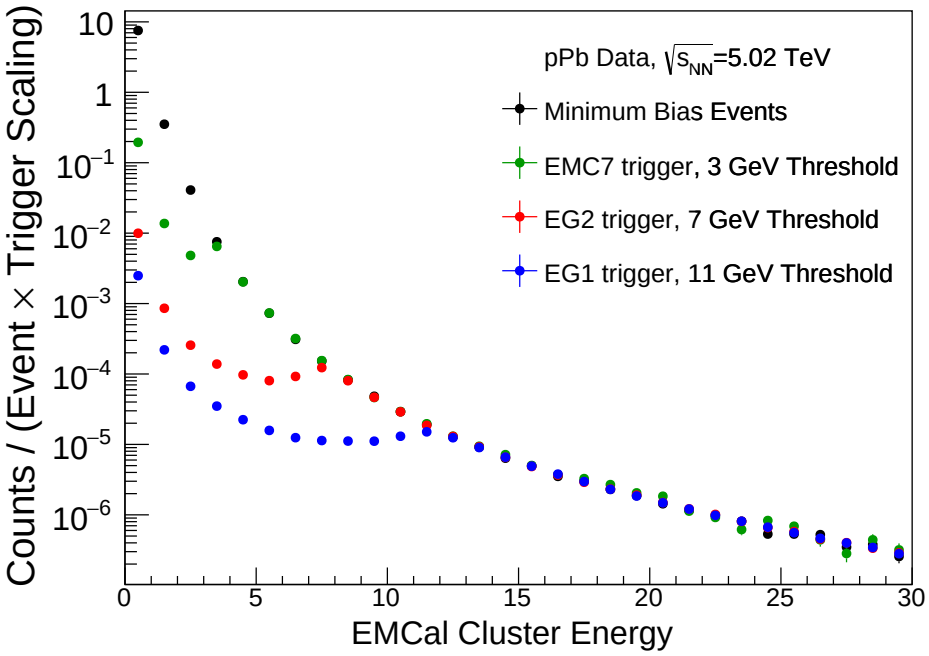


Figure 4.11: EMCal cluster energy for each trigger after trigger efficiencies are applied.

The triggered events can be used to increase the statistics for finding electrons at a higher p_T range since the triggered events have an enhancement of statistics at higher p_T as compared to minimum bias data. However the triggered scaling number introduces a systematic error, since there is some uncertainty in the number. For this analysis, only minimum bias, EG2 and EG1 triggered events were used. The EMC7 sample was found to have lower statistics for electrons and covered a smaller p_T range as compared to minimum bias events. The EMC7 triggered events did not increase the p_T coverage of the analysis and had a larger systematic and statistical error as compared to minimum bias events.

4.6 Particle Identification cuts

It cannot be determined with complete certainty whether a specific track was created by an electron or another particle. Using the known properties and behaviors of the electron we can define some cuts that will enhance the sample for electrons. The cuts may cause some electrons to be lost but the cuts should remove more of the hadron background than electrons, increasing the purity of the electron sample.

4.6.1 TPC electron identification: n_σ^{TPC}

The TPC can identify particles by using the rate of energy loss of the particles as they pass through the gas in the detector. See section 3.5.2 for a more detailed description. Figure 4.12 shows the particle identification using the TPC. In this figure, the x-axis is momentum of the tracks. The y-axis is energy loss of the particles going through the detector, scaled by the number of standard deviations away from the electron hypothesis for energy loss in the TPC. Electrons can be seen as a horizontal line with some width at $n_\sigma^{TPC} = 0$. For this analysis, an asymmetric n_σ^{TPC} cut for electrons of -1 to 3 was used.

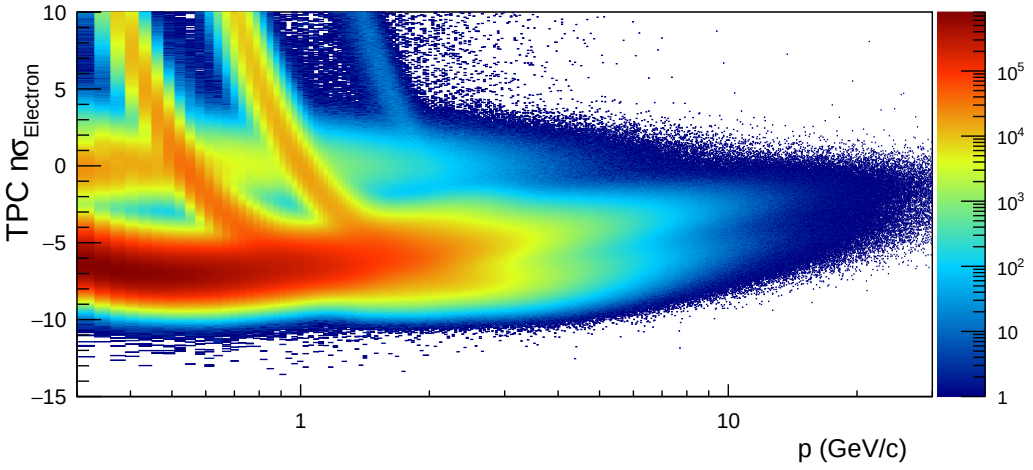


Figure 4.12: Particle identification in the TPC. The vertical axis is the number of sigmas away from the electron hypothesis of energy loss in the TPC. The horizontal axis is the momentum of the track.

The TPC cut works well at lower momenta, but runs out of distinguishing power at momenta above 15 GeV/c. More particle identification cuts are needed in order to get a clean sample of electrons at $p_T > 10$ GeV/c.

4.6.2 EMCal electron identification: E/p

The EMCal responds to electrons and hadrons differently. The E/p measurement can be used to exploit this fact and enhance the sample of electrons.

E/p = (Energy deposited in the EMCal) / (Momentum of the track in the TPC)

The graphic in figure 4.13 shows photons, electrons, and hadrons and their interaction with the detector. The photon does shower in the EMCal and deposits its full energy but does not create a track in the TPC. Photons will not have an E/p measurement since it does not have a track in the TPC and will not have a momentum measurement.

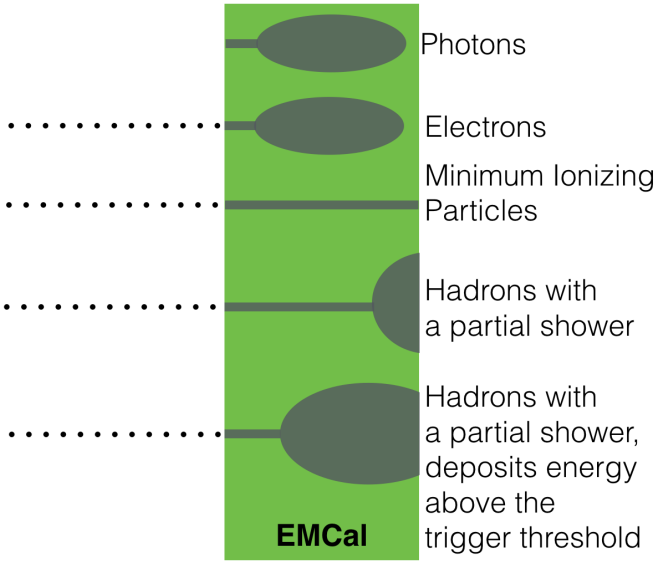


Figure 4.13: Graphic of particle interactions with the EMCal. Photons do not create tracks in the TPC. Electrons and charged hadrons create tracks in the TPC and can deposit energy in the EMCal.

The electron makes a track in the TPC and deposits all of its energy in the EMCal. Electrons observed in ALICE will be moving at relativistic speeds. For relativistic particles, energy is related to momentum by the following equation.

$$E^2 = p^2c^2 + m^2c^4 \tag{4.2}$$

Electrons have a small mass of 0.0005 GeV/c^2 and electrons measured in this analysis have a momentum of $p > 1$ GeV/c. Consequently, $p^2c^2 >> m^2c^4$ and $E \approx p$. The E/p measurement for electrons will be near unity. In general, electrons will be considered in the region $0.8 < E/p < 1.2$.

Hadrons can have a varied response to the EMCal. Hadrons can pass through and deposit a minimum amount of energy in the EMCal. This behavior is called a MIP, or a minimum ionizing particle. The E/p measurement for a MIP will be near zero.

Hadrons can also shower in the EMCal. Some hadrons will deposit a fraction of their energy in the EMCal. For these hadrons, the measured energy divided by the measured momentum will usually be less than one, $E/p < 1$.

EMCal triggered events have an additional E/p component. Since collisions occur in ALICE at a rate faster than can be recorded, the EMCal trigger is used to identify and prioritize saving of events that have a strong signal in the EMCal. Compared to minimum bias events, EMCal triggered events have a larger percentage of high energy-depositing electrons and photons, but also have a larger percentage of high energy-depositing hadrons. EMCal triggered events enhance the signal of electrons, but also add an additional background of hadrons that deposit energy in the EMCal above the trigger threshold. Figure 4.14 shows E/p as a function of energy for minimum bias and EMCal triggered events in pPb collisions in ALICE. In the minimum bias events (top left plot, figure 4.14), the MIP can be seen as a horizontal line near $E/p = 0$. The hadrons with a partial shower are mostly in the range $0 < E/p < 1$ but with a peak near $E/p \approx 0.5$. A horizontal line near $E/p = 1$, representing the electrons, is barely visible in the minimum bias data. The three EMCal triggered events have

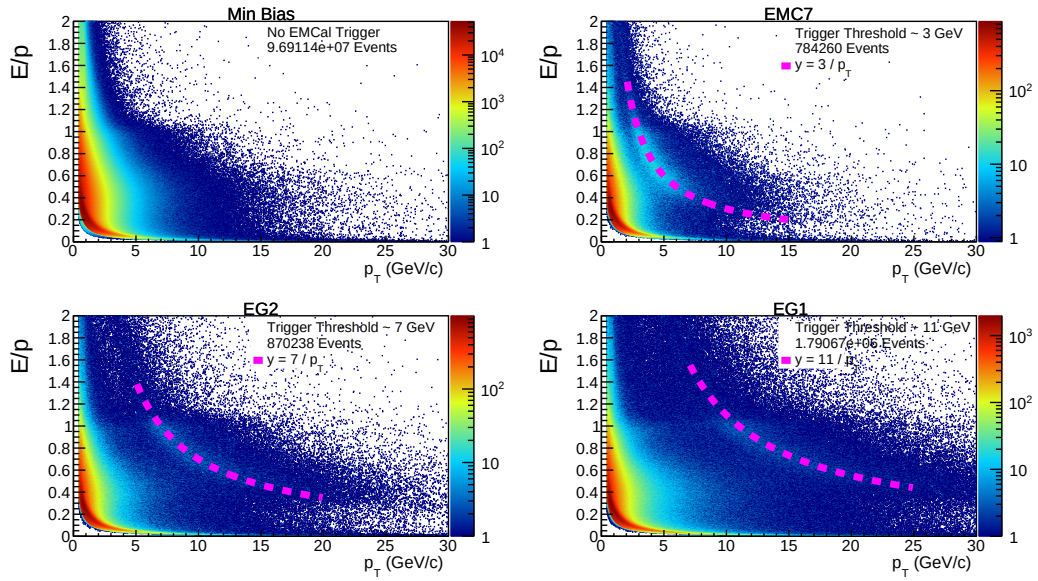


Figure 4.14: E/p for all particles with tracks in the TPC matched to energy clusters in the EMCal. Going clockwise from top left plot shows minimum bias events, EMC7, EG1, and EG2 EMCal triggered events. The EMC7, EG1, and EG2 EMCal triggered events have a function overlaid of $E/p = E_{Threshold}/p_T$ shown in a dotted pink line. All events are pPb collisions at $\sqrt{s_{NN}} = 5.02$ TeV measured in ALICE.

an additional component which can be seen as a crescent shape in each of the three EMCal triggered data sets. This additional component is due to the hadrons that deposited energy in the EMCal above the trigger threshold that fired the EMCal trigger.

The EMC7 triggered data require a cluster in the EMCal with an energy near or above 3 GeV. A hadron that passes the EMC7 trigger will have an E/p measurement of $E/p \geq 3/p$. The EMCal is sitting in the pseudorapidity region $|\eta| < 0.7$ so $p \approx p_T$. In a given energy interval, it is more likely for a particle to have a lower energy than a higher energy. For these reasons, most hadrons that fire the EMC7 trigger will have an $E/p \approx 3/p_T$. The EG1 and EG2 trigger have an energy threshold of 11 and 7 GeV. The EG2 events will have an enhancement of hadrons with $E/p \approx 7/p_T$, and EG1 with $E/p \approx 11/p_T$. To check that this is a good estimation, figure 4.14 has a function overlaid on all of the triggered data sets of $E/p = E_{Threshold}/p_T$. This function seems to describe the peak of this background well.

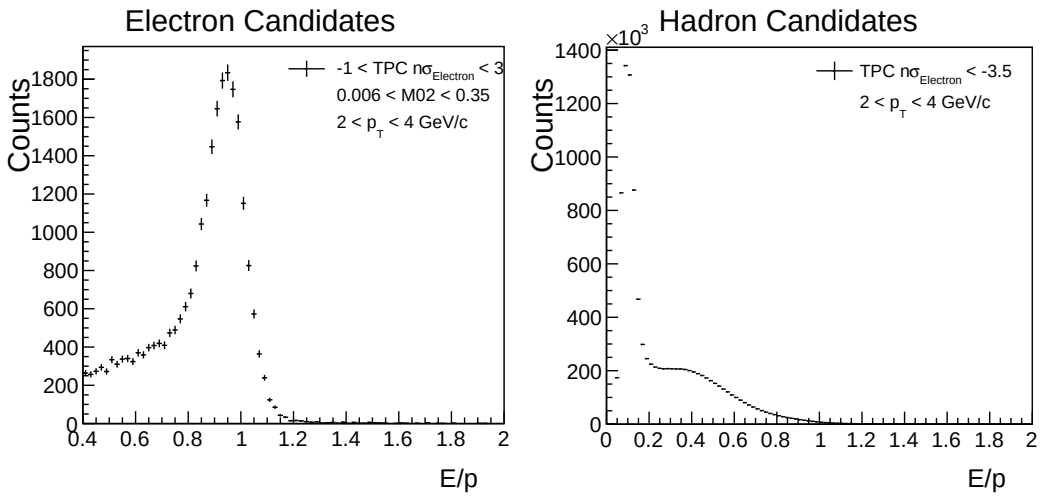


Figure 4.15: E/p for Electrons and Hadrons. Minimum Bias p-Pb collisions at $\sqrt{s_{NN}} = 5.02$ TeV measured in ALICE.

Electrons and hadrons have a different E/p shape. Figure 4.15 shows E/p for minimum bias events in p_T window 2-4 GeV/c. In these plots, the x-axis is E/p, the energy measured in the EMCal divided by the momentum of the track. The y-axis is counts. In the left figure a n_σ^{TPC} and shower shape cut are applied to enhance the signal of electrons. A peak centered near $E/p = 1$ can clearly be seen in the left hand plot.

The plot in the right of figure 4.15 shows the E/p shape for hadrons. The TPC dE/dx information has been used to enhance the sample of hadrons. The minimum ionizing particles create an E/p peak near 0. The hadrons that leave a partial shower in the EMCal are seen around $E/p = 0.4$ with a tail that goes out to 1 in E/p.

It is important to note that the counts in figure 4.15 for the hadrons are much higher than the counts for the electrons. The y-axis for the right plot in figure 4.15 is a factor of 10^3 higher than the left plot. Even at $E/p = 0.8$, the hadron count is much larger than the electron counts (approximately 30,000 to 700). This demonstrates the importance of purifying the electron signal.

4.6.3 EMCal electron identification: M20 and M02

Since electrons have a predictable shower in the EMCal, the background of hadrons can be further reduced by making a cut on the shape that electrons make when showering in the EMCal. Figure 4.16 shows a drawing of electrons and hadrons and the shape of their showers in the EMCal. The left side of this figure shows the side view of the electron and hadron showers. The right side of this figure shows a view from the front face of the EMCal. The right side is indicative of the actual signal coming from the EMCal.

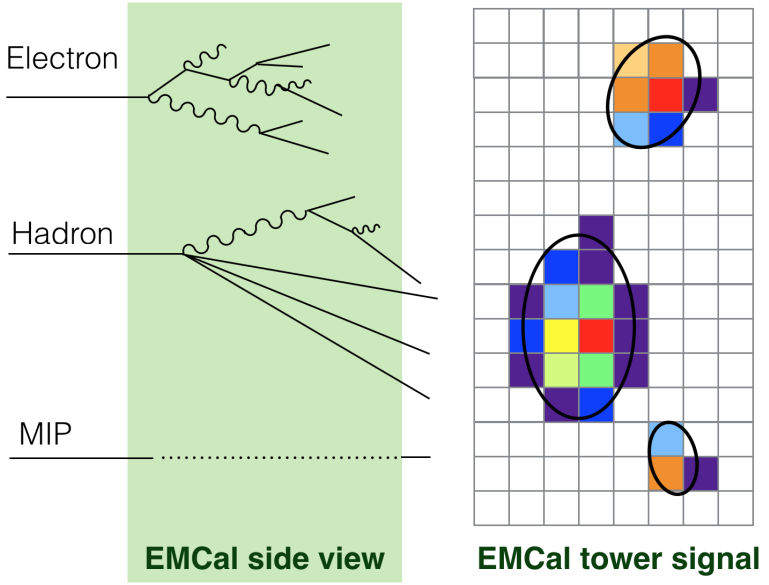


Figure 4.16: Schematic showing electrons and hadrons and the shape of their showers in the EMCal.

The size of a shower from an electron is slightly larger than one EMCal tower. Electrons will usually leave a signal in five to ten adjacent EMCal towers. The shape of the adjacent towers with a signal will be round or ellipsoid.

Hadronic showers are more variable. If a hadron goes through the EMCal without showering (MIP), then the hadron will deposit a signal in one or two towers. If the hadron does shower in the EMCal then the shower size varies substantially. A hadron shower can cover three to fifteen towers. Fully contained hadron shower is larger

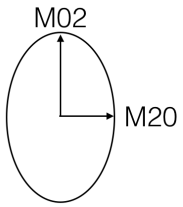


Figure 4.17: M20 and M02 axis defined. M20 is the shorter axis. M02 is the longer axis.

longitudinally and laterally as compared to an EM shower. (For a more in depth discussion on electron and hadron showers in the EMCal, see section 3.6.1 and 3.6.2.)

The electron sample can be enhanced by making a cut on the shower shape that agrees with the electron's behavior in the EMCal. The shower shape parameters are drawn in figure 4.17. The long axis is called M02 ("m-zero-two") and the short axis is called M20 ("m-twenty"). After a cluster is found, the long and short axis is calculated using the cell weights, given by the energy of the signal in the cells, and the coordinates of the cells in the cluster. The equations [71] [65] for M02 and M20 are:

$$M_{02} = \frac{dxx + dzz}{2} + \sqrt{\left(\frac{dxx - dzz}{2}\right)^2 + \left(dxz\right)^2} \tag{4.3}$$

$$M_{20} = \frac{dxx + dzz}{2} - \sqrt{\left(\frac{dxx - dzz}{2}\right)^2 + \left(dxz\right)^2} \tag{4.4}$$

In these equations, 4.3 and 4.4, dxx, dzz and dxz are functions of the position, η_k and ϕ_k, of each k-th cell in the cluster and weighted by the energy in each cell:

$$dxx = \frac{\sum_k w_k \eta_k^2}{\sum_k w_k} - \frac{\left[\sum_k w_k \eta_k\right]^2}{\left[\sum_k w_k\right]^2} \qquad dzz = \frac{\sum_k w_k \phi_k^2}{\sum_k w_k} - \frac{\left[\sum_k w_k \phi_k\right]^2}{\left[\sum_k w_k\right]^2}$$

$$dxz = \frac{\sum_k w_k \eta_k \phi_k}{\sum_k w_k} - \frac{\sum_k w_k \eta_k \sum_k w_k \phi_k}{\left[\sum_k w_k\right]^2} \qquad w_k = w_{0_k} + \log\left(\frac{E_k}{\sum_k E_k}\right)$$

Figure 4.18 shows the shower shape parameters as a function of E/p for two samples. The top two plots have a n_σ^{TPC} cut to enhance the sample of electrons. The two bottom plots have a cut to increase the sample of hadrons. In these plots, electrons are most likely to be found in the top two plots, around $E/p = 1$.

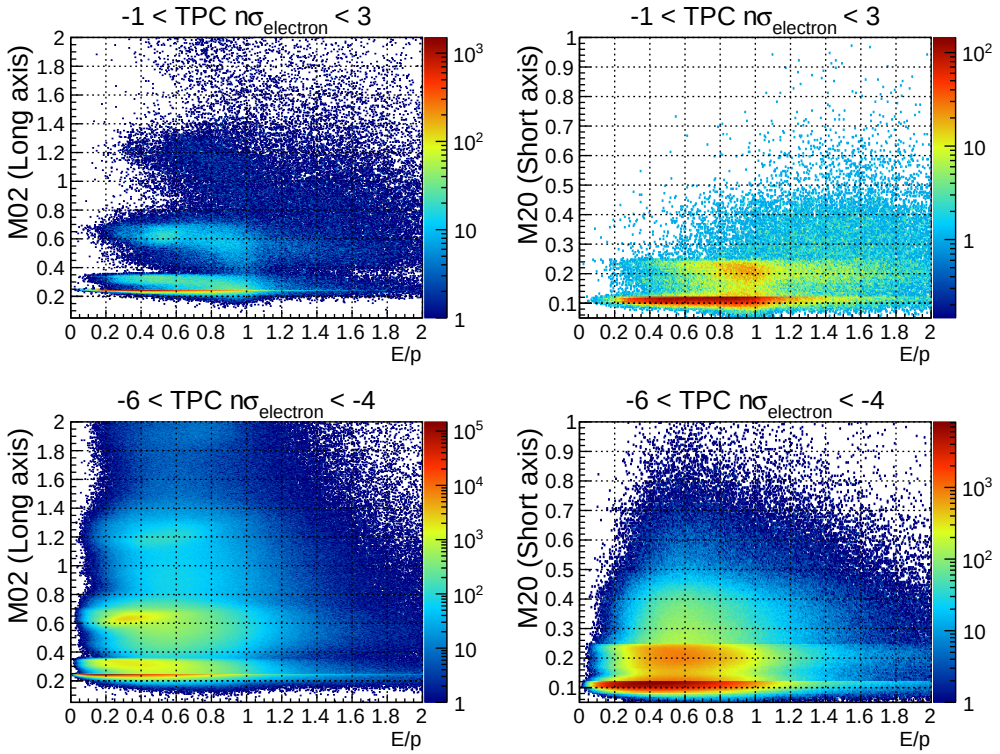


Figure 4.18: The top two plots show the shower shape parameters, M02 and M20, for a sample enhanced with electrons. The bottom two plots show M02 and M20 for a sample enhanced with hadrons. p-Pb collisions at $\sqrt{s_{NN}} = 5.02$ TeV measured in ALICE.

The exact value for the best shower shape cut is not immediately clear from looking at these plots. From comparing the top and bottom left plot in figure 4.18, a

potentially good shower shape cut could be M02 = 0.35, 0.4, or 0.8. From comparing the left plots, a good value for a shower shape cut could be M20 = 0.14, or 0.25.

If a shower shape cut can help enhance the signal of electrons, it will have the most impact in the region $p_T > 10$ GeV/c since the n_σ^{TPC} measurement runs out of distinguishing power at this point. Figure 4.19 shows three E/p p_T windows with various M02 (top three plots) and M20 cuts (bottom three plots). In these figures, the black points do not have any shower shape cut applied. When a shower shape cut is applied, the counts are decreased in the areas $E/p < 0.8$ and $E/p > 1.2$. Applying a shower shape requirement appears to be a good way to remove some hadron contamination. The cut of M20 < 0.14 (orange points) seems to remove the most background, however it also removes some signal. The cuts M20 < 0.35 (green) and M02 < 0.8 (blue) are not removing as much background but also leave the signal intact.

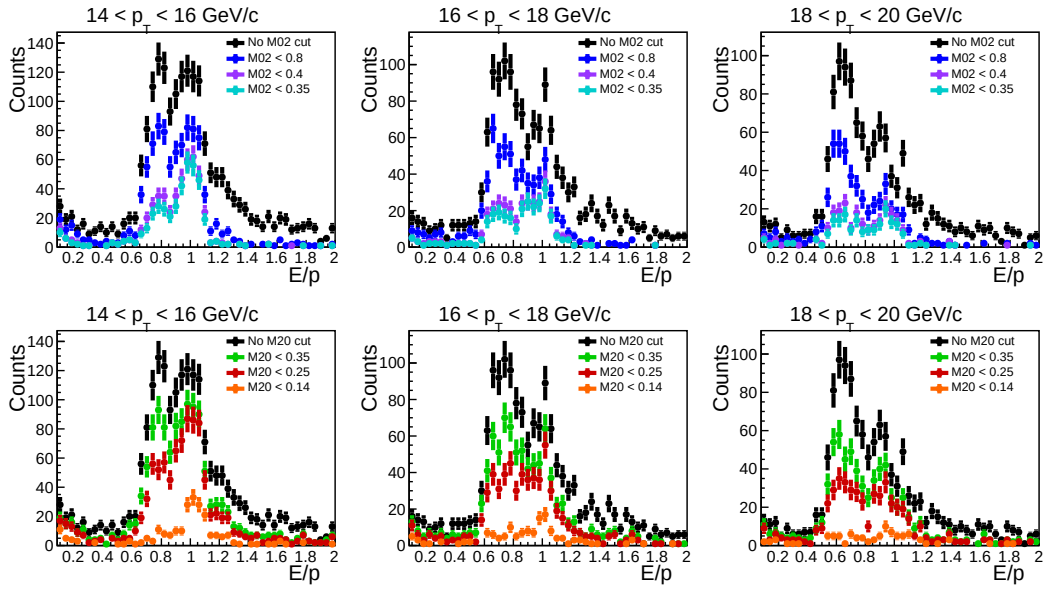


Figure 4.19: E/p plots in EG1 triggered events for various shower shape cuts. All plots include a n_σ^{TPC} cut of -1 to 3. p-Pb collisions at $\sqrt{s_{NN}} = 5.02$ TeV measured in ALICE.

A way of determining the best shower shape cut is to estimate the purity and efficiency for each cut. In order to do this, the E/p plot for each p_T bin was fitted

with a function (see 4.7 for more information). The signal and background were estimated using a fit. Figure 4.20 shows an example of the $10 < p_T < 12$ GeV/c E/p plot for three different shower shape cuts, and no shower shape cut. The purity can be estimated using the signal and background areas.

Purity = (area signal) / (area signal + area background)

The signal was defined as the area between the red and blue curve, between $0.8 < E/p < 1.2$. In figure 4.20, the signal area is shown in red. The background was defined as the area under the blue curve in $0.8 < E/p < 1.2$ and is shown in blue. The background area is almost completely eliminated from the bottom right plot for the cut M20 < 0.14. The purity for this p_T bin will be very high. The top right plot, with no shower shape cut applied, has the largest background area and should have the lowest purity. If the only consideration was purity, then the best cut out of these four would be the M20 < 0.14 shower shape cut.

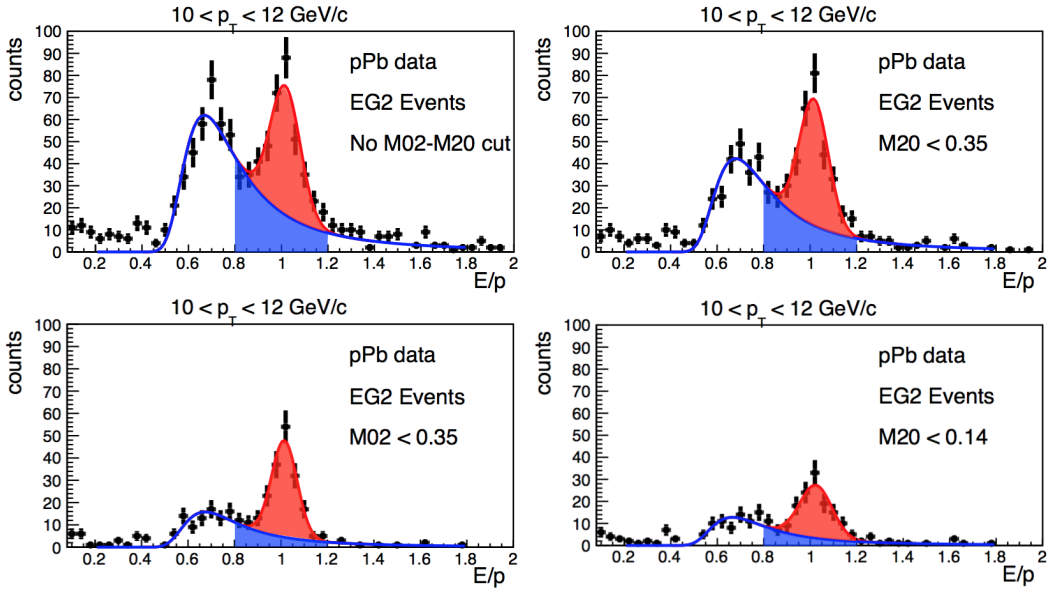


Figure 4.20: E/p plots for $10 < p_T < 12$ GeV/c in EG2 triggered events. All plots include a n_σ^{TPC} cut of -1 to 3. p-Pb collisions at $\sqrt{s_{NN}} = 5.02$ TeV measured in ALICE.

Another consideration is how much signal is being lost with a cut. In figure 4.20, the red signal area is the largest in the E/p plot with no shower shape cut. The red

signal area is the smallest in the E/p plot with M20 < 0.14. Estimating the efficiency of each cut gives an idea of how much signal is retained with a certain cut.

Efficiency = (area signal with cut) / (area signal without cut)

Since the red area in the top right plot in figure 4.20 is almost the same size as the red area in the top left plot, the efficiency for M20 < 0.35 will be near 1. The efficiency for M20 < 0.14 will be the lowest for these plots.

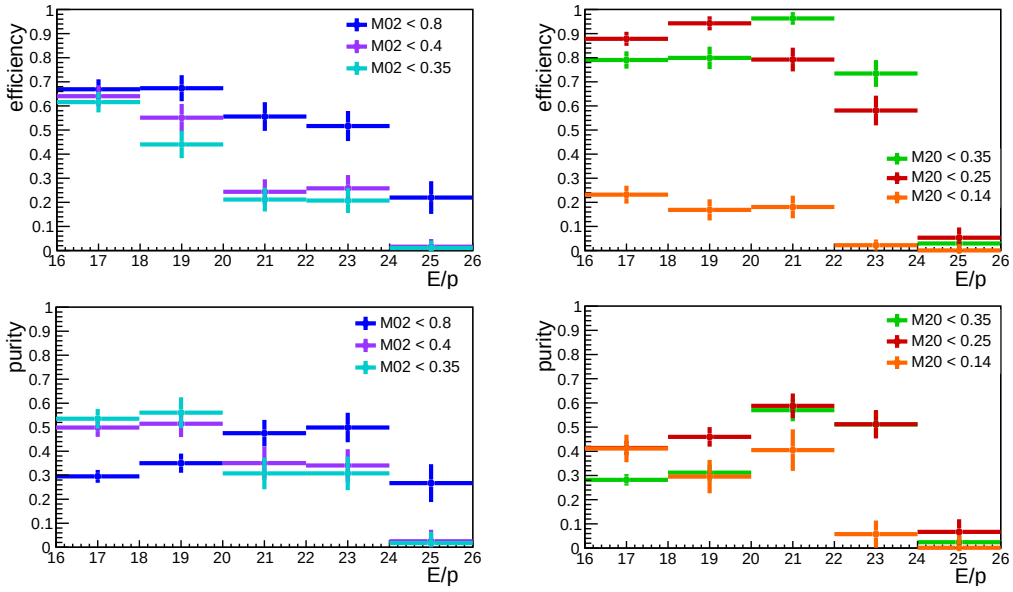


Figure 4.21: Efficiency and purity for various M02 and M20 cuts in EG1 triggered events. p-Pb collisions at $\sqrt{s_{NN}} = 5.02$ TeV measured in ALICE.

Figure 4.21 shows the efficiency and purity for various M02 and M20 cuts. The cuts with the highest purity are M20 < 0.14 and M02 < 0.35. Since these two cuts also remove signal with the background, the p_T range of M20 < 0.14 ends at $p_T = 24$ because the statistics were too low to fit with a function. The M20 < 0.35 cut has the highest efficiency of the shower shape cuts shown. It is important to note that even though the efficiency has a large difference between cuts, the purity is similar for each cut. For example, in the $16 < p_T < 18$ bin, the difference in efficiency for the M20 < 0.35 cut and M20 < 0.14 cut is about 0.6. However the difference in purity is around 0.1. A tight shower shape does not gain much purity, but loses a lot of

efficiency and total statistics. For these reasons a loose shower shape cut such as M20 < 0.35 is ideal.

4.7 Hadron Background Subtraction

In order to get the electron p_T spectrum, the number of electrons in each p_T bin needs to be determined. One method is to look at the E/p measurement in a given p_T window, subtract as much background as possible and estimate the number of electrons. The background can be subtracted knowing the detector response and E/p ranges for electrons and background particles, as explained in section 4.6.2.

Figure 4.15 shows the E/p distribution for electrons and hadrons for minimum bias events. From the left and right figures in figure 4.15, one can see that the electron E/p distribution is Gaussian with a peak around E/p of 1. The hadron distribution has a main peak near E/p of 0, but it also has a little hump around E/p of 0.4 and a tail that continues out past E/p of 1. A rough estimate of the number of electrons in the range $2 < p_T < 4$ can be obtained by integrating the area under the electron peak, $0.8 < E/p < 1.2$ in the left plot in figure 4.15. However there is some hadron contamination under the electron E/p peak that needs to be subtracted away to get the best estimation of the number of electrons.

This analysis used a function to fit the signal and background to obtain the number of electrons. The function took into account the detector response to each component of the E/p signal. For minimum bias events, there are three components that will be seen in E/p windows, background due to the minimum ionizing particles, background due to hadrons with a partial shower, and the electron signal. Under the electron signal, in the range $0.8 < E/p < 1.2$, the main background component will be due to hadrons with a partial shower. The functional form for fitting E/p in minimum bias events is shown in equation 4.5. The background is a wide Gaussian peak. The signal is a narrow Gaussian peak.

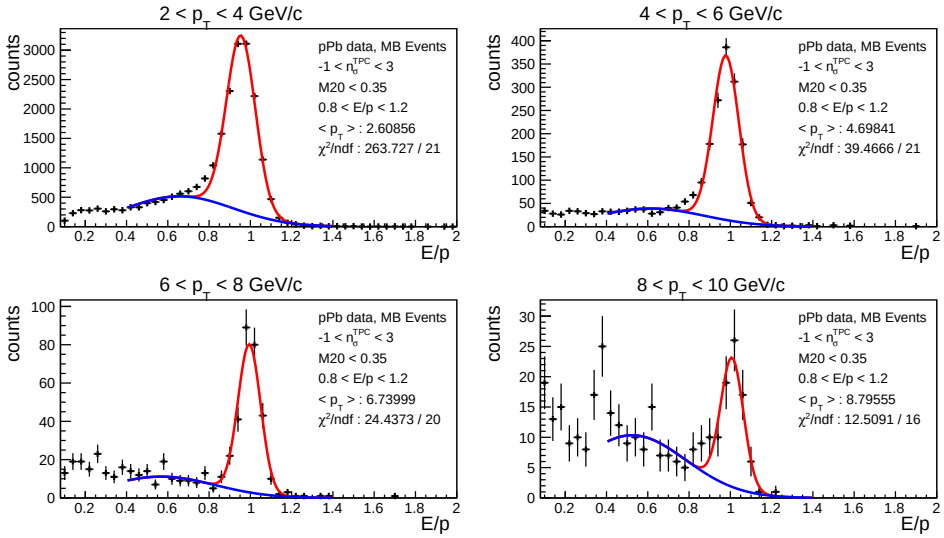


Figure 4.22: E/p in 2 GeV/c p_T windows in Minimum Bias p-Pb collisions at $\sqrt{s_{NN}}$ = 5.02 TeV measured in ALICE. The red line is the total fitting function. The blue line is the background component.

Minimum Bias Events:

f(E/p) = (Hadrons with a partial shower) + (Electrons)

$$f(E/p) \;=\; B \cdot exp\Big(-\frac{[(E/p)-\mu_B]^2}{2\;\cdot\;\sigma_B^2}\Big) \;+\; S \cdot exp\Big(-\frac{[(E/p)-\mu_S]^2}{2\;\cdot\;\sigma_S^2}\Big) \tag{4.5}$$

In this equation, B and S are parameters that are fit to the data. B and S are proportional to the number of counts in the E/p histograms. The values μ_B and μ_S are the position of the peak of the background and the position of the peak of the signal. The background peak position was between $0.4 < E/p < 0.62$. The signal peak position was in the range $0.9 < E/p < 1.1$. The width of the background was fixed to $\sigma_B = 0.26$. The width of the electron peak was $0.055 < \sigma_S < 0.07$.

Figure 4.22 shows the fitting function at work in 2 GeV/c p_T-windows in minimum bias pPb events in ALICE. The red line is the total fitting function as written in equation 4.5. The blue line is only the background components in the fitting function. In this analysis, the number of electrons is proportional to the area between the red and blue curve, between $0.8 < E/p < 1.2$.

The EMCal triggered events had an extra E/p functional component due to the EMCal trigger threshold, as explained in section 4.6.2 and shown in figure 4.14. For EMCal triggered events there are four components that will be seen in E/p windows. The first three components are the same as seen in minimum bias events. The fourth is from the hadrons that fired the EMCal trigger. Under the electron signal, in the range $0.8 < E/p < 1.2$, the main component is due to the hadrons that fired the shower.

The Landau distribution describes the energy loss of charged particles in a thin layer of material. The E/p distributions are the energy lost scaled by the momentum, for a small momentum range. It could be argued that the EMCal is a "thin layer" for charged hadrons since the EMCal is too shallow to fully contain the hadronic shower of the protons, pions, and other charged hadrons. For these reasons, the Landau distribution is a reasonable guess at the form of the background component. The functional form used for the background in triggered data was the Landau distribution with a peak near $E_{Threshold}/p_T$.

EMCal Triggered events:
f(E/p) = (Hadrons that fired the EMCal trigger) + (Electrons)

$$f(E/p) \;=\; B \cdot \text{Landau}((E/p), \mu_B, \sigma_B) \;+\; S \cdot \text{Gaus}((E/p), \mu_S, \sigma_S) \tag{4.6}$$

Just like the minimum bias functional form, B, and S are parameters that are fit to the data and depend on the number of counts in the E/p windows. The value μ_b is the peak position of the background and was $E_{Threshold}/p_T \pm 0.1$. The width of the background, σ_b was set at 0.0775. The signal peak position was in the range $0.9 < \mu_s < 1.1$. The width of the electron peak was $0.055 < \sigma_S < 0.07$.

Figure 4.23 shows the fitting in EG2 triggered events. The red line is the total fit, equation 4.6. The blue line is the background function. The number of electrons is proportional to the area between the red and blue line, in the area $0.8 < E/p < 1.2$.

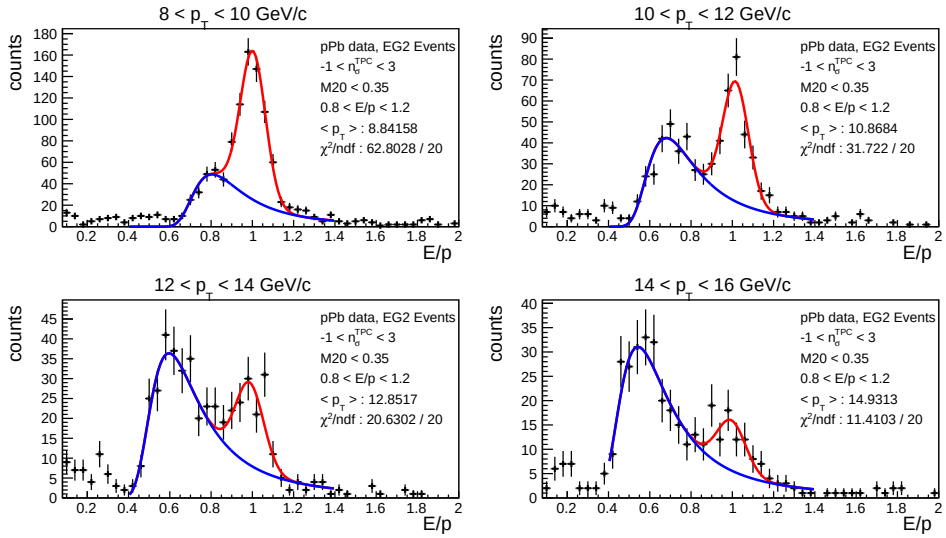


Figure 4.23: E/p fitting shown for EG2 EMCal triggered events, trigger threshold ≈ 7 GeV. p-Pb collisions at $\sqrt{s_{NN}} = 5.02$ TeV measured in ALICE.

4.8 Photonic Electron Background

After finding the electron candidates, and subtracting off the hadron contamination, the remainder is called the "inclusive electrons". Inclusive electrons are the number of measured electrons from all sources. This analysis measured electrons from decays of heavy flavor mesons. It is impossible to tell the origin of a specific electron. However, it is possible to estimate on a statistical basis the number of electrons from various sources and therefore infer the number of heavy flavor electrons. The number of heavy flavor electrons is the inclusive electrons minus the number of electrons from other sources.

Figure 4.24 shows inclusive electron yield (black points) for pp collisions at $\sqrt{s} =$ 7 TeV measured in ALICE [39]. The estimated yield of electrons is drawn for various background sources. The sum total of all background sources, the background "cocktail", is drawn (black line). Sources of electrons include the Dalitz decay of light neutral mesons, namely π^0, η and η' mesons. The decay products from the Dalitz decay of these mesons are a photon and a pair of unlike sign electrons, $\pi^0 \to \gamma + e^+ + e^-$, and $\eta \to \gamma + e^+ + e^-$, and $\eta' \to \gamma + e^+ + e^-$. Photon conversion ("conv. of γ_{meson}")

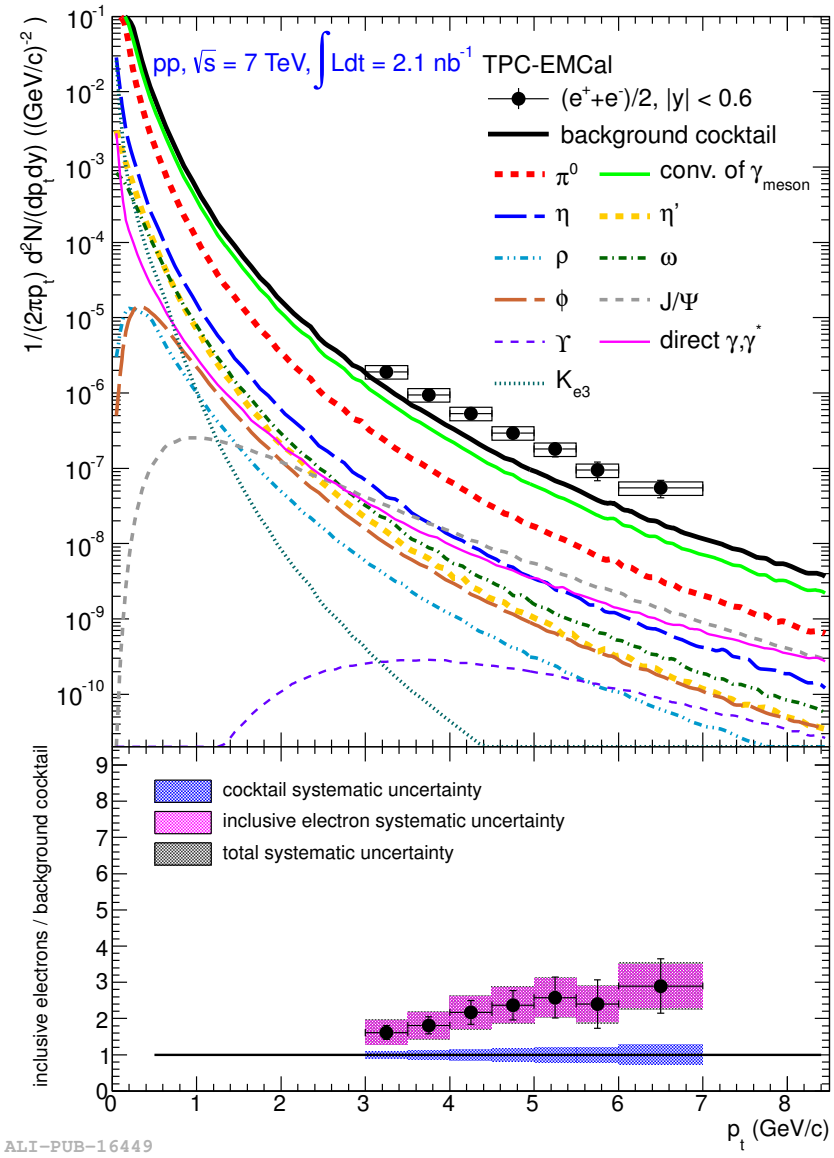


Figure 4.24: Inclusive electron yield and background electron cocktail as a function of p_T for p-p collisions at $\sqrt{s} = 7$ TeV measured in ALICE [39]. Bottom panel shows the ratio of inclusive electron yield to background electron cocktail.

is a large source of electrons. When a photon interacts with matter in the detector material the energy of the photon can be converted into an electron-positron pair, $\gamma \rightarrow e^+ + e^-$. The vector mesons ρ, ω, ϕ have dielectron decay modes. Real and virtual photons ("direct γ, γ^*") that are produced in the collision can also convert

into an electron-positron pair. The charged and neutral kaons have a semileptonic decay mode ("K_{e3}"), $K \rightarrow e\pi\nu$.

The J/Ψ and Υ are mesons with heavy flavor. The J/Ψ is a meson composed of a charm and anti-charm quark. The Υ meson is made up of a bottom and anti-bottom quark. The D and B mesons, measured in this analysis, are composed a single heavy flavor quark and a light quark. The J/Ψ and Υ have different formation time and interact with the medium somewhat differently from the D and B. For these reasons, the J/Ψ and Υ are measured separately from D and B mesons and are considered background of this measurement.

The background sources in figure 4.24 [39] were calculated using a cocktail method. For this thesis, an alternative method was used for measuring background sources called the *invariant mass method*. As can be seen from figure 4.24 the main sources of background electrons are from photon conversion and from Dalitz decay of light mesons, so called *photonic electrons*. The invariant mass method takes advantage of the fact that the main source of background electrons are from sources which produce electrons in pairs, $e^- + e^+$. The invariant mass of electron-positron pairs from photon conversions and from Dalitz decays of neutral mesons is near zero. The number of photonic electrons can be estimated by finding electron-positron pairs and calculating the invariant mass.

Since the inclusive electrons include the signal from heavy flavor electrons and the background from various sources (mainly photonic electrons), the number of heavy flavor electrons is approximately the number of inclusive electrons minus the number of photonic electrons, equation 4.7. The efficiency of finding a pair of photonic electrons is $\epsilon_{Photonic}$.

$$N^{raw}_{HFE} = N_{Inclusive} - N^{raw}_{Photonic}/\epsilon_{Photonic} \tag{4.7}$$

The photonic electron subtraction does not include the sources of real electrons from the decays of neutral kaons, J/Ψ, Υ, and W and Z bosons. The invariant yield

of the electrons from the decay of the W and Z bosons has a near constant shape across p_T, while the invariant yield of the electrons from heavy flavor decreases across p_T. Therefore the yield of electrons from the W and Z bosons is most important at higher p_T, around $p_T > 20$ GeV/c, and the yield may rival the photonic electron background yield in this p_T region. These background sources that are not included in the photonic electron subtraction were estimated to be smaller than the systematic error, and therefore negligible. Neglecting these background contributions would constitute a modest, one-sided, contribution to the overall systematic error. This systematic error would be dominated by other contributions, mainly the systematic error due to hadron background determination from fitting. (See table 4.8 for the magnitude of various systematic errors in this analysis.)

Steps involved in the Invariant Mass Method:

1. Find an electron candidate with a track that has a good match to an EMCal cluster. To be an electron candidate it must pass the electron identification cuts, $-1 < n_\sigma^{TPC} < 3$, $0.8 < E/p < 1.2$, and M20 < 0.35.

2. Loop over all of the other tracks in the event. Find an associated track that passes the associated track cuts shown in table 4.2. The associated track cuts are loose in order to increase the chances of finding a photonic pair.

Table 4.2: Cuts on associated track.

TPC number of clusters	> 80
p_T	> 0.3
Eta	-0.9, 0.9
n_σ^{TPC}	-3.5, 3.5
TestFilterMask	kTrkTPCOnly
TPC and ITS refit	yes
χ^2/NDF track	< 4.0
reject kink daughters	yes

3. Check the sign of the charge of the original and associated track. If they have the same charge, $e^+ + e^+$ or $e^- + e^-$, then they are tagged as Like Sign pairs (LS). If the charges do not match, they are labeled as Unlike Sign pairs (ULS), $e^- + e^+$.

4. Calculate the invariant mass of the original and associated track. The square of the invariant mass is given in equation 4.8 for relativistic particles.

$$M^2 = 2p_{T1}p_{T2}(cosh(\eta_1 - \eta_2) - cos(\phi_1 - \phi_2)) \tag{4.8}$$

5. If the calculated invariant mass is less than the invariant mass cut, then the original electron candidate is tagged as having found a LS or ULS pair. The invariant mass cut chosen was 0.15 GeV/c^2.

Two random opposite sign electrons can be consistent by chance with an invariant mass near zero without originating from a photon. The Like Sign (LS) pairs can be used to estimate the number of the uncorrelated pairs since there are few known processes that produce electron pairs of the same sign. The difference between Unlike Sign (ULS) and LS gives the number of photonic pairs. $N_{Photonic} = N_{ULS}$ - N_{LS}.

Figure 4.25 shows the invariant mass distribution for LS and ULS electron pairs. The difference between ULS and LS is also shown. Due to electrons from photon conversions, there is a distinct peak for invariant mass near zero in the ULS and ULS-LS distributions. There is a minimum in the invariant mass ULS-LS distribution around 0.1 GeV/c^2.

The invariant mass for photonic electrons is near zero, however the exact numerical value for the cut off point to be tagged as a photonic electron is subjective. Figure 4.26 shows the LS and ULS p_T distribution for electron candidates for various invariant mass cuts in EG2, 7 TeV trigger threshold, events for pPb collisions measured in ALICE. Three invariant mass cuts, 0.18, 0.15, and 0.12 GeV/c^2, are shown for unlike

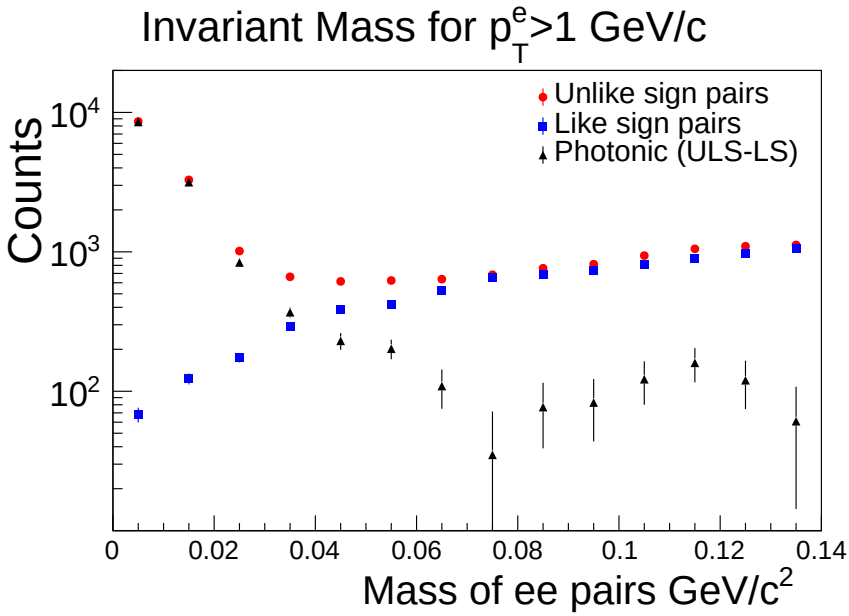


Figure 4.25: Invariant mass of pairs of electrons with a $p_T > 1$ GeV/c in pPb collisions at $\sqrt{s} = 5.02$ TeV measured in ALICE. Unlike Sign Electrons, Like Sign Electrons, and the difference, ULS - LS, is shown.

sign and like sign pairs. The yield of ULS and LS electrons are dependent on the value of the invariant mass cut chosen. A larger invariant mass cut produces a slightly greater yield of LS and ULS electrons across the full p_T range.

Changing the invariant mass cuts does impact the yield of LS and ULS electrons, but how does changing the invariant mass cut effect the yield of photonic electrons? In figure 4.27, the p_T distribution for the difference, ULS-LS, is shown for various invariant mass cuts in minimum bias data for pPb collisions measured in ALICE. The same invariant mass cuts as in figure 4.26 are shown here. The yields of ULS-LS all agree within error bars for the three invariant mass cuts plotted. The ratio of the yield for the 0.18 GeV/c^2 cut divided by the yield for the 0.15 GeV/c^2 cut, and the ratio of the yield for the cut 0.12 GeV/c^2 divided by the yield for 0.15 GeV/c^2 cut is also shown. Varying the invariant mass cut does not seem to greatly effect the yield of photonic electrons. The invariant mass cut chosen in this analysis was 0.15 GeV/c^2.

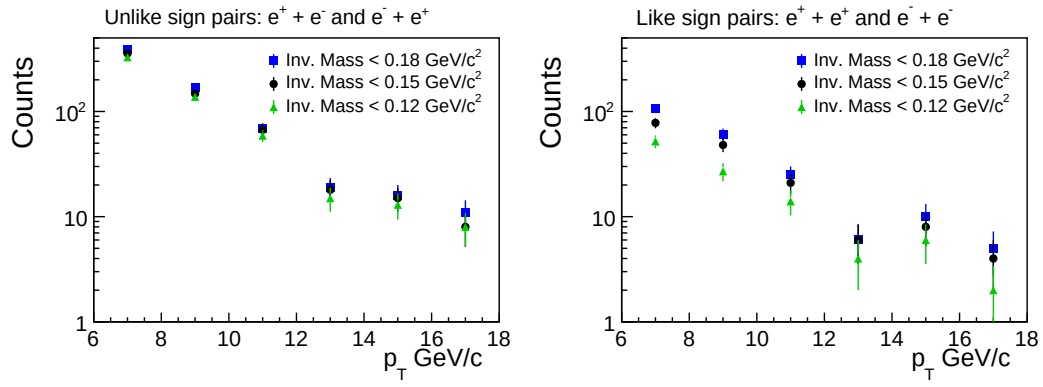


Figure 4.26: The yield with respect to transverse momentum of and Unlike Sign (left plot) and Like Sign (right plot), electron pairs are shown for three invariant mass cuts, 0.18, 0.15, and 0.12 GeV/c^2 are shown for EG2 pPb collisions at $\sqrt{s} = 5.02$ TeV, measured in ALICE.

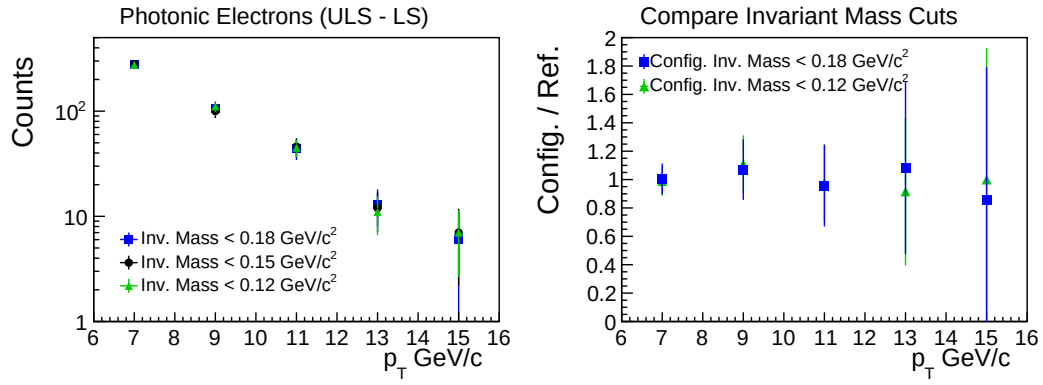


Figure 4.27: Yield of photonic electrons (Like Sign - Unlike Sign) with respect to transverse momentum for various invariant mass cuts are shown for minimum bias pPb collisions at $\sqrt{s} = 5.02$ TeV, measured in ALICE. The ratio of the yield in configuration/reference is also shown, where the reference cut is 0.15 GeV/c^2. The configuration cut is 0.18 GeV/c^2 and 0.12 GeV/c^2

The minimum bias data for photonic electrons run out at about $p_T \sim 10$ GeV/c. However with the use of the EMCal triggered data, the inclusive electron data in pPb events reach up to $p_T \sim 30$ GeV/c. In order to get the heavy flavor spectrum, a photonic electron spectrum with the same p_T range as the inclusive electron p_T range is needed. Figure 4.28 shows the yield of photonic electrons for Min Bias, EG1 and EG2 triggered events. The yields were scaled by number of events and the efficiency of the trigger for triggered events. The distribution of the yields for

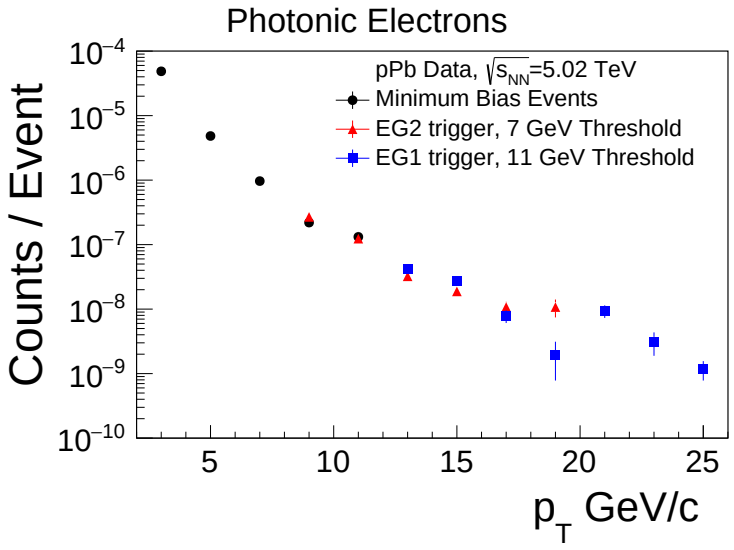


Figure 4.28: Photonic Electrons per event with respect to p_T for Min Bias, EG1 and EG2 triggered events. pPb collisions at $\sqrt{s} = 5.02$ TeV, measured in ALICE. Invariant mass cut is 0.15 GeV/c^2.

photonic electrons for minimum bias and EMCal triggered events align when using the trigger scaling. Adding EMCal triggered events in order to extend the p_T reach of the photonic electron data appears to be appropriate.

The efficiency for tagging a photonic electron was measured by another analysis in ALICE [72] [73]. The efficiency is shown in figures 4.29 and 4.30 for two different p_T ranges. The same method, partner cuts, and invariant mass cuts were used in figures 4.29 and 4.30 as in this analysis so the efficiency of finding a photonic electron should be the same. From figure 4.30, the efficiency for tagging a photonic electron pair appears to be nearly a constant as a function of p_T for $p_T > 8$. The photonic reconstruction efficiency for $20 > p_T > 30$ was assumed to be constant, extrapolating from figure 4.30.

The number of heavy flavor electrons can be found using the number of inclusive electrons and photonic electrons, equation 4.7. Figure 4.31 shows the number per event of inclusive and photonic electrons. In this plot, the number of photonic electrons is corrected by the efficiency of tagging a photonic electron, $\epsilon_{Photonic}$.

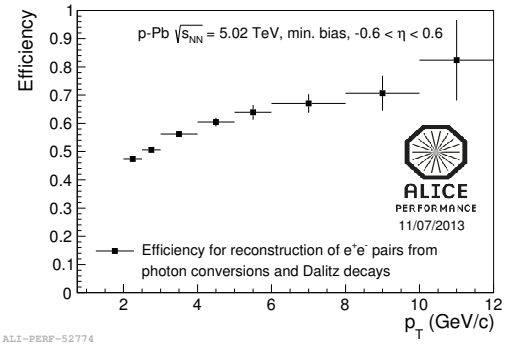


Figure 4.29: Efficiency of reconstructing a photonic electron [72].

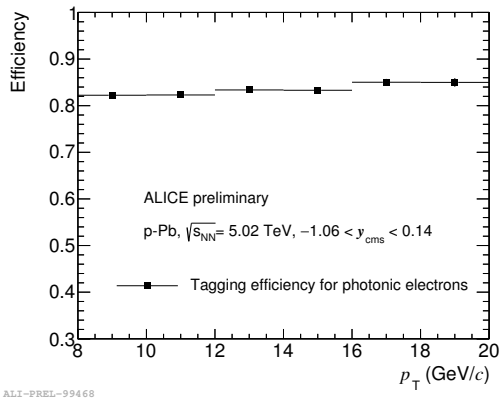


Figure 4.30: Efficiency of tagging a photonic electron [73].

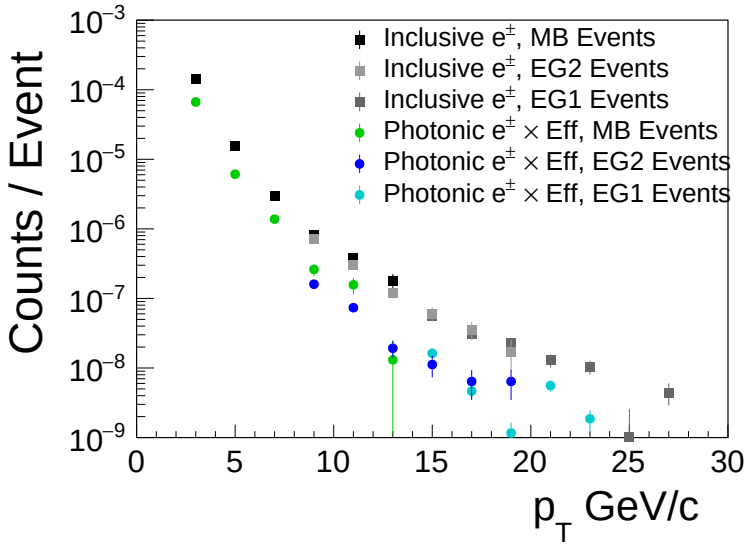


Figure 4.31: Inclusive electrons and photonic electrons are shown per event for Min Bias, EG1 and EG2 pPb collisions at $\sqrt{s} = 5.02$ TeV measured in ALICE. Invariant mass cut used is 0.15 GeV/c^2.

4.9 Acceptance and Efficiency

The total acceptance and efficiency was obtained by using Monte Carlo simulations. The Monte Carlo production used in this analysis was LHC14b3c, which is anchored to the LHC13e run. This production was enhanced with heavy-flavor electrons up to p_T of 30 GeV/c. The event generator used in the Monte Carlo production was

HIJING. The particles generated were then propagated through the detector using GEANT3.

$$\text{Total Acceptance} \times \text{Efficiency} = \frac{\text{Electrons reconstructed with the analysis}}{\text{Electrons generated in MC simulation}} \quad (4.9)$$

The method is given in equation 4.9. The numerator is given by number of electrons that were reconstructed using the same algorithms and cuts used in the data analysis.

The numerator and denominator for equation 4.9 are shown in figure 4.32. The red points are the number of heavy flavor electrons reconstructed using the data analysis method. The blue points are the number of heavy flavor electrons generated.

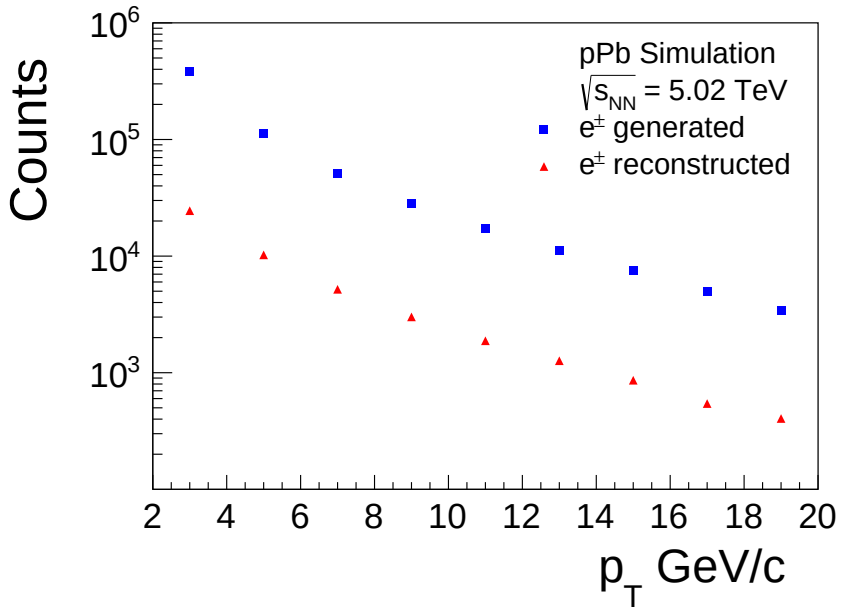


Figure 4.32: Heavy flavor electrons generated and reconstructed for Monte Carlo simulations

The acceptance and efficiency can be written in terms of the following four factors: ϵ^{geo}, ϵ^{reco}, ϵ^{eID}, $\epsilon^{track-cluster-matching}$.

$$\text{Total Acceptance} \times \text{Efficiency} = \epsilon^{geo} \times \epsilon^{reco} \times \epsilon^{eID} \times \epsilon^{track-cluster-matching} \quad (4.10)$$

The factor ϵ^{geo} is the geometrical acceptance of the detector. This factor accounts for the fact that the electrons can only be measured in the active area of the detectors used in this analysis. The detector that covers the smallest active area in ϕ and η space is the EMCal. This analysis is limited by the geometrical size of the EMCal since a signal in the EMCal is required to identify electrons. The electrons in the numerator and denominator were given a cut of $-0.6 < \eta < 0.6$, the same as the analysis acceptance. The electrons were generated across all of $0 < \phi < 2\pi$, but were only found in the EMCal acceptance region $\sim 107°$.

The factor ϵ^{reco} is the reconstruction efficiency which determines how well the hits in the ITS and TPS were reconstructed into tracks. The efficiency that the electrons pass the identification cuts are given by ϵ^{eID}. This includes the cuts $-1 < n_{\sigma}^{TPC} < 3$, $0.8 < E/p < 1.2$ and M20 < 0.35. The efficiency of how well tracks are matched to EMCal clusters is given by $\epsilon^{track-cluster-matching}$.

The total acceptance and efficiency is shown in figure 4.33. The total acceptance and efficiency varies between 0.5 to 0.12 in the region $2 < p_T < 20$. There is more background at low p_T which lowers the efficiency. At high p_T the tracks are straighter, making them easier to reconstruct.

4.10 Error Analysis

Sources of uncertainties in this analysis are due to systematic errors associated with particle identification cuts, systematic errors of the background determination from fitting, uncertainty in the trigger scaling, and systematic errors of the photonic electron background.

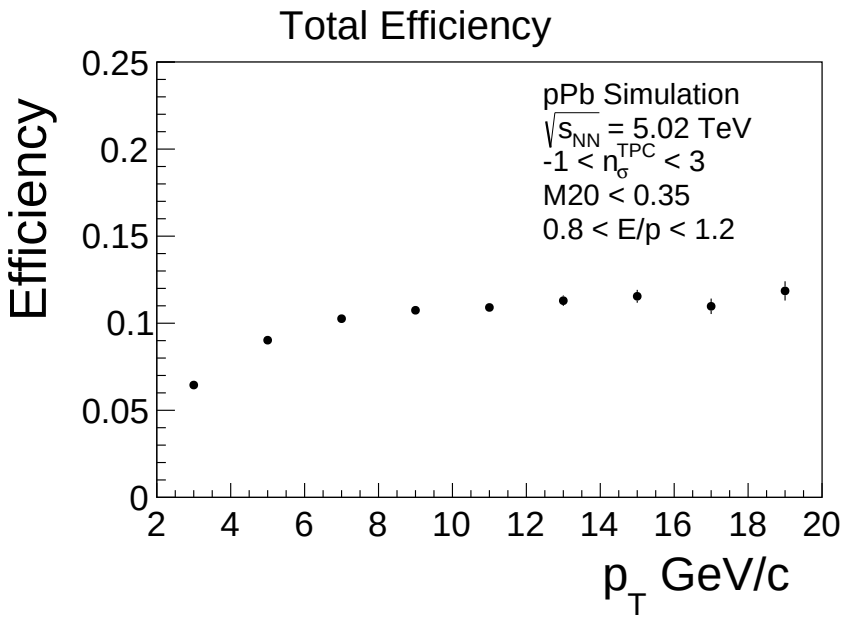


Figure 4.33: Total acceptance × efficiency as a function of p_T for heavy flavor electrons. pPb Monte Carlo simulation.

4.10.1 Particle identification systematics: n_σ^{TPC}

In order to determine the magnitude of the systematic error of the particle identification cuts, the cut is varied and the spectra of heavy flavor electrons is calculated with the varied cut. The ratio of the yield of heavy flavor electrons for the reference and the variation gives an approximate size of the systematic effect of the cut [74]. The ratio is fitted with a straight line to find the magnitude of the systematic error.

The reference spectrum has the particle identification cuts of -1 $< n_\sigma^{TPC} <$ 3, M02 $<$ 0.35, and $0.8 < E/p < 1.2$. The variation spectrum only differs from the reference by one PID cut at a time. For example,

Reference:	-1 $< n_\sigma^{TPC} <$ 3	M02 $<$ 0.35	$0.8 < E/p < 1.2$
Variation:	-0.8 $< n_\sigma^{TPC} <$ 3	M02 $<$ 0.35	$0.8 < E/p < 1.2$

For brevity, in the following tables and plots the only cuts that are different from the reference cuts will be explicitly stated.

The equation for the invariant yield is given by 5.1. The geometrical acceptance, p_T bin size, and number of events accepted will be the same for the default and variation ID cuts. With a tighter electron identification cut, the number of electrons found will be smaller. However, the efficiency of finding an electron will also be smaller with a tighter identification cut. Given a perfect detector and infinite statistics, the two yields should be identical. The difference in spectra is assumed to be due to the systematic error in the particle identification cut.

The n_σ^{TPC} cut was used to enhance electrons. Most of the background contamination is on the negative side of n_σ^{TPC} so the default cut chosen was asymmetrical, $-1 < n_\sigma^{TPC} < 3$. Table 4.3 lists the variations used to determine the systematic uncertainty of the TPC PID cut.

Table 4.3: Table of n_σ^{TPC} variation cuts

Reference:	$-1 < n_\sigma^{TPC} < 3$			
		Effect at p_T 2-10	8-16	14-30 GeV/c
Variation:	$-1.25 < n_\sigma^{TPC} < 3.5$	-1%	+6%	+7%
Variation:	$-1.2 < n_\sigma^{TPC} < 3$	-1%	+2%	+4%
Variation:	$-1 < n_\sigma^{TPC} < 3.5$	negl.	negl.	negl.
Variation:	$-1 < n_\sigma^{TPC} < 2.5$	negl.	negl.	negl.
Variation:	$-0.8 < n_\sigma^{TPC} < 3$	-1%	+3%	+2%
Variation:	$-0.5 < n_\sigma^{TPC} < 1$	-1%	-6%	+1%
Total Effect:		±1%	±6%	±7%

Changing the positive side of the n_σ^{TPC} produces a negligible effect. This is expected because there is little background contamination on the positive side of $n_\sigma^{TPC}$and because the number of electrons should change very little at 3σ away from the electron signal. Changing the cut on the negative side has a more noticeable effect.

Figure 4.34 shows a sample of plots for the n_σ^{TPC} cut systematics. All of the plots have the variation of $-1.25 < n_\sigma^{TPC} < 3.5$. The left figure shows Minimum Bias events for $2 < p_T < 10$. The ratio of the variation yield to the reference yield is approximately 0.9896, indicating a systematic effect of -1% in this p_T range. The

middle figure shows EG2 events, with a trigger threshold around 7 GeV. The effect in middle plot, $8 < p_T < 16$, is approximately +6%. The right plot shows EG1 events that have a trigger threshold of about 11 GeV/c. The ratio indicates approximately a +7% effect in the $14 < p_T < 30$ region.

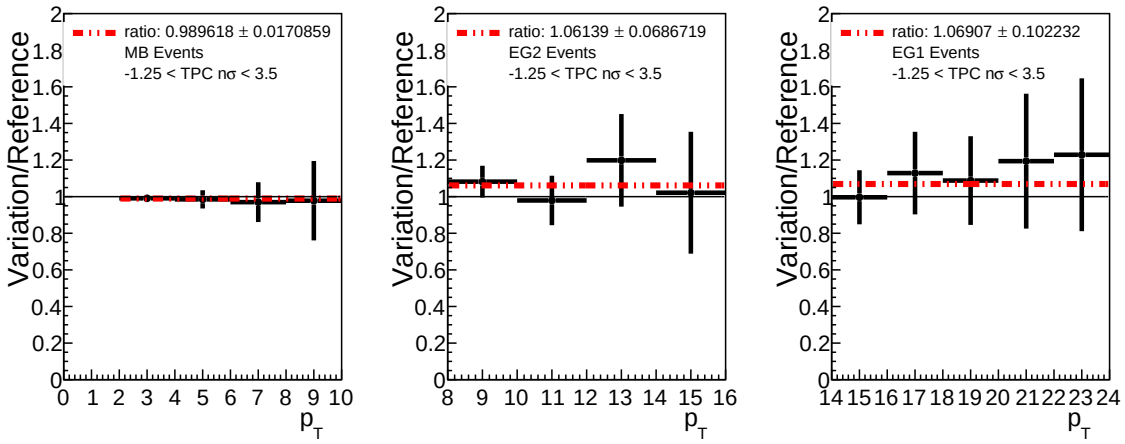


Figure 4.34: Estimating the systematic effect of the n_σ^{TPC} cut. The variation configuration has a cut of -1.25 < n_σ^{TPC} < 3.5. The reference cut is -1 < n_σ^{TPC} < 3. pPb collisions at $\sqrt{s} = 5.02$ TeV, measured in ALICE.

4.10.2 Particle identification systematics: Shower Shape

The same procedure from the n_σ^{TPC} systematics was applied to the shower shape cut. The default cut chosen for this analysis was M20 < 0.35. Table 4.4 shows a list of tighter and looser cuts on M20 that was used to determine the systematics. (Refer to figure 4.18 to see common values for M20 for electrons and hadrons.) The shower shape cut was determined to have a weak systematic effect at low p_T and an effect of ±6% at high p_T. Table 4.4 shows the systematic errors in each p_T range of the variations that were implemented and the total systematic effect of the shower shape cut.

Figure 4.35 shows some example plots for the shower shape systematics. For low transverse momentum, $p_T < 10$, the shower shape cut has a weak systematic effect.

Table 4.4: Table of shower shape variation cuts

Reference:	M02 < 0.35			
		Effect at p_T 2-10	8-16	14-30 GeV/c
Variation:	M20 < 0.38	-1%	-1%	-5%
Variation:	M20 < 0.32	+1%	+2%	+1%
Variation:	M20 < 0.3	+1%	+1%	+2%
Variation:	M20 < 0.28	-1%	+2%	+4%
Variation:	M20 < 0.25	-1%	-1%	+6%
	Total Effect:	±1%	±2%	±6%

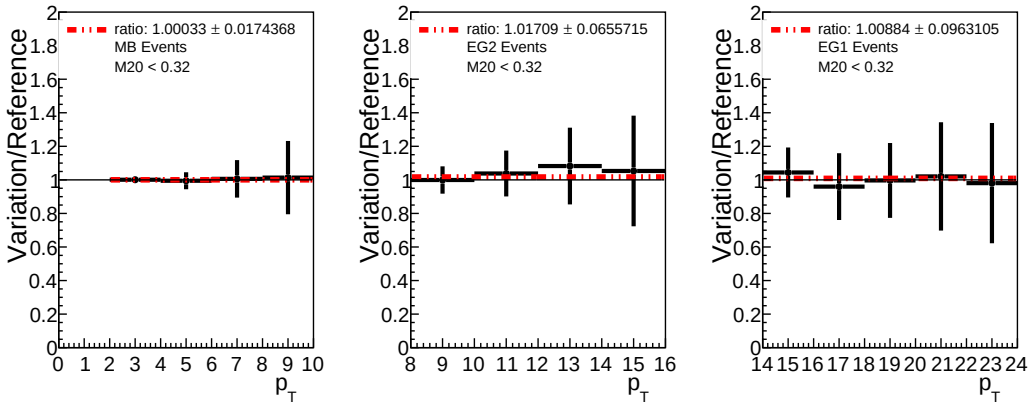


Figure 4.35: EMCal Shower Shape systematic effect. The reference cut is M20 < 0.35. pPb collisions at $\sqrt{s} = 5.02$ TeV, measured in ALICE.

4.10.3 Particle identification systematics: E/p

Electrons are expected to have an E/p near unity. The default cut was chosen to be $0.8 < E/p < 1.2$. Table 4.5 shows the variations of E/p cuts used to determine the systematics. Various looser and tighter cuts on E/p were studied. Minimum bias data were the most sensitive to the E/p cuts. This is most likely due to the fact that the E/p signal peak varies between 0.95 and 1.0 in minimum bias data, which is not reproduced in the Monte Carlo simulations.

Figure 4.36 shows a representative plot for the E/p systematic determination. These plots show the tighter cut variation of $0.825 < E/p < 1.175$ as compared to the reference cut for minimum bias, and EG2 and EG1 triggered data.

Table 4.5: Table of E/p variation cuts

Reference:	$0.8 < E/p < 1.2$			
		Effect at p_T 2-10	8-16	14-30 GeV/c
Variation:	$0.75 < E/p < 1.2$	-5%	-2%	-2%
Variation:	$0.775 < E/p < 1.225$	-3%	-2%	-2%
Variation:	$0.8 < E/p < 1.3$	-1%	-2%	-4%
Variation:	$0.8 < E/p < 1.1$	-1%	-2%	+2%
Variation:	$0.825 < E/p < 1.175$	+3%	+2%	+1%
Variation:	$0.85 < E/p < 1.15$	+5%	+3%	+2%
Total Effect:		±5%	±3%	±4%

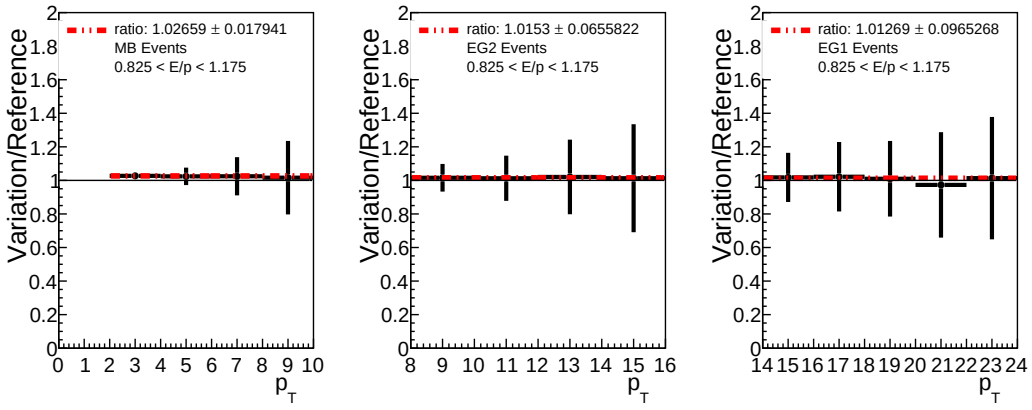


Figure 4.36: EMCal E/p systematic effect. The reference cut is $0.8 < E/p < 1.2$. pPb collisions at $\sqrt{s} = 5.02$ TeV, measured in ALICE.

4.10.4 Background Determination Systematics

There is a systematic error in the expected number of electrons due to not knowing the exact function to use to fit the background and signal in the E/p windows. (Refer to 4.7 for more information on background fitting and subtraction.) To estimate the size of this systematic error, the fitting function was varied. The ratio of number of electrons found with the varied and default fitting function gives an estimation of the size of the fitting systematic error.

To estimate the size of the systematic error due to the background fitting, an exponential function and second order polynomial function was used for the variation background function. The settings of the default function were also varied. Figure

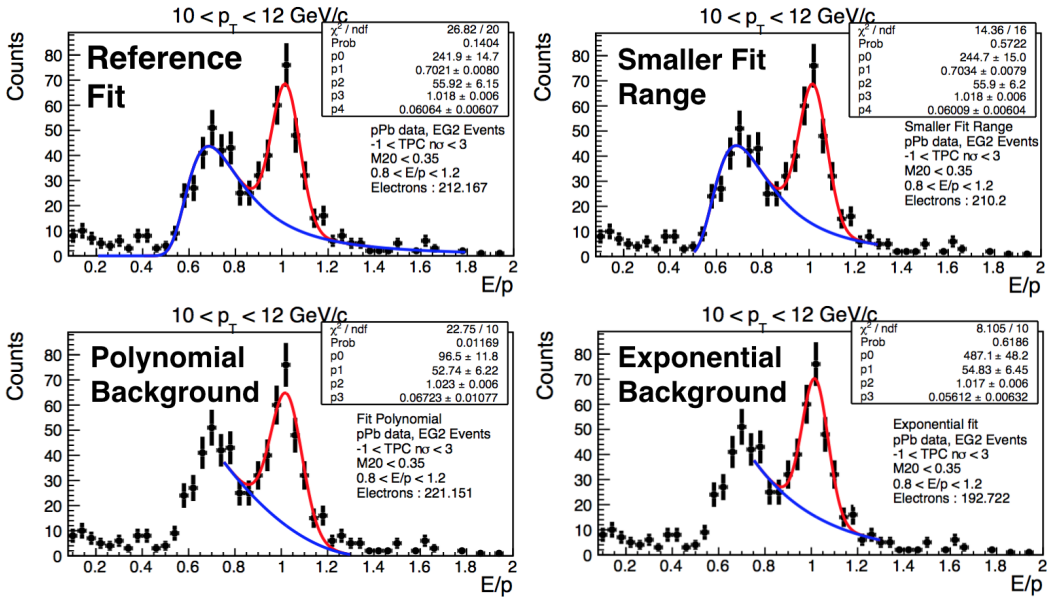


Figure 4.37: Fitting E/p windows with various functions in pPb collisions at $\sqrt{s} = 5.02$ TeV, measured in ALICE.

4.37 shows the default fitting function and three sample functions tried for the same p_T range and PID cuts. The top left plot shows the default fit with the default PID cuts. In the top right plot, the default function was used but the range of the fit region was decreased. Altering the range of the fit region modified the shape of the background function slightly, which can enhance or reduce the number of electrons found. In the bottom left plot, a second order polynomial function was used for the background function. The polynomial function in this plot created a larger signal area and a smaller background area as compared to the default, causing the number of electrons found to be increased for this p_T bin. In the bottom right plot, an exponential function was used for the background. The exponential function has less of a bend as compared to the reference fit, which has a result of estimating a larger background area. The number of electrons found was slightly less for this p_T bin.

Table 4.6 shows the background functions and variations and their estimated systematic effect. To be conservative, the larger numbers were used to estimate the total size of the systematic error due to fitting the background area.

Table 4.6: Table of the hadron background subtraction systematics

	Background Variation	Effect at p_T 2-10	8-16	14-30 GeV/c
Variation:	Exponential Background	+6%	-2%	-8%
Variation:	Polynomial Background	+3%	+7%	-8%
Variation:	Smaller Fit Range	+1%	+1%	-1%
Variation:	Larger Fit Range	-1%	+1%	+2%
	Total Effect:	±6%	±7%	±8%

Table 4.7: Table of the electron signal fitting systematics

	Signal Fitting Variation	Effect at p_T 2-10	8-16	14-30 GeV/c
Variation:	Restricting $e^{\pm}$ peak position	-6%	+1%	-2%
Variation:	Restricting $e^{\pm}$ peak width	-3%	+1%	-2%
	Total Effect:	±6%	±1%	±2%

There is also a systematic error due to not knowing the true shape of the signal shape. To get an estimation of this effect, the fitting of the electron signal width and peak position were varied. In order to get the best estimation of the number of electrons the default function allows the E/p peak to be inside of a small range near $E/p = 1.0$. One variation that was tried restricted the signal E/p peak to be at 1.0. This had a larger effect in minimum bias data, since the electron signal peak drifts with p_T in the minimum bias data. In the $2 < p_T < 4$ range, the signal peaks at around $E/p = 0.95$. For the next three p_T bins the signal peaks at around $E/p = 0.975$, 0.99, and 1.0. Above $p_T = 10$, and for the triggered data, the E/p peak is stable at 1. Varying the signal E/p peak has a larger effect in minimum bias data than in the triggered data due to the shifting electron signal position. The default fitting function allows the width of the signal Gaussian width to be in a small range. One variation tried was restricting the Gaussian width to be exactly 0.063, the average signal width. Table 4.7 shows the systematic effect of these variations on the electron signal fitting.

4.10.5 Total Systematics

Table 4.8 shows a summary of the systematic errors from this analysis. The total systematics for the heavy flavor electron yield in minimum bias events was 10.4%. The systematics for EG2 events is 16% and EG1 events is 14%.

To calculate the heavy flavor electron cross section, the yield needs to be multiplied by $\sigma_{MB}^{V0} = 2.09$ barns ± 0.07 (syst)[70]. This value has a systematic error of 3.4%.

Table 4.8: Table of the summary of systematic errors

Source	Effect at p_T 2-10	8-16	14-30 GeV/c
n_σ^{TPC}	$\pm 1\%$	$\pm 6\%$	$\pm 7\%$
Shower Shape	$\pm 1\%$	$\pm 2\%$	$\pm 6\%$
E/p	$\pm 5\%$	$\pm 3\%$	$\pm 4\%$
Background signal fitting	$\pm 6\%$	$\pm 7\%$	$\pm 8\%$
Electron signal fitting	$\pm 6\%$	$\pm 1\%$	$\pm 2\%$
Trigger Scaling	NA	12%	3%
Track matching		1%	
Photonic Electron		3%	
Total Systematics for yield	10%	16%	14%
Systematics for σ_{MB}^{V0}		3.4%	

Chapter 5

Results and Discussion

The major components of the steps of the analysis have been described in Chapter 4. In section 4.3 any events or tracks with bad quality or were known to be from a source of background were removed. Then the electrons were enhanced from the background by applying particle identification cuts n_{σ}^{TPC} (section 4.6.1), E/p (section 4.6.2), and M20 (section 4.6.3). The hadrons that passed the electron identification cuts and misidentified as electrons were subtracted in section 4.7. From the inclusive electron yield the main sources of background were calculated and removed using the invariant mass method (section 4.8). The electrons remaining were then corrected for the geometrical acceptance and efficiency of reconstructing an electron from semileptonic heavy-flavor hadron decays, shown in section 4.9. After putting all of these components together, the p_T-differential invariant yield and cross section for electrons from decays of heavy flavor hadrons can be obtained.

5.1 Invariant Yield of HFE

The p_T-differential invariant yield of single electrons from decays of bottom and charm hadrons, $(e^+ + e^-)/2$, is given by:

$$\frac{1}{2\pi p_T}\frac{\mathrm{d}^2 N_{HFE}}{\mathrm{d}p_T \mathrm{d}y} = \frac{1}{2}\frac{1}{2\pi p_T^{center}}\frac{1}{\Delta y \Delta p_T}\frac{N_{HFE}^{raw}}{(\epsilon^{geo}\times\epsilon^{reco}\times\epsilon^{eID})}\frac{1}{N_{MB}N_{Trigg.Scaling}} \tag{5.1}$$

In this equation [39], p_T^{center} is the mean p_T of each p_T bin. The geometrical acceptance in rapidity in the lab frame is given by Δy. The width of the p_T bin is Δp_T. N_{MB} is the number of minimum bias collisions analyzed. $N_{Trigg.Scaling}$ is the trigger scaling, described in detail in 4.5.

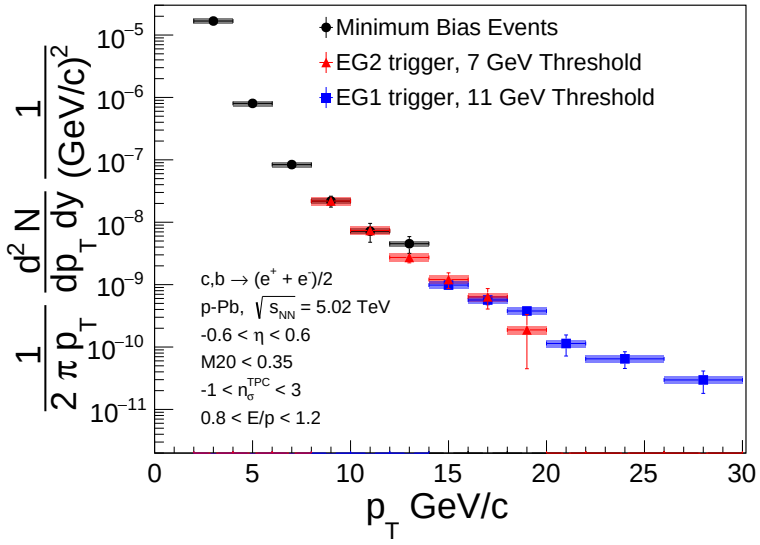


Figure 5.1: Yield for heavy flavor electrons in pPb collisions at $\sqrt{s_{NN}} = 5.02$ TeV measured in ALICE. Minimum Bias events are shown in black dots. EG2 triggered events are shown in red triangles. EG1 triggered events are shown in blue squares.

Figure 5.1 shows p_T-differential invariant yield for heavy flavor electrons. The yield per minimum bias events is shown for minimum bias, EG2 and EG1 triggered events. The horizontal bars show the width of the p_T bin. The vertical error bars show the statistical errors and the shaded vertical error bars show the systematic errors. The yield for Minimum Bias events and triggered events agree within statistical and systematic error bars in the overlapping p_T regions, $8 < p_T < 20$ GeV/c.

5.2 Cross Section of HFE

The equation for the cross section is similar to the equation for the invariant yield:

$$\frac{1}{2\pi p_T}\frac{\mathrm{d}^2\sigma_{HFE}}{\mathrm{d}p_T\mathrm{d}y} = \frac{1}{2\pi p_T}\frac{\mathrm{d}^2N_{HFE}}{\mathrm{d}p_T\mathrm{d}y} \times \sigma_{MB}^{V0} \tag{5.2}$$

In this equation, σ_{MB}^{V0} is the cross section for Minimum Bias events in measured in ALICE using the VZERO trigger and is $\sigma_{MB}^{V0} = 2.09 \pm 0.07$ barns [70].

Figure 5.2 shows the p_T-differential invariant cross section for heavy flavor electrons. The various triggers agree within their systematic and statistical error bars in the overlapping p_T regions.

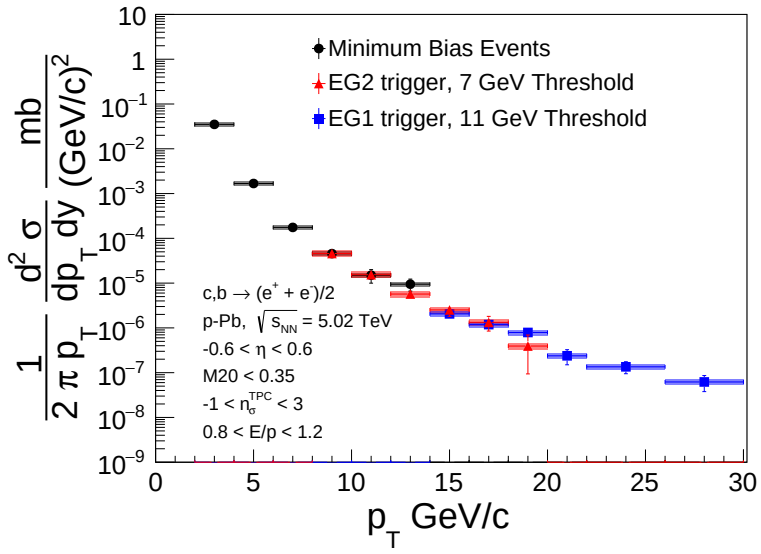


Figure 5.2: Cross Section for heavy flavor electrons in pPb collisions at $\sqrt{s_{NN}} =$ 5.02 TeV measured in ALICE. Minimum Bias events are shown in black dots. EG2 triggered events are shown in red triangles. EG1 triggered events are shown in blue squares.

The measurements for the three event samples can be combined using a weighted mean, where the weighting factor is the inverse square of the error. The weighted mean of the Minimum Bias, EG2 and EG1 triggered events is drawn in figure 5.3.

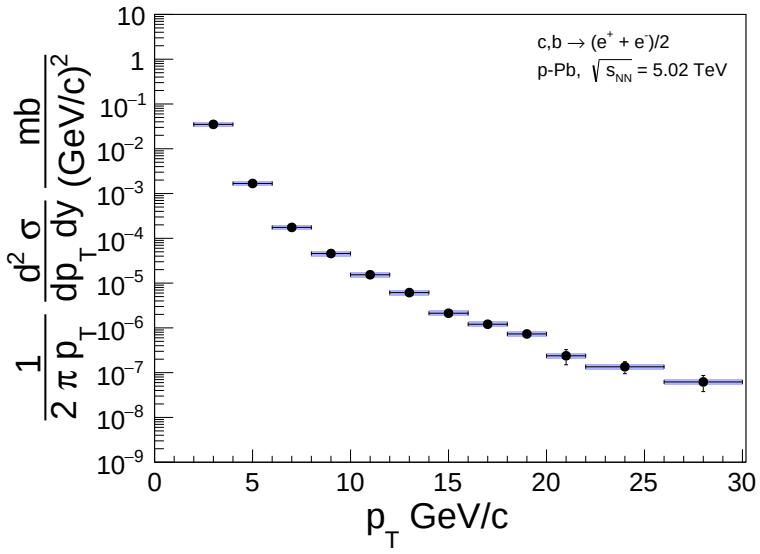


Figure 5.3: Cross Section for heavy flavor electrons in pPb collisions at $\sqrt{s_{NN}}$ = 5.02 TeV measured in ALICE. Minimum Bias, EG2 and EG1 triggered events are combined using a weighted average.

5.3 Nuclear Modification Factor R_{pA}

The nuclear modification factor can help understanding the cold nuclear matter effects with respect to those in proton-proton collisions.

The R_{pPb} can be calculated as the ratio of the cross section of electrons from decays of bottom and charm hadrons in p-Pb collisions and pp collisions scaled by the number of nucleons in the Pb nucleus. The pp reference spectrum should be multiplied by the number of nucleons in the lead nucleus, A=208.

$$R_{pPb} = \frac{1}{A} \frac{d\sigma_{pPb}/dp_T}{d\sigma_{pp}/dp_T} \tag{5.3}$$

The R_{pPb} can also be calculated using the yield in pPb and pp collisions. In this case, the pp collisions are scaled by the average number of binary nucleon-nucleon collisions as calculated by the Glauber model, $\langle N_{coll}^{Glauber} \rangle = 6.87 \pm 5.10$ for minimum bias pPb collisions [16]. When comparing the yield in pPb collisions and cross section in pp collisions, pp should be scaled by the thickness function, $\langle T_{pPb}^{Glauber} \rangle = 0.0983 \pm$

0.0728 mb^{-1} for minimum bias pPb collisions [16]. All of these equations for R_{pPb} will give an equivalent result.

$$R_{pPb} = \frac{1}{\langle N_{coll}^{Glauber} \rangle} \frac{\mathrm{d}N^{\mathrm{pPB}}/\mathrm{d}p_T}{\mathrm{d}N^{\mathrm{pp}}/\mathrm{d}p_T} = \frac{1}{\langle T_{pPb}^{Glauber} \rangle} \frac{\mathrm{d}N^{\mathrm{pPB}}/\mathrm{d}p_T}{\mathrm{d}\sigma^{\mathrm{pp}}/\mathrm{d}p_T} \tag{5.4}$$

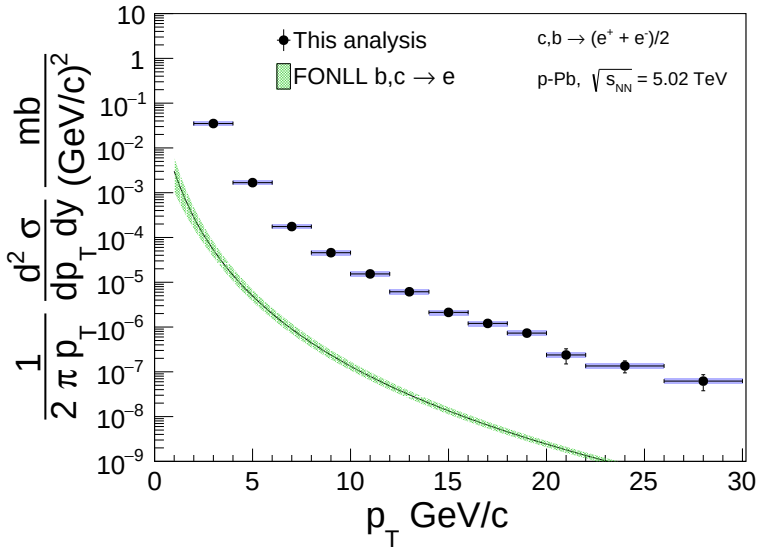


Figure 5.4: FONLL pQCD theory calculation for the single electron cross section at $\sqrt{s} = 5.02$ TeV compared to the cross section from this analysis.

There is currently no pp measurement at $\sqrt{s} = 5.02$ TeV for electrons from decays of bottom and charm hadrons. The Fixed Order plus Next-to-Leading-Log perturbative Quantum Chromodynamics (FONLL pQCD) theory calculations have been demonstrated to agree with heavy flavor measurements at the LHC [75] [39], especially in the p_T region relevant to this analysis. Figure 5.4 shows the FONLL calculation [28] for pp collisions at $\sqrt{s} = 5.02$ TeV for heavy flavor electron decays along with the cross section from this analysis.

The FONLL calculation [28] included the standard parameter set and standard parton distribution function, CTEQ6.6. The FONLL prediction has some uncertainty associated with the factorization and renormalization scales, μ_F and μ_R and the uncertainty of the mass of charm and bottom quark, m_c and m_b. The central value calculation used the mass of bottom $m_b = 4.75$ GeV, and mass of charm $m_c = 1.5$

GeV. In figure 5.4, the central value for FONLL is drawn with a solid line. The width of the filled area is the uncertainties due to scales and masses are summed in quadrature.

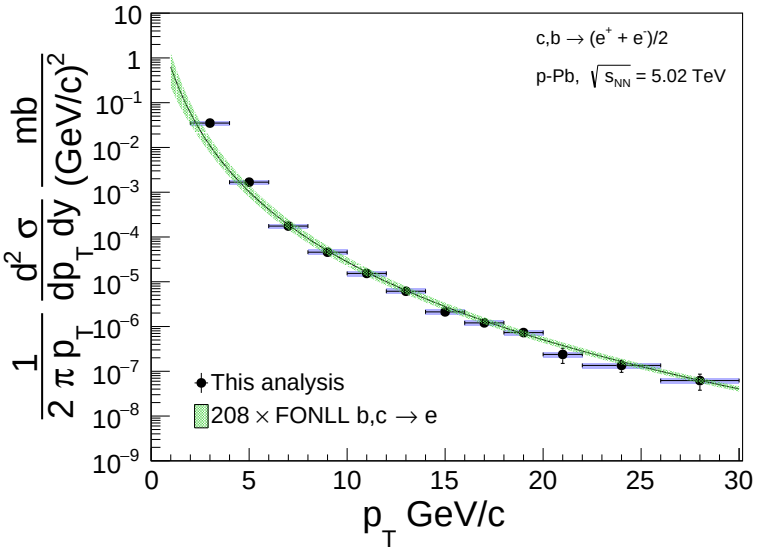


Figure 5.5: Cross section from this analysis compared to scaled FONLL [28] pQCD calculation.

The FONLL reference was scaled by the number of nucleons in the lead nucleus, as in equation 5.3 and demonstrated on figure 5.5. The scaled FONLL reference matches well with the measurement in pPb collisions.

Figure 5.6 shows the R_{pA} using the FONLL reference. The error due to the uncertainty in the FONLL calculation is not included in the systematic error in this plot. The R_{pA} shows a slight enhancement at low p_T, and is consistent with unity within statistical and systematic error bars for $p_T > 8$.

5.4 Comparison to previous measurement

The cross section in this analysis agrees with a previous analysis [40] measured in ALICE with Minimum Bias events, as shown in figure 5.7. This analysis was able

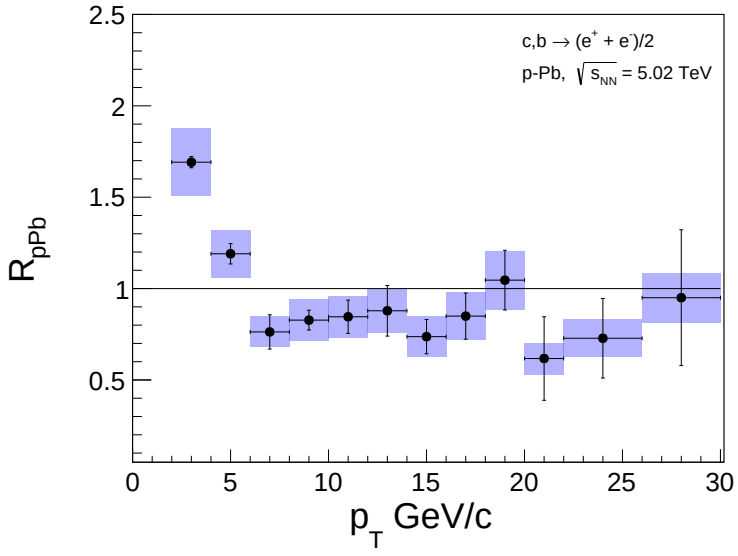


Figure 5.6: R_{pPb} using FONLL pQCD theory calculation as a reference.

to extend the p_T reach of the previous analysis. The cross sections agree within systematic and statistical error bars.

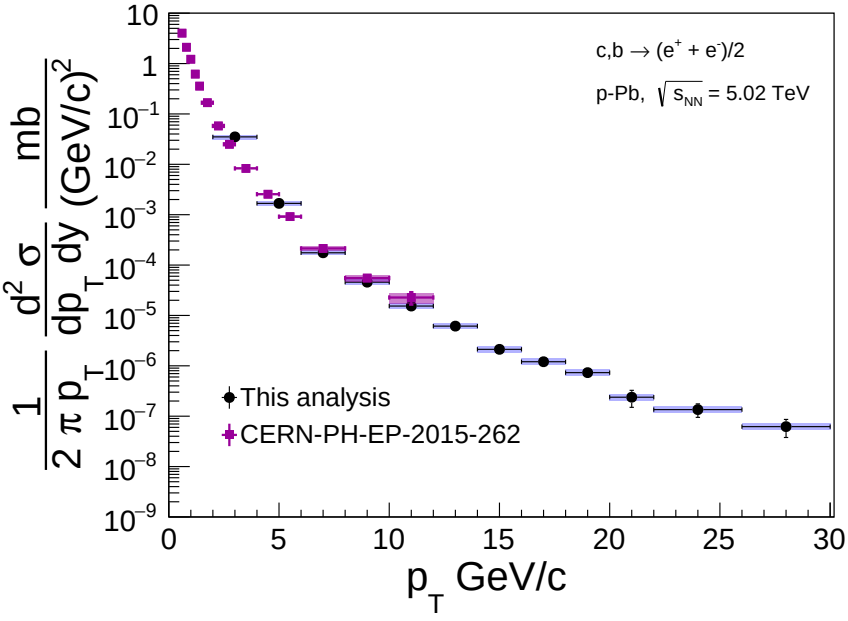


Figure 5.7: Heavy flavor electron cross section compared with the published [40] ALICE pPb cross section drawn in purple.

Figure 5.8 [76], compares the R_{pA} from this analysis with the previous analysis [40] measured in ALICE with Minimum Bias events. The R_{pPb} obtained is consistent

within systematic and statistical error bars. Both analyses measure R_{pPb} as unity within uncertainties. This suggests that cold nuclear matter effects are small in pPb collisions at LHC energies. Several theoretical models are shown on figure 5.8. Included in the theory curves shown are FONLL+ EPS09NLO [27] nuclear modification and parameterization from input of deep inelastic scattering, Drell-Yan dilepton production and inclusive pion production. The blast wave calculation [77] is a hydrodynamic model that assumes that the heavy quarks flow with the expansion of a medium. Also shown are theories that include coherent multiple scattering [78] and incoherent multiple scatterings [8]. All four of these theory calculations predict small cold nuclear matter effects in pPb collisions and agree with the data.

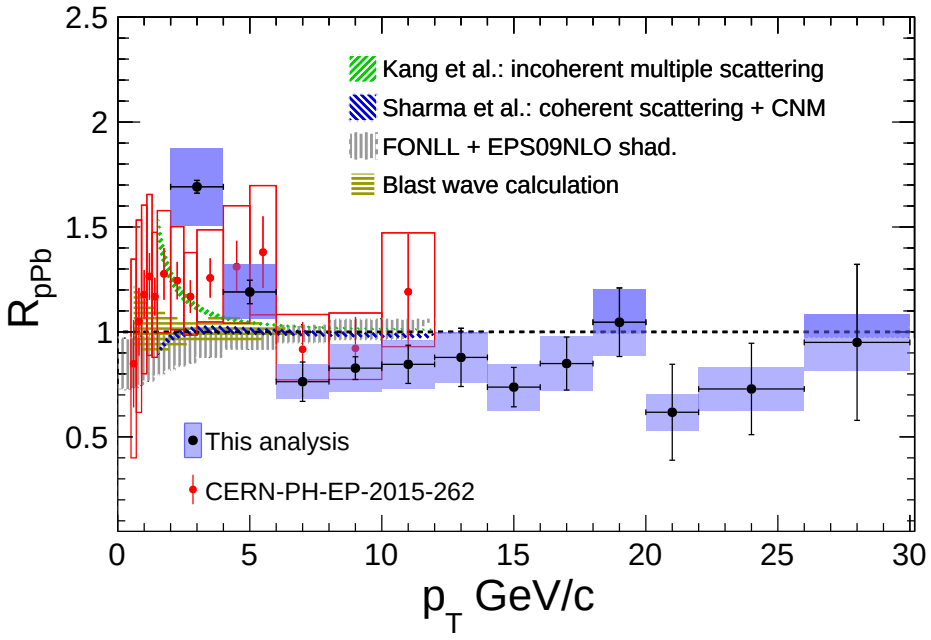


Figure 5.8: R_{pPb} measured in this analysis compared to the published result [40]. Four theoretical models are included: incoherent multiple scatterings [8], coherent multiple scattering [78], FONLL+ EPS09NLO [27] and blast wave calculation [77].

5.5 Comparison to similar analysis

Figure 5.9 shows R_{pPb} for the average of D^0, D^+ and D^{*+} mesons and their charge conjugates measured in pPb collisions in ALICE [41] as compared to the R_{pPb} from this analysis. The D mesons were measured by reconstructing their hadronic decay channel. When comparing these plots it is important to note that the x-axis of the D mesons plot is the D meson p_T, while the x-axis of this analysis is p_T^e. The electrons from decays of D and B mesons carry away a fraction of the p_T of the D or B meson. The heavy flavor decay electron at a p_T bin samples a range of D and B mesons at a higher p_T. The R_{pPb} for electrons from heavy flavor decays agrees and the average D meson measurement both show an R_{pPb} consistent with unity.

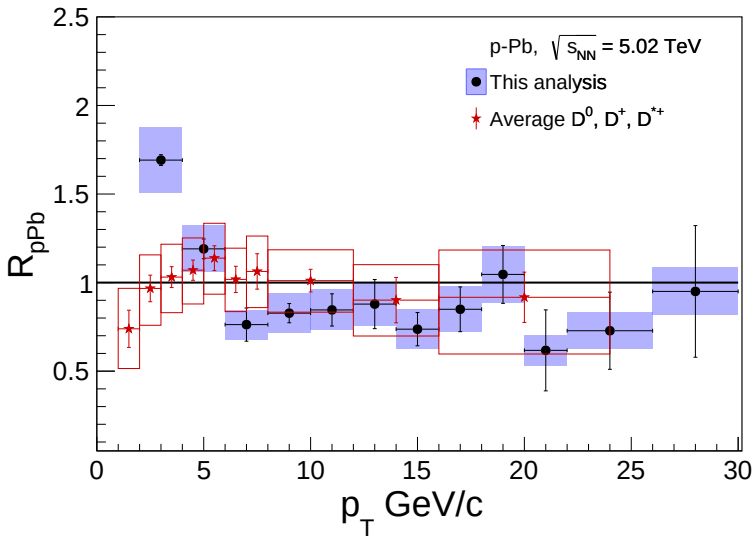


Figure 5.9: R_{pPb} for the average of D^0, D^+ and D^{*+} mesons [41] in ALICE, for pPb collisions at $\sqrt{s_{NN}} = 5.02$ TeV as compared to the R_{pPb} from this analysis.

Figure 5.10 compares the R_{pPb} for this analysis to the measurement of electrons from heavy flavor decays in d+Au (deuteron+gold) collisions at $\sqrt{s_{NN}} = 200$ GeV measured by the PHENIX experiment at RHIC, drawn with red points. The R_{d+Au} exhibits evidence of an enhancement as compared to pp collisions.

Figure 5.11 shows R_{AA} of electrons from heavy-flavor hadron decays in heavy ion collisions measured by ALICE and PHENIX [37] experiments for 0-10% centrality

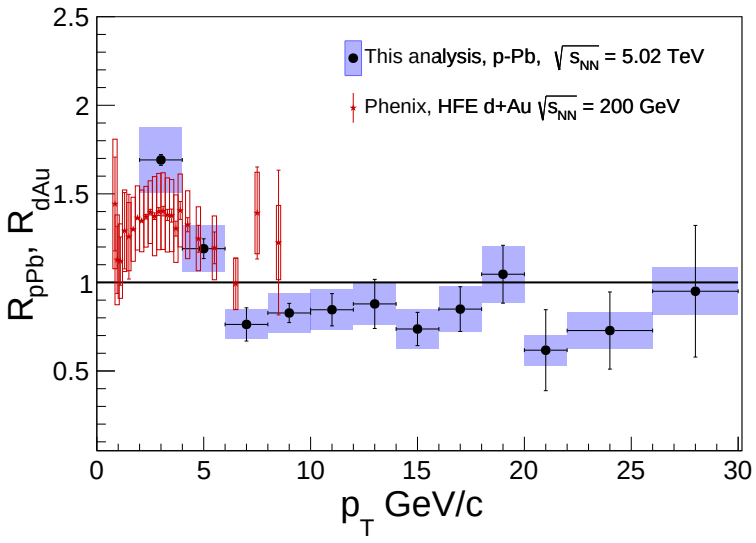


Figure 5.10: Nuclear modification factor for electrons from heavy flavor decays for this analysis as compared to d+Au collisions measured in PHENIX at $\sqrt{s_{NN}} = 200$ GeV [25].

Pb+Pb and the Au+Au collisions. The two measurements both show a nuclear modification factor consistent with unity at low p_T and a large suppression when moving to higher p_T. Since R_{dAu} and R_{pPb} is consistent with a slight enhancement or unity, then the suppression seen in R_{AA} cannot be explained by initial state effects or cold nuclear matter effects.

5.6 Comparison to other results

How does the R_{pA} for heavy flavor compare to other particle types? Figure 5.12 shows R_{pA} for inclusive charged pions ($\pi^+ + \pi^-$) and protons ($\mathrm{p}^+ + \bar{\mathrm{p}}$) measured in ALICE [80] as compared to electrons from heavy flavor hadron decays measured in this analysis. The protons show the most enhancement. All of the hadrons are consistent with unity at high transverse momentum. R_{pA} for electrons from heavy-flavor hadron decays agrees well with the R_{pA} for charged pions.

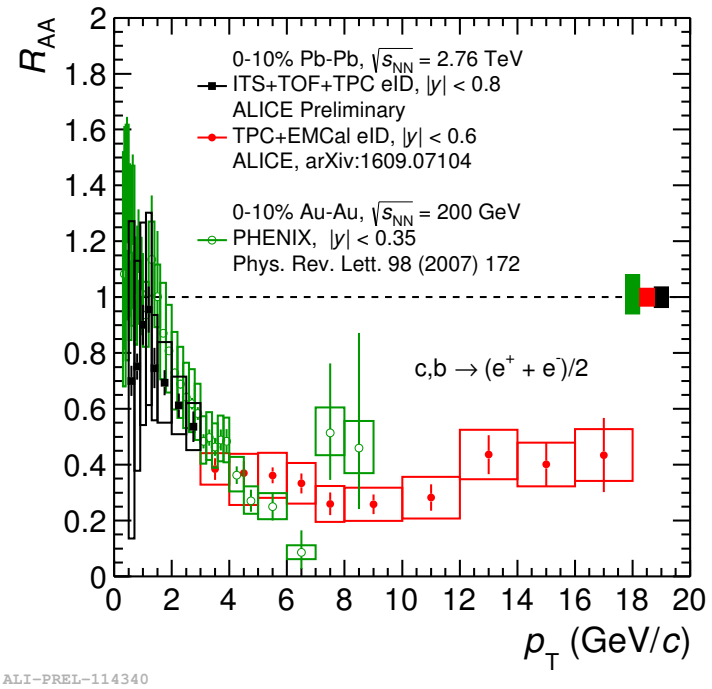


Figure 5.11: R_{AA} of electrons from heavy-flavor hadron decays measured in ALICE and RHIC. The black and red points show 0-10% most central Pb-Pb events at $\sqrt{s_{NN}}$ = 2.76 TeV measured in ALICE [79]. The green points show the 0-10% most central Au-Au events at $\sqrt{s_{NN}}$ = 200 GeV measured by Phenix [37].

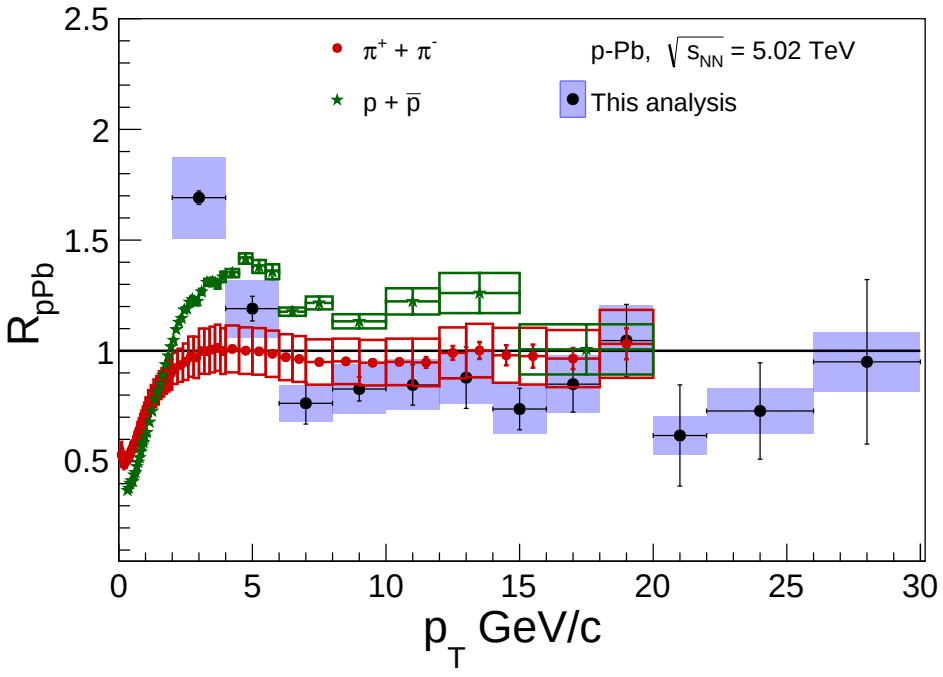


Figure 5.12: R_{pA} for charged pions and protons [80] measured in ALICE for pPb collisions at $\sqrt{s_{NN}} = 5.02$ TeV compared to the R_{pA} for this analysis.

Chapter 6

Summary and Conclusions

The purpose of the measurement described in this work is to address issues concerning cold nuclear matter effects in the production of the heavy flavor quarks in relativistic heavy ion collisions. Is the yield of heavy flavor produced in collisions affected by the additional nucleons present in proton-nucleus collisions as compared to proton-proton collisions? Additionally, is the production and momentum distribution of heavy quarks affected differently from light quarks? Furthermore, are there new physics effects at the high LHC energies as compared to what has been previously measured at RHIC?

In order to address these questions, the Large Hadron Collider accelerated and collided protons at 4 TeV with lead ions at 82x4 TeV. These asymmetrical proton-lead collisions at center of mass energy per nucleon $\sqrt{s_{NN}} = 5.02$ TeV were measured by ALICE. This analysis measured the yield of mesons composed of one charm or bottom quark and a light quark, $D^+, D^-, D^0, \bar{D}^0, B^+, B^-, B^0, \bar{B}^0$. The production of D and B hadrons were measured through their semileptonic decay channel by measuring the single electron yield.

Electrons were enhanced by using the tracking and energy measurements provided by the Time Projection Chamber and the Electromagnetic Calorimeter. The remaining hadron contamination was subtracted with a function that was fit to

the detector response of the electron signal and the hadron background. This measurement covered a novel transverse momentum range made possible by the EMCal trigger system. However, these triggers introduced an additional background that needed to be accounted for in the background subtraction.

The main sources of background electrons are from photon conversion and from Dalitz decay of light mesons. This analysis estimated the yield of background electrons by exploiting the fact that the main background sources produced electrons in pairs with an invariant mass near zero, while the signal produced single electrons.

The final results of the yield, cross section, and R_{pPb} of electrons from the decays of D and B mesons in pPb collisions as measured in ALICE at the LHC were presented in figure 5.1, figure 5.3 and figure 5.6.

This analysis extended the transverse momentum reach of an earlier measurement in ALICE [40]. The measurement of the cross section agrees with the earlier measurement as shown in figure 5.7. The transverse momentum coverage of this analysis was able to extend the p_T reach of the previous measurement from 12 GeV/c up to 30 GeV/c using the EMCal triggers.

The R_{pPb} of this measurement demonstrated agreement with the previous measurement in the p_T overlap region in figure 5.8. A similar analysis, that reconstructs the D meson using the hadronic decay channel, was also shown to agree with the measurement from this analysis in figure 5.9.

Theoretically the data are well described by FONLL, Fixed Order plus Next-to-Leading-Log perturbative Quantum Chromodynamics theory calculation with standard parameters. The pQCD theory was calculated for proton-proton collisions and then scaled using the average number of binary nucleon-nucleon collisions to compare with proton-lead collisions illustrated in figure 5.5. FONLL describes the data well across six orders of magnitude. More advanced models that take into account various cold nuclear matter effects were also consistent with this measurement, as depicted in figure 5.8.

This measurement was compared a similar collision system, $d + Au$, at a lower energy, $\sqrt{s_{NN}} = 200$ GeV measured at RHIC. Figure 5.10 shows a slight possible Cronin enhancement at low p_T and is consistent with unity at higher p_T. These results show that the effects of cold nuclear matter in pPb collisions as compared to pp collisions are small for heavy flavor hadrons at LHC energies and do not deviate significantly from the measurements at RHIC energies.

As seen in figure 5.12, the D and B mesons seem to scale similarly to other light flavored charged hadrons when comparing pp to pPb collisions. The modification of light and heavy quarks are comparable in pPb collisions.

Figure 5.10 and figure 5.11 illustrate a significant suppression in heavy ion collisions, $Au + Au$ and the $Pb - Pb$, at RHIC and LHC energies. Since the $d + Au$ and pPb collision data does not show any signs of suppression on heavy flavor, initial state effects and cold nuclear matter effects can not explain the suppression seen in central heavy ion collisions and must be due to hot nuclear matter effects.

Bibliography

[1] David Griffiths. *Introduction to elementary particles*. 2008. 2, 4

[2] Wikimedia Commons: MissMJ. Standard model of elementary particles., 2014. [Online, accessed 19-Jan-2016] `https://commons.wikimedia.org/wiki/File:Standard_Model_of_Elementary_Particles.svg`. 2, 3

[3] J. Beringer et al. Review of Particle Physics (RPP). *Phys. Rev.*, D86:010001, 2012. 2, 7, 56, 57

[4] F. Halzen and Alan D. Martin. *Quarks and Leptions: An Introductory Course In Modern Particle Physics*. 1984. 4

[5] Siegfried Bethke. World Summary of α_s (2012). 2012. [Nucl. Phys. Proc. Suppl.234,229(2013)] arXiv:1210.0325. 5, 23, 24

[6] K. Adcox et al. Formation of dense partonic matter in relativistic nucleus-nucleus collisions at RHIC: Experimental evaluation by the PHENIX collaboration. *Nucl. Phys.*, A757:184–283, 2005. arXiv:nucl-ex/0410003. 5

[7] John C. Collins, Davison E. Soper, and George F. Sterman. Heavy Particle Production in High-Energy Hadron Collisions. *Nucl. Phys.*, B263:37, 1986. 5

[8] Zhong-Bo Kang, Ivan Vitev, Enke Wang, Hongxi Xing, and Cheng Zhang. Multiple scattering effects on heavy meson production in p+A collisions at backward rapidity. *Phys. Lett.*, B740:23–29, 2015. arXiv:1409.2494. 6, 122

[9] Gerhard A. Schuler. Production of heavy quarks and heavy quarkonia. *Z. Phys.*, C71:317–328, 1996. arXiv:hep-ph/9504242. 6

[10] R. Vogt. Shadowing and absorption effects on J/ψ production in dA collisions. *Phys. Rev.*, C71:054902, 2005. 6

[11] Donald Eric Hornback. *A measurement of open charm using single muons at forward angles for p+p collisions at center of mass energy 200 GeV*. PhD thesis, The University of Tennessee, Knoxville, 2008. 8

[12] C. Y. Wong. *Introduction to high-energy heavy ion collisions*. 1995. 10, 16

[13] Wikimedia Commons: JabberWok. A graphic showing the relationship between angle and pseudorapidity., 2007. [Online, accessed 4-May-2016 File:Pseudorapidity2.png] `https://commons.wikimedia.org/wiki/File:Pseudorapidity2.png`. 10

[14] Michael L. Miller, Klaus Reygers, Stephen J. Sanders, and Peter Steinberg. Glauber modeling in high energy nuclear collisions. *Ann. Rev. Nucl. Part. Sci.*, 57:205–243, 2007. arXiv:nucl-ex/0701025. 11

[15] Maarten Bruinsma. *J/ψ in pA - Performance of the First Level Trigger of HERA-B and Nuclear Effects in J/ψ Production*. PhD thesis, University of Utrecht, 2002. 12

[16] Jaroslav Adam et al. Centrality dependence of particle production in p-Pb collisions at $\sqrt{s_{\rm NN}}$= 5.02 TeV. *Phys. Rev.*, C91(6):064905, 2015. arXiv:1412.6828. 12, 14, 15, 118, 119

[17] Nicolas Borghini and Francois Gelis. Distribution of multiple scatterings in proton-nucleus collisions at high energy. *Phys. Rev.*, D74:054025, 2006. arXiv:hep-ph/0607098. 13

[18] A. Adare et al. Transverse energy production and charged-particle multiplicity at midrapidity in various systems from $\sqrt{s_{NN}}$ = 7.7 to 200 GeV. *Phys. Rev.*, C93(2):024901, 2016. arXiv:1509.06727. 15, 16

[19] Bo Nilsson-Almqvist and Evert Stenlund. Interactions Between Hadrons and Nuclei: The Lund Monte Carlo, Fritiof Version 1.6. *Comput. Phys. Commun.*, 43:387, 1987. 16

[20] Peter Z. Skands. QCD for Collider Physics. In *High-energy Physics. Proceedings, 18th European School, ESHEP 2010, Raseborg, Finland, 20 Jun. - 3 Jul., 2010*, 2011. arXiv:1104.2863. 17

[21] Bo Andersson, G. Gustafson, G. Ingelman, and T. Sjostrand. Parton Fragmentation and String Dynamics. *Phys. Rept.*, 97:31–145, 1983. 18

[22] Michael Leitch. Highlights from PHENIX-I: Initial State and Early Times. *Nucl. Phys.*, A830:27C–34C, 2009. arXiv:0907.4627. 19

[23] J. W. Cronin, Henry J. Frisch, M. J. Shochet, J. P. Boymond, R. Mermod, P. A. Piroue, and Richard L. Sumner. Production of hadrons with large transverse momentum at 200, 300, and 400 GeV. *Phys. Rev.*, D11:3105–3123, 1975. 19

[24] Alberto Accardi. Cronin effect in proton nucleus collisions: A Survey of theoretical models. 2002. arXiv:hep-ph/0212148. 19, 20

[25] A. Adare et al. Cold-nuclear-matter effects on heavy-quark production in d+Au collisions at $\sqrt{s_{NN}} = 200$ GeV. *Phys. Rev. Lett.*, 109(24):242301, 2012. arXiv:1208.1293. 20, 21, 30, 31, 124

[26] T. Lappi. Understanding saturation and AA collisions with an eA collider. *Nucl. Phys.*, A830:403C–410C, 2009. arXiv:0907.4588. 21

[27] K. J. Eskola, H. Paukkunen, and C. A. Salgado. EPS09: A New Generation of NLO and LO Nuclear Parton Distribution Functions. *JHEP*, 04:065, 2009. arXiv:0902.4154. 21, 22, 122

[28] Matteo Cacciari, Mario Greco, and Paolo Nason. The p_T spectrum in heavy flavor hadroproduction. *JHEP*, 05:007, 1998. arXiv:hep-ph/9803400. 24, 25, 119, 120

[29] O. Botner, L. O. Eek, T. Ekelof, K. Fransson, A. Hallgren, P. Kostarakis, G. Lenzen, and B. Lund-Jensen. Production of Prompt Electrons in the Charm p_T Region at $\sqrt{s} = 630$-GeV. *Phys. Lett.*, B236:488, 1990. 25, 27, 28

[30] Matteo Cacciari. FONLL Heavy Quark Production., 2016. "http://www.lpthe.jussieu.fr/~cacciari/fonll/fonllform.html". 25

[31] Matteo Cacciari, Paolo Nason, and Ramona Vogt. QCD predictions for charm and bottom production at RHIC. *Phys. Rev. Lett.*, 95:122001, 2005. arXiv:hep-ph/0502203. 26

[32] F. W. Busser et al. Observation of High Transverse Momentum Electrons at the CERN ISR. *Phys. Lett.*, B53:212–216, 1974. 26, 27

[33] C. Albajar et al. Beauty production at the CERN p anti-p collider. *Phys. Lett.*, B256:121–128, 1991. [Erratum: Phys. Lett.B262,497(1991)]. 28

[34] F. Abe et al. Measurement of the bottom quark production cross-section using semileptonic decay electrons in $p\bar{p}$ collisions at $\sqrt{s} = 1.8$ TeV. *Phys. Rev. Lett.*, 71:500–504, 1993. 29

[35] F. Abe et al. Measurement of bottom quark production in 1.8 TeV $p\bar{p}$ collisions using semileptonic decay muons. *Phys. Rev. Lett.*, 71:2396–2400, 1993. 29

[36] S. Abachi et al. Inclusive μ and B quark production cross-sections in $p\bar{p}$ collisions at $\sqrt{s} = 1.8$ TeV. *Phys. Rev. Lett.*, 74:3548–3552, 1995. 29, 30

[37] A. Adare et al. Energy Loss and Flow of Heavy Quarks in Au+Au Collisions at $\sqrt{s_{NN}} = 200$ GeV. *Phys. Rev. Lett.*, 98:172301, 2007. arXiv:nucl-ex/0611018. 30, 31, 123, 125

[38] A. Adare et al. Cold-Nuclear-Matter Effects on Heavy-Quark Production at Forward and Backward Rapidity in d+Au Collisions at $\sqrt{s_{NN}} = 200$ GeV. *Phys. Rev. Lett.*, 112(25):252301, 2014. arXiv:1310.1005. 31, 32

[39] Betty Abelev et al. Measurement of electrons from semileptonic heavy-flavour hadron decays in pp collisions at $\sqrt{s} = 7$ TeV. *Phys. Rev.*, D86:112007, 2012. arXiv:1205.5423. 32, 33, 96, 97, 98, 116, 119

[40] Jaroslav Adam et al. Measurement of electrons from heavy-flavour hadron decays in p-Pb collisions at $\sqrt{s_{\rm NN}} = 5.02$ TeV. *Phys. Lett.*, B754:81–93, 2016. arXiv:1509.07491. 34, 35, 36, 120, 121, 122, 128

[41] Betty Bezverkhny Abelev et al. Measurement of prompt D-meson production in $p - Pb$ collisions at $\sqrt{s_{NN}} = 5.02$ TeV. *Phys. Rev. Lett.*, 113(23):232301, 2014. arXiv:1405.3452. 35, 36, 37, 38, 123

[42] Vardan Khachatryan et al. Study of B Meson Production in p+Pb Collisions at $\sqrt{(}s_{NN}) = 5.02$ TeV Using Exclusive Hadronic Decays. *Phys. Rev. Lett.*, 116(3):032301, 2016. arXiv:1508.06678. 39

[43] Lyndon Evans and Philip Bryant. LHC Machine. *JINST*, 3:S08001, 2008. 41

[44] K. Aamodt et al. The ALICE experiment at the CERN LHC. *JINST*, 3:S08002, 2008. 41, 42, 71

[45] E. Abbas et al. Performance of the ALICE VZERO system. *JINST*, 8:P10016, 2013. arXiv:1306.3130. 43, 44, 45, 46

[46] P Cortese et al. ALICE technical design report on forward detectors: FMD, T0 and V0. 2004. CERN-LHCC-2004-025. 43, 44, 45

[47] Jochen Thaeder. 3D ALICE Schematic - ITS inlay, 2012. `https://aliceinfo.cern.ch/Figure/node/3403`. 47

[48] G. Dellacasa et al. ALICE technical design report of the inner tracking system (ITS). 1999. CERN-LHCC-99-12. 47, 48

[49] Yasser Corrales Morales. Identified hadron production and study of collective phenomena in p-Pb collisions at the LHC with ALICE. In *4th International Conference on New Frontiers in Physics ICNFP2015*, 2015. `https://indico.cern.ch/event/344173/contributions/1740589/attachments/1143630/1638915/150822_Crete_V2.pdf`. 49

[50] G. Dellacasa et al. ALICE: Technical design report of the time projection chamber. 2000. CERN-OPEN-2000-183, CERN-LHCC-2000-001. 50

[51] J. Alme et al. The ALICE TPC, a large 3-dimensional tracking device with fast readout for ultra-high multiplicity events. *Nucl. Instrum. Meth.*, A622:316–367, 2010. arXiv:1001.1950. 50

[52] Francis Demange. Artistic picture of the time projection chamber, 2006. `http://aliceinfo.cern.ch/Public/en/Chapter2/Chap2_TPC.html`. 50

[53] ALICE. 7 TeV proton proton collisions expected for the 30 March 2010, 2010. `http://aliceinfo.cern.ch/Public/en/Chapter1/news2010.html`. 51

[54] Claude Amsler et al. Review of Particle Physics. *Phys. Lett.*, B667:1–1340, 2008. 52

[55] Alexander Philipp Kalweit. TPC dE/dx distribution for p-Pb collisions, 2013. [ALI-PERF-60751]. 53

[56] U. Abeysekara et al. ALICE EMCal Physics Performance Report. 2010. arXiv:1008.0413. 53, 67

[57] P. Cortese et al. ALICE electromagnetic calorimeter technical design report. 2008. CERN-LHCC-2008-014, CERN-ALICE-TDR-014. 53, 54, 55, 56, 59, 60, 61, 62, 63

[58] C. W. Fabjan and F. Gianotti. Calorimetry for particle physics. *Rev. Mod. Phys.*, 75:1243–1286, 2003. 55

[59] Nural Akchurin and Richard Wigmans. Hadron calorimetry. *Nuclear Instruments and Methods in Physics Research Section A: Accelerators, Spectrometers, Detectors and Associated Equipment*, 666:80–97, 2012. 56

[60] Dan Green. Selected topics in sampling calorimetry. Technical report, 1993. 56, 58

[61] Hadron shower, 2015. `http://mathsconcepts.com/node20.html`. 57

[62] Fan Zhang, Hans Muller, Terry. C Awes, Sorin Martoiu, Jiri Kral, David Silvermyr, Alfonso Tarazona Martinez, Guangming Huang, and Daicui Zhou. Point-to-point readout for the ALICE EMCal detector. *Nucl. Instrum. Meth.*, A735:157–162, 2014. 62, 64

[63] Julien Faivre. Relative pre-calibration of the ALICE electromagnetic calorimeter EMCAL. *J. Phys. Conf. Ser.*, 293:012046, 2011. 63, 64

[64] Tomas Robert Prem-Raj Aronsson. *Cross section of bottom electrons in proton-proton collisions in the ALICE experiment*. PhD thesis, Yale University, 2014. 64, 65

[65] Xiangrong Zhu. *Two-Particle Correlations with Neutral Pion and Direct Photon Triggers in pp and Pb+Pb Collisions with ALICE at the LHC*. PhD thesis, CCNU, Wuhan, Inst. Part. Phys., 2014-03-20. 64, 65, 88

[66] O. Bourrion, N. Arbor, G. Conesa-Balbastre, C. Furget, R. Guernane, and G. Marcotte. The ALICE EMCal L1 trigger first year of operation experience. *JINST*, 8:C01013, 2013. arXiv:1210.8078. 67, 68, 69

[67] Betty Abelev et al. Pseudorapidity density of charged particles in p + Pb collisions at $\sqrt{s_{NN}}$ = 5.02 TeV. *Phys. Rev. Lett.*, 110(3):032301, 2013. arXiv:1210.3615. 71

[68] ALICE Experiment. MonALISA Repository for ALICE. Run Condition Table, 2013. `https://alimonitor.cern.ch/configuration/`. 73

[69] Michael Weber. EMCAL Track-Cluster matching (2D), 2012. [ALI-PERF-42973] `https://aliceinfo.cern.ch/Figure/node/3756`. 76

[70] Betty Bezverkhny Abelev et al. Measurement of visible cross sections in proton-lead collisions at $\sqrt{s_{\rm NN}}$ = 5.02 TeV in van der Meer scans with the ALICE detector. *JINST*, 9(11):P11003, 2014. arXiv:1405.1849. 78, 114, 117

[71] Denise Godoy. Shower shape parameters, 2011. [Private Alice TWiki page] `https://twiki.cern.ch/twiki/bin/viewauth/ALICE/ShowerShapeParameters`. 88

[72] Cristiane Jahnke. Non-HFE reconstruction efficiency in p-Pb collisions at 5.02 TeV MB, 2013. [ALI-PERF-52774] `https://aliceinfo.cern.ch/Figure/node/4683`. 103, 104

[73] Cristiane Jahnke. Tagging efficiency for photonic electrons, 2015. [ALI-PREL-99468] `https://aliceinfo.cern.ch/Figure/node/8507`. 103, 104

[74] Roger Barlow. Systematic errors: Facts and fictions. In *Advanced Statistical Techniques in Particle Physics. Proceedings, Conference, Durham, UK, March 18-22, 2002*, pages 134–144, 2002. arXiv:hep-ex/0207026. 107

[75] B. Abelev et al. Measurement of charm production at central rapidity in proton-proton collisions at $\sqrt{s} = 7$ TeV. *JHEP*, 01:128, 2012. arXiv:1111.1553. 119

[76] Jaroslav Adam et al. Measurement of electrons from beauty-hadron decays in p-Pb collisions at $\sqrt{s_{NN}} = \mathbf{5.02}$ TeV and Pb-Pb collisions at $\sqrt{s_{NN}} = \mathbf{2.76}$ TeV. 2016. arXiv:1609.03898. 121

[77] Anne M. Sickles. Possible Evidence for Radial Flow of Heavy Mesons in d+Au Collisions. *Phys. Lett.*, B731:51–56, 2014. arXiv:1309.6924. 122

[78] Rishi Sharma, Ivan Vitev, and Ben-Wei Zhang. Light-cone wave function approach to open heavy flavor dynamics in QCD matter. *Phys. Rev.*, C80:054902, 2009. arXiv:0904.0032. 122

[79] Andrea Dubla. HFE RAA at low pT - Comparison with published high pT result and PHENIX measurements, 2016. [ALI-PREL-114340] `https://aliceinfo.cern.ch/Figure/node/9857`. 125

[80] Jaroslav Adam et al. Multiplicity dependence of charged pion, kaon, and (anti)proton production at large transverse momentum in p-Pb collisions at $\sqrt{s_{NN}}$ = 5.02 TeV. *Phys. Lett.*, B760:720–735, 2016. arXiv:1601.03658. 124, 126

Vita

Rebecca Michelle Scott was born in Indiana in 1986. She spent her early childhood in Florence, Alabama, where she was encouraged to read books and delve into art and the humanities from her middle school math and science teacher mother and her physics professor father. Rebecca's education was achieved in doublets: she attended two elementary schools, two middle schools, two high schools, and two universities. She is now hoping to land two job offers.

At Morehead State University, in Kentucky, she majored in physics and minored in mathematics. In 2007, she was awarded a Physical Sciences Department scholarship and also participated in the Research Experience for Undergraduate program at West Virginia University, where she studied spintronics and magnetism. For her senior project that same year, she investigated an unusual particle drift in a rotating flow, presented at the SESAPS annual meeting and at the MSU Celebration of Student Scholarship. Upon graduation from MSU in 2008, she enrolled in the PhD program at the University of Tennessee, Knoxville.

During her time as a graduate student, Rebecca taught physics labs and won the Outstanding Graduate Teaching Assistant Award in 2009. She joined the UTK Relativistic Heavy Ion Physics group in 2010 to study p+Pb collisions measured by the ALICE experiment at the Large Hadron Collider. Her thesis adviser was Dr. Soren Sorensen.